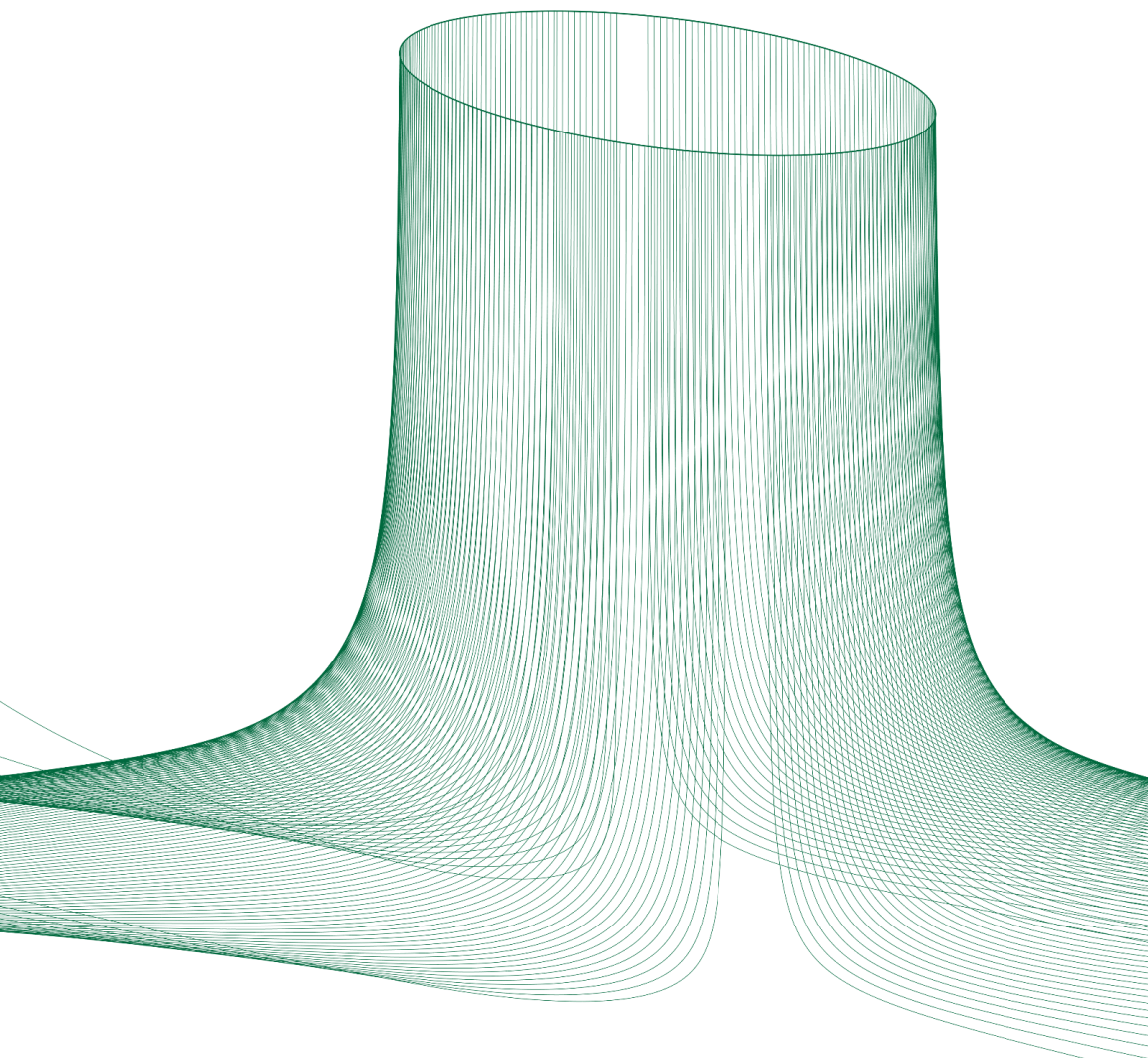


Current Continuity in Auroral System Science



July 2025
Dartmouth College

Jules van Irsel

Current Continuity in Auroral System Science

A Thesis

Submitted to the Faculty

in partial fulfillment of the requirements for the
degree of

Doctor of Philosophy

in

Physics and Astronomy

by Jules van Irsel

Guarini School of Graduate and Advanced Studies
Dartmouth College
Hanover, New Hampshire

July 2025

Examining Committee:

Kristina A. Lynch (chair)

Matthew D. Zettergren

Yi-Hsin Liu

James W. LaBelle

F. Jon Kull, Ph.D.

Dean of the Guarini School of Graduate and Advanced Studies

© Jules van Irsel, 2025

This thesis is licensed under a CC BY-NC-SA 4.0 International License.

Abstract

The Earth relies on the Sun’s energy, but at times this energy can be overwhelming; the Sun expels plasma which, were it not for our humble magnetic field, would erode our atmosphere (Mars, c. 4 Ga). The protective interaction Earth has with the solar wind results in spectacular auroral displays—one such auroral form is discussed in this thesis: quiet discrete auroral arcs.

Such arcs have long been studied; they are abundant, have usable symmetries, and they can predict magnetic substorms that wreak havoc in our magnetosphere. The auroral emissions, albeit beautiful, are however only the visible end of a self-consistent system of currents, electric fields, particle precipitation, and ionospheric conductivity. To study electric currents surrounding auroral arcs, it turns out, requires knowledge of all these aspects.

This thesis enhances our understanding of auroral arcs through the lens of ionospheric current closure. The ionosphere has its plasma transition to being collisional with the neutrals over about 100 km altitude, which allows for currents to flow perpendicular to the local magnetic field—something they cannot do outside our ionosphere. This couples the ionosphere and magnetosphere through magnetic-field-aligned current closure, where the ionosphere can present characteristics not unlike those in a circuit resistor.

The discrete auroral arcs come into play because they are the result of attempting to host field-aligned currents through magnetic flux tubes that can be too tenuous to fulfill their amperage without the creation of parallel electric fields. Such fields can cause electrons to accelerate to energies high enough to ionize the atmosphere. This enhances the ionospheric conductivity, affecting the pathways for current closure.

This thesis outlines methods involving the use of a plethora of heterogeneous, multi-platform auroral measurements curated for driving fully-three-dimensional ionospheric simulations of auroral arcs. This filters for solutions that are geophysical and self-consistent, and allows for the investigation of sensitivities to various input parameters. This work highlights, not just various considerations in performing such simulations, but the very fact that they require all three dimensions for a complete picture. After all, the equations that govern auroral arcs systems are inherently three-dimensional in nature.

*To my partner in life,
Bailey,
for unparalleled love and support throughout the years*

*To my family,
Jacky, Richard, and Bas,
for lifelong lessons, nurture, and encouragement*

*To my friends,
you know who you are,
for without whom I would have finished years earlier*

Acknowledgments

Professor Kristina A. Lynch fosters an overwhelmingly fruitful scientific community; she holds a steadfast commitment to her peers and is endlessly devoted to her students and mentees. Her contribution to this thesis, and the goals it encapsulates, are immeasurable—a feat only paralleled by her constructive influence over my professional, and even personal development throughout the last six years. A heartfelt thank you goes out to her for her invaluable lessons and mentorship.

For his unwavering guidance and providing me with the opportunity to develop the research in this thesis, I also thank professor Matthew D. Zettergren. His grasp on computational physics is near-infinite and his optimistic and confident approach to solving seemingly impossible problems has greatly inspired me. Though things rarely are easy, he makes it look effortless, which has allowed me to take on much more than I ever anticipated.

To professors Yi-Hsin Liu and James W. LaBelle: thank you for being a crucial part of my thesis and granting me this opportunity by joining my committee. Thank you for reviewing this thesis to ensure it exceeds your expectations of exemplary science and that it be free of of any typos. It has been a pleasure working with you.

To the students in the 317 Lab, including Magda L. Moses, Alex Mule, and Charlie R. Acomb: this thesis would not have been possible without your aid and insights, whether with igniting plasmas or deriving equations. More importantly, I also thank you for your comradery—a word I have chosen with intent.

For without whom I would not be here: professor Johnathan K. Burchill. He has been the inspiration that led me to the field of space plasma physics and has, without a doubt, made me a more apt, motivated, and confident researcher. I am ever thankful for his introduction, along with professor David J. Knudsen, to professor Lynch.

For guidance in my research efforts, and a plethora of illuminating meetings and discussions, I thank Meghan Burleigh, Don Hampton, Leslie Lamarche, Hayley L. Clevenger, and Daniel Billett.

I thank Terrence Kovacs, John Griffin, and Michael Hirsch for giving me access to the well of technical knowledge they possess; you humbly remind me of how truly little I know about the world of computer science and software engineering.

Aside from the work presented in this thesis, part of my Ph.D. program has been involved with projects that have given me great experience in plasma instrumentation and sounding rockets. I acknowledge the NASA Sounding Rocket Program, and thank the teams at NSROC, the Wallops Flight Facility, and the Poker Flat Research Range, for giving me the guidance and opportunity to achieve my various goals as an experimentalist. This forgoes the most incredible journeys these projects have led me on, for which I am eternally grateful. For their efforts in allowing me to be a part of these projects, I thank Alan B. Goldblatt, Whitey B. Adams, Christopher M. Grant, Jeffrey D. Renk, and Kristen M. Frederick-Forst.

Last, but far from least, I thank Megan P. Whitlock, Jean L. Blandin, Tressena A. Manning, and Rowan M. Kowalsky for being the foundation of the community we share and for always being available to help me through the most dreaded part of any Ph.D. program: the bureaucracy and paperwork.

For those not mentioned, I can only hope I have expressed my thanks to you, in one way or another, for whenever and wherever you have aided me throughout these enlightening years. If not, then let me say it here:

Thank you. Truly.

Contents

1	Introduction	1
1.1	Background	1
1.1.1	The Magnetosphere	1
1.1.2	Quiet Discrete Auroral Arcs	3
1.2	Fundamental Concepts	5
1.2.1	Current Continuity	5
1.2.2	High-Altitude Plasma Transport	6
1.2.3	Low-Altitude Plasma Transport	8
1.2.4	Ionospheric Current Continuity	12
1.3	Frozen-In Flux, Electric Field Mapping, & the Dungey Cycle	14
1.4	Thesis Statement & Outline	17
2	Manuscript: Generating Top-Boundary Conditions	19
2.1	Introduction	22
2.1.1	Motivation	22
2.1.2	Background	23
2.2	Methodologies	24
2.2.1	Reconstruction	27
2.2.2	Replication	30
2.2.3	Weighted Replications	37
2.3	Auroral Ionosphere 3-D Modeling with Potential Map Estimates	40
2.3.1	The GEMINI model	40
2.3.2	Simulation Examples	41
2.4	Discussions	43
2.4.1	Improvements to Auroral Plasma Flow Mapping	43
2.4.2	Cautionary Remarks	44
2.5	Conclusions & Applications	45

3 Manuscript: Data-Driven 3-D Auroral Simulations	49
3.1 Introduction	52
3.2 Observational Data, Instrumentation, & Methodologies	55
3.2.1 Poker Flat Digital All-Sky Cameras & Imagery Inversion	57
3.2.2 Swarm Spacecraft	57
3.2.3 Poker Flat Incoherent Scatter Radar	58
3.2.4 Super Dual Auroral Radar Network	58
3.2.5 FAC Replication	59
3.2.6 GEMINI Simulations	59
3.2.7 Electron Precipitation Methods	60
3.2.8 Current Flux Tube Visualization	64
3.3 Conjunction Events	66
3.3.1 February 10, 9:51:27 UT	70
3.3.2 February 12, 10:22:11 UT	70
3.3.3 March 4, 7:30:12 UT	70
3.3.4 March 4, 10:13:49 UT	70
3.3.5 March 14, 6:49:07 UT	71
3.3.6 March 19, 8:23:30 UT	71
3.4 Simulation Results	72
3.4.1 Background Flow & Electric Field	72
3.4.2 Electron Precipitation Spectra	84
3.4.3 Along-Arc FAC Structure	92
3.5 Discussions & Conclusions	96
4 Conclusion Summary & Future Work	103
4.1 Conclusion Summary	103
4.2 Future Work	105
A Derivations	107
A.1 Most General Polynomial Harmonic Function	107
A.2 Accelerated Maxwellian Differential Flux Derivation	107
B Simulation Instructions & Flowchart	111
C Simulation Summary & Additional Comparisons	113
C.1 Comparison II: Background Flow	113
C.2 Comparison IV: Background Flow	116
C.3 Comparison VII: Precipitation Spectra	118
C.4 Comparison IX: Precipitation Spectra	120

List of Tables

3.1	Summary of conjunction events with input map values	68
3.2	Summary of event comparisons	73

List of Figures

1.1	Overview of the magnetosphere	2
1.2	Magnetic flux tube connecting the plasmasheet and the auroral ionosphere	4
1.3	Examples of the $\mathbf{E} \times \mathbf{B}$ drift motion for singly-ionized oxygen and an electron	7
1.4	Transition altitudes for plasma collisions	9
1.5	Schematic outlining how collisions create perpendicular currents	10
1.6	The Dungey cycle	14
1.7	Top view of the Dungey cycle	16
2.1	Geographical context used in the reconstruction and replication methods	26
2.2	Example of a plasma flow field reconstruction	30
2.3	Defining arc boundaries using Pedersen conductance contours and Sobel edges	32
2.4	In situ trajectory flow data replication example	33
2.5	Comparing methods for determining potential maps from interpolated flow maps	36
2.6	Validity of harmonic function fitting	37
2.7	Comparison of input maps with and without replication scaling/rotating	38
2.8	Weighted replication example	40
2.9	Plasma flow driven GEMINI output with Figure 2.7c as the potential driver	42
2.10	Calculated FAC components from Equation 2.1	43
3.1	Geographical context of our simulations	56
3.2	Comparison between unaccelerated and accelerated precipitation spectra	62
3.3	Steps in determining the source region characteristic energy	63

3.4	Example of a current flux tube plot using a February 10 simulation	65
3.5	Top-boundary drivers of conjunction events	67
3.6	SuperDARN convection maps of conjunction events	69
3.7	Isometric, side, and top view of the GEMINI results for Simulation Ia	75
3.8	Comparison I (February 10, 9:51 UT)	77
3.9	Comparison III (March 4, 7:30 UT)	79
3.10	Isometric view of the GEMINI results for Simulation IIIa	81
3.11	Comparison V (March 19, 8:23 UT)	83
3.12	Comparison VI (February 10, 9:51 UT)	86
3.13	Comparison VIII (March 4, 7:30 UT)	88
3.14	Factors that enhance Joule heating for Simulation VIIb over VIIa	90
3.15	Comparison X (February 10, 9:51 UT)	93
3.16	Comparison XI (March 14, 6:49 UT)	95
3.17	GEMINI versus TII flow comparisons for Simulations Ib and IVb	99
B.1	High-level flowchart for running a data-driven GEMINI simulation.	112
C.1	Comparison II (February 12, 10:22 UT)	115
C.2	Comparison IV (March 14, 6:49 UT)	117
C.3	Comparison VII (February 12, 10:22 UT)	119
C.4	Comparison IX (March 4, 10:14 UT)	121
C.5	Simulations Ia, VIIa, and Xa (February 10, 9:51 UT)	122
C.6	Simulation Ib (February 10, 9:51 UT)	123
C.7	Simulation VIIb (February 10, 9:51 UT)	124
C.8	Simulations Ia, VIIa, and Xa (February 10, 9:51 UT)	125
C.9	Simulation Xb (February 10, 9:51 UT)	126
C.10	Simulations IIa and VIIa (February 12, 10:22 UT)	127
C.11	Simulation IIb (February 12, 10:22 UT)	128
C.12	Simulation VIIb (February 12, 10:22 UT)	129
C.13	Simulations IIIa and VIIIa (March 4, 7:30 UT)	130
C.14	Simulation IIIb (March 4, 7:30 UT)	131
C.15	Simulation VIIIb (March 4, 7:30 UT)	132
C.16	Simulation IXa (March 4, 10:14 UT)	133
C.17	Simulation IXb (March 4, 10:14 UT)	134
C.18	Simulations IVa and XIa (March 14, 6:49 UT)	135
C.19	Simulation IVb (March 14, 6:49 UT)	136
C.20	Simulation XIb (March 14, 6:49 UT)	137
C.21	Simulation Va (March 19, 8:23 UT)	138

Chapter 1

Introduction

1.1 Background

1.1.1 The Magnetosphere

The earthly aurorae are a vibrant and dynamic visual signature at the atmospheric end of a complex interaction between the Sun's ever-outward-flowing magnetized plasma and the Earth's magnetic dynamo. Not unlike the standing wave trailing a stone in a river, this solar wind drags and distorts the Earth's nearly dipolar magnetic field into an elongated teardrop shape whose tail length is measured in 100s of Earth radii. Depending on the solar wind's pressure, velocity, density, and magnetic field orientation, this interaction can be fairly dynamic, generating energetic space weather which can affect our everyday lives. However, as luck would have it, the Earth's influence in this interaction is substantial and our planet plays a non-passive role in these dynamics, shielding us from certain solar wind tribulations. The region where this interaction happens, encompassed by the bow shock, is called our magnetosphere.

Figure 1.1 shows several components of the Earth's magnetosphere, including part of the aforementioned bow shock, the northern and southern tail lobes, the plasma sheet squeezed in between these lobes, and the auroral oval. The plasma sheet, which surrounds the magnetotail equatorial plane, is considered the source region for the type of aurora covered by this thesis, namely discrete auroral arcs. These arcs are less dynamic—even considered quasi-static—yet they can indicate the beginnings of substorms—a type of energetic space weather which can disrupt communications and power infrastructure—and it is therefore important for them to be understood. They are created by accelerated auroral electrons precipitating and impacting the neutral particles in the atmosphere which are atomically ex-

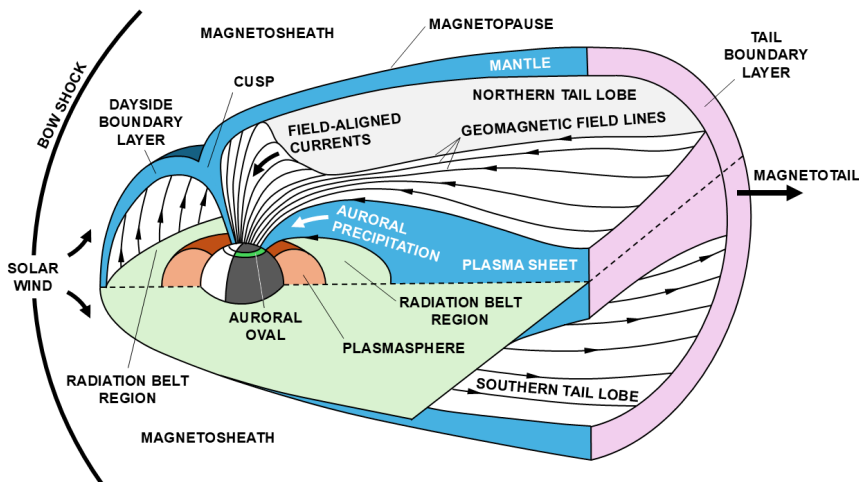


Figure 1.1: Overview of the magnetosphere. This figure is adapted from Figure 1.13 by Kelley (2009, continuing courtesy of J. Roederer).

cited causing photon emissions. This precipitation is indicated in Figure 1.1, flowing along magnetic flux tubes connecting the plasma sheet and the auroral oval.

Coinciding with this electron precipitation, there are field-aligned currents (FAC¹) which exist naturally in a deformed dipolar magnetic field configuration; bending magnetic field lines, even if curl-free to begin with, introduces additional curl which requires currents (Maxwell, 1865). The charged particles which constitute these currents have a high mobility parallel to the magnetic field lines compared to the perpendicular direction, which would not be a problem if it were not for the Earth physically obstructing their path. To avoid continuing charge build up, i.e. $\partial\rho/\partial t = 0$, at the ends of the flux tube, or in any particular spot for that matter, currents require closure and, as magnetic flux tubes cannot intersect (Maxwell, 1865), this means the currents are required to flow perpendicular to the field lines at some point. This is where the ionosphere, the region in the atmosphere containing plasmas, comes into play, and partly the reason why many in the space physics community focus on such a volumetrically minuscule part of this system. The ionospheric layer coincides with the thermosphere which contains neutral particles and the ionospheric charged

¹In this thesis, the acronym “FAC” is used for both field-aligned current and field-aligned current density.

particles start colliding with these neutrals when moving to lower altitudes. These collisions are what make perpendicular currents possible, making the ionosphere a crucial component in auroral current closure.

1.1.2 Quiet Discrete Auroral Arcs

Quiet discrete auroral arcs, often found in the evening to midnight sectors inside the auroral oval, are distinctive curtain-like aurorae that are in part defined by their accelerated electron precipitation (Knudsen et al., 2021). The mechanism that accelerates discrete auroral electrons is a parallel electric field which exists at around 1 – 2 Earth radii up the field lines (Temerin and Mozer, 1984), inside what is known as the auroral acceleration region.

A high-level explanation as to why steady-state parallel electric fields can form—not necessarily how—follows along with the explanation given by Temerin and Carlson (1998), and involves charge neutrality and particle continuity. Figure 1.2 shows a schematic view of an auroral flux tube connecting the plasmashell source region and the auroral oval. Temerin and Carlson (1998) take on the somewhat controversial assumption (see their Discussion section) of a steady-state ion density profile along this flux tube, $n_i(b)$, where $b = |B|/|B_1|$ is the coordinate along the flux tube, and B_1 and B are the magnetic field strengths at the ionospheric ($b = 1$) end of the flux tube and at some point along the flux tube respectively. This is to say that, on the transit time scales of the electrons, there is no parallel ion flow, $v_{i,\parallel} = 0$ and the density does not change with time. Now, particle continuity states that $n_e v_{e,\parallel} A$ remains constant, where the electron density $n_e(b)$, parallel electron flow, $v_{e,\parallel}(b)$, and cross-sectional area, $A(b)$, are all allowed to vary along b . In another way of looking at this, the FAC in this flux tube is $j_{\parallel} = -en_e v_{e,\parallel}$ and, given the definition of a flux tube, the magnetic flux is conserved, i.e. $AB = A_1 B_1$, where A_1 and A are the cross-sectional areas at the B_1 and B locations. This means that the linear current, $I_{\parallel} = j_{\parallel} A$, and j_{\parallel}/B are both also conserved along the flux tube.

Bringing into this charge neutrality, $n_e = n_i$, has both the solutions for $n_e(b)$ and $A(b)$ fixed. This requires $v_{e,\parallel}(b) = v_{e,\parallel,1} n_{i,1} \times b/n_i(b)$, and since $n_i(b)$ is relatively constant in the plasma sheet, and is certainly not proportional to b along the whole flux tube, it suggests there must be an acceleration mechanism along the flux tube somewhere. Ignoring gravity and parallel pressure gradients, the only other parallel force to consider is the mirror force, which depends on the geometry of the flux tube and the plasma's pitch angle distribution. This force pushes the electrons toward the plasmashell, hence there are situations where, in order for the solution $v_{e,\parallel}(b)$ to hold, there must a potential difference along the field lines accelerating the electrons against the mirror force to allow for them to reach the ionosphere and meet the flux tube current requirements—requirements

$$n_e(b)v_{e,\parallel}(b)A(b) \equiv \text{cnst}$$

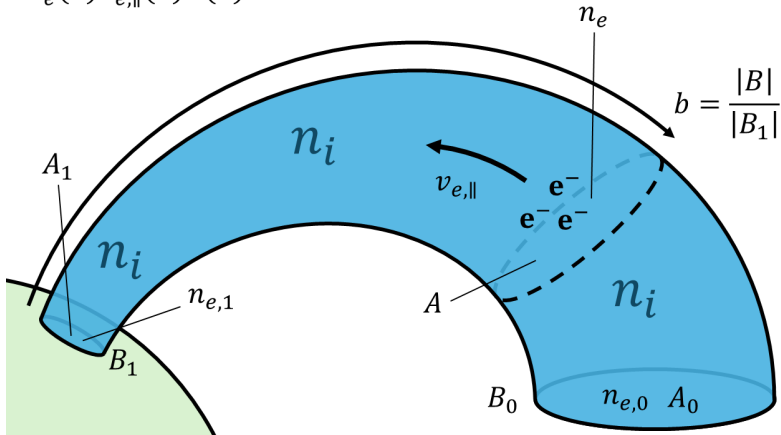


Figure 1.2: Magnetic flux tube connecting the plasmasheet and the auroral ionosphere. Subscript “1” refers to the ionospheric end where $b = 1$, while “0” refers to $b \rightarrow 0$ at the plasmasheet.

that may be set externally in the source region plasmashell.

It is a fair suggestion that a steady-state, zero flow ion density profile along the flux tube will not last long provided the same parallel electric field would accelerate the ions upward. But given that the ion response time can be much slower, this is a question of: “if not forever, then for how long can the electric fields be sustained?” Either way, herein lies the trouble with the steady-state approach, and one has to resort to solutions involving particle-wave interactions, transversely heating the ions, and/or shear stresses of magnetic field lines fracturing, but this moves us well past the scope of this thesis (see Knudsen, 2001; Haerendel, 1994, 2021, & references therein for more insights). The simple fact is that strong, sheetlike parallel electric fields have been observed (Temerin and Mozer, 1984; Ergun et al., 2002) lasting for several minutes with acceleration energies on the order of keVs—all aspects which are characteristic of quiet, quasi-static, discrete auroral forms.

A discussion about parallel electric fields would not be complete without mention of Knight (1973), who covers the relationship between auroral FAC and parallel potential drops from the perspective of electron velocity distributions, Liouville's theorem, and the conservation of energy and the first adiabatic invariant (something akin to what this thesis re-derives in Appendix A.2). Knight (1973) integrates the FAC phase space, $-ev_{e,\parallel}(f_0(\mathbf{v}_e) - f_1(\mathbf{v}_e))d^3v$, over electrons whose pitch angles and velocities

overcome the mirror force, and with velocity distributions at the ionosphere and plasmashell with respective temperatures, densities, and potentials. This provides a relationship between FAC at the ionospheric end and a parallel potential drop, given source region and ionospheric plasma parameters. Knight (1973) continues on by using this relation with typical values for these plasma parameters to show that a $20 \mu\text{A}/\text{m}^2$ FAC at the ionosphere requires a 6 kV potential drop for the range of conditions they consider.

The importance of the parallel potential drop and its role in impact ionization and ionospheric conductivity—and thus FAC closure—is covered in Chapter 3. This Chapter also focuses on the importance of the large-scale horizontal electric fields in the ionosphere, which requires knowledge about their origins. To understand these origins, one first needs to cover some fundamental concepts of auroral plasma physics, which is the topic of the following section.

1.2 Fundamental Concepts

1.2.1 Current Continuity

To understand electric currents, the community frequently resorts to work done by Maxwell (1865), who poses a set of relations between the charge distribution and current density, ρ and \mathbf{j} , and electric and magnetic fields, \mathbf{E} and \mathbf{B} :

$$\nabla \cdot \mathbf{E} = \frac{\rho}{\varepsilon_0}, \quad (1.1)$$

$$\nabla \cdot \mathbf{B} = 0, \quad (1.2)$$

$$\nabla \times \mathbf{E} = -\frac{\partial \mathbf{B}}{\partial t}, \quad (1.3)$$

$$\nabla \times \mathbf{B} = \mu_0 \mathbf{j} + \mu_0 \varepsilon_0 \frac{\partial \mathbf{E}}{\partial t}, \quad (1.4)$$

where ε_0 and μ_0 are the permittivity and permeability of free space. These equations are used as the basis for the understanding of electrodynamics and current closure in this thesis. Taking the divergence of Equation 1.4, dividing by μ_0 , and substituting in Equation 1.1, provides

$$0 = \nabla \cdot \mathbf{j} + \varepsilon_0 \frac{\partial}{\partial t} \nabla \cdot \mathbf{E} = \nabla \cdot \mathbf{j} + \frac{\partial \rho}{\partial t}, \quad (1.5)$$

which denotes the continuity of charges. In this thesis, however, the auroral arc systems have static charge distributions only, hence giving the luxury of dealing with divergence-free currents, i.e. $\nabla \cdot \mathbf{j} = 0$. The next section covers how electric and magnetic fields dictate plasma transport, and what this implies about electric currents.

1.2.2 High-Altitude Plasma Transport

Our regime exists at an altitude range where the charged particles inside Earth's plasmas go from being fully collisional with the neutral atmosphere, at around 80 km, to having virtually no collisions at all, at 200 km or higher, where the *E*-region transitions into the *F*-region ionosphere. From Kelley (2009, Chapter 2), the momentum conservation for an ionized species influenced by Earth's gravity, \mathbf{g} , the Lorentz force, and collisional momentum exchange reads

$$\rho_j \frac{d\mathbf{v}_j}{dt} = -\nabla p_j + \rho_j \mathbf{g} + n_j q_j (\mathbf{E} + \mathbf{v}_j \times \mathbf{B}) - \sum_{k,k \neq j} \rho_j \nu_{jk} (\mathbf{v}_j - \mathbf{v}_k), \quad (1.6)$$

where $d/dt \equiv \partial/\partial t + \mathbf{v}_j \cdot \nabla$, and ρ_j , \mathbf{v}_j , p_j , n_j , and q_j are the mass density, velocity, pressure, number density, and charge of species j , and ν_{jk} is the collision frequency of species j with k . Splitting the velocity and electric field into components perpendicular and parallel to the local magnetic field, i.e. $\mathbf{v}_j = v_{j,\parallel} \mathbf{b} + \mathbf{v}_{j,\perp}$ and $\mathbf{E} = E_{\parallel} \mathbf{b} + \mathbf{E}_{\perp}$, where $\mathbf{b} = \mathbf{B}/B$, with $B = |\mathbf{B}|$. Furthermore, at high latitudes, the assumption is made that gravity points in the direction of the magnetic field, i.e. $\mathbf{g} = g\mathbf{b}$, where $g = |\mathbf{g}|$, and that there are no perpendicular pressure gradients, i.e. $\nabla_{\perp} p_j = 0$. At higher altitudes, where collisions may also be ignored, this splits Equation 1.6 in two:

$$\rho_j \frac{dv_{j,\parallel}}{dt} = -\frac{\partial p_j}{\partial l} + \rho_j g + n_j q_j E_{\parallel}, \quad (1.7)$$

$$\rho_j \frac{d\mathbf{v}_{j,\perp}}{dt} = n_j q_j (\mathbf{E}_{\perp} + \mathbf{v}_{j,\perp} \times \mathbf{B}), \quad (1.8)$$

where l is the parallel coordinate. Focusing on the perpendicular equation, Equation 1.8, force balance reveals a fundamental concept about collisionless plasma transport

$$\mathbf{E}_{\perp} = -\mathbf{v}_{j,\perp} \times \mathbf{B} \implies \mathbf{v}_{j,\perp} = \frac{\mathbf{E} \times \mathbf{B}}{B^2}, \quad (1.9)$$

where the fact that $\mathbf{E} \times \mathbf{B} = \mathbf{E}_{\perp} \times \mathbf{B}$ is used. Note that all species, and more notably still, species of any charge, traverse in the same direction. This is known as *E-cross-B* drift—an essential concept in plasma physics. The fluid description of plasmas mimic what is known as the guiding-center motion of single particles moving in a constant electric and magnetic field, depicted in Figure 1.3. This same figure presents an important perspective of plasma, as will be shown later on.

To understand the motion of charged particles shown in Figure 1.3, let us take a step back and equate the centripetal force with the Lorentz force

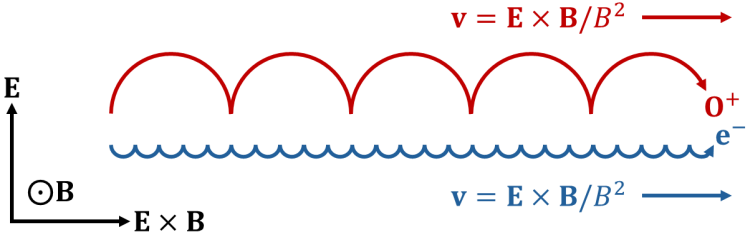


Figure 1.3: Examples of the $\mathbf{E} \times \mathbf{B}$ drift motion for singly-ionized oxygen (red) and an electron (blue). Both particles drift at the same velocity. Not to scale. Adapted from Figure 3.1 by Paschmann et al. (2003).

with no electric field:

$$q_j \mathbf{v}_j \times \mathbf{B} = -m_j \boldsymbol{\omega}_j \times (\boldsymbol{\omega}_j \times \mathbf{r}_j) = m_j \mathbf{v}_j \times \boldsymbol{\omega}_j \implies \boldsymbol{\omega}_j = \frac{q_j B}{m_j}, \quad (1.10)$$

with $\boldsymbol{\omega}_j$ and m_j being the angular velocity and mass of particle j with charge q_j . The frequency $f_{cj} = \omega_j/2\pi$ is a fundamental frequency of plasmas called the gyrofrequency. It, depending on the algebraic sign of the particle charge, circulates particles in one handedness or the other. Now let us say that this magnetic field exists inside a moving reference frame with velocity \mathbf{v} . Under the laws of special relativity, with $|\mathbf{v}| \ll c$, the electromagnetic fields in this frame are

$$\mathbf{E}' = \mathbf{E} + \mathbf{v} \times \mathbf{B}, \quad (1.11)$$

$$\mathbf{B}' = \mathbf{B}. \quad (1.12)$$

In our hypothetical case, $\mathbf{E}' = 0$, suggesting that there must be an electric field in the stationary frame that is $\mathbf{E} = -\mathbf{v} \times \mathbf{B}$. This tells us that an electric and magnetic field \mathbf{E} and \mathbf{B} acting on the motion of a charged particle is the equivalent of that particle undergoing simple cyclotron motion under \mathbf{B} in a reference frame moving at $\mathbf{v} = \mathbf{E} \times \mathbf{B} / B^2$ (Gurnett and Bhattacharjee, 2017, Section 3.2). The resulting trajectories, in the stationary frame, are those shown in Figure 1.3. One should be mindful, however, and remember that this is true for a constant magnetic field, in both space and time, for a reference frame that is moving at a constant velocity.

As a counter example to $\mathbf{E} \times \mathbf{B}$ drift, let us return to Equation 1.6 and move to higher altitudes still, where gravitational forces, in addition to collisions, may be ignored, so that the steady state gives us

$$0 = -\nabla p_j + n_j q_j (\mathbf{E} + \mathbf{v}_j \times \mathbf{B}). \quad (1.13)$$

Rearranging this to solve for \mathbf{v}_j , reveals an additional perpendicular drift:

$$\mathbf{v}_j - v_{j,\parallel} \mathbf{b} = \mathbf{v}_{j,\perp} = \frac{\mathbf{E} \times \mathbf{B}}{B^2} - \frac{\nabla p_j \times \mathbf{B}}{q_j n_j B^2}, \quad (1.14)$$

called the diamagnetic drift, $\mathbf{v}_{d,j}$; it being the latter term on the right-hand side. Unlike the $\mathbf{E} \times \mathbf{B}$ term, this drift is charge-dependent, which immediately points to the existence of a current,

$$\mathbf{j}_d = \sum_j n_j q_j \mathbf{v}_{d,j} = -\frac{1}{B^2} \sum_j \nabla p_j \times B = -\frac{\nabla p \times \mathbf{B}}{B^2}, \text{ where } p \equiv \sum_j p_j, \quad (1.15)$$

known as the diamagnetic current, \mathbf{j}_d (p here is the total pressure). This current is small in the ionosphere, yet it cannot go unmentioned in a study about current closure as it is the mechanism which sustains the current sheet in the magnetotail (Lui, 2018) sourced by lobe pressure gradients induced by the Solar wind (see Figure 1.1). It is the other end of our current circuit, and often considered one of the main electric generators in the context of this thesis.

In steady-state these perpendicular currents cannot pile up (see Equation 1.5)—any place these currents converge in the perpendicular direction must be met with equally spatially increasing field-aligned currents (FAC, j_{\parallel}):

$$\nabla \cdot \mathbf{j} = 0 \implies \frac{\partial j_{\parallel}}{\partial l} = -\nabla_{\perp} \cdot \mathbf{j}_{\perp}. \quad (1.16)$$

Equation 1.16 applies at the cross-tail current sheet as much as it does at the ionosphere, the lower altitudes of which are covered in the following section. This section unveils how the collisions between the constituents of plasmas and the neutral atmosphere affect plasma transport at lower altitudes.

1.2.3 Low-Altitude Plasma Transport

At altitudes around $80 - 200$ km, roughly defined as the ionospheric *E*-region, the plasma transitions to being fully collisional with the neutral atmosphere—the collision frequencies between ions and neutrals become comparable to those of the cyclotron motion depicted in Figure 1.3. To explain how this affects charged particle motion, we turn to a more pictographic view shown by Figure 1.5, in conjunction with Figure 1.4. As the neutral and plasma densities increase toward lower altitudes, the collisions between their constituents increase. Taking on Equation 2.29 by Kelley (2009), using parameters from an ionospheric simulation covered in Chapter 3 and Mass Spectrometer Incoherent Scatter radar data (MSIS, Emmert et al., 2021), Figure 1.4a shows that the collisions, for this instance, vary

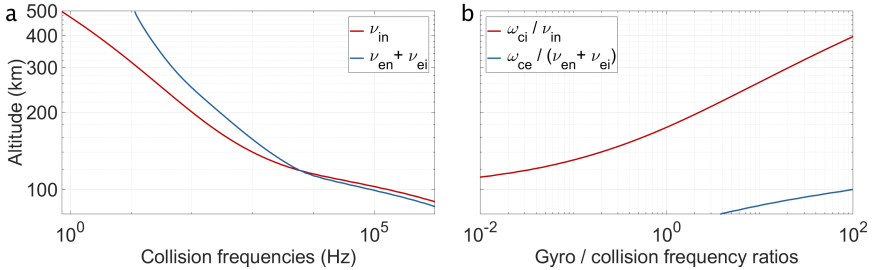


Figure 1.4: Transition altitudes for plasma collisions. (a) Altitude profiles of the collision frequencies of ions (red) and electrons (blue) of an ionospheric simulation from February 10, 2023. (b) The ratio between the cyclotron and collision frequencies for ions and electrons. Data source: <https://rcweb.dartmouth.edu/LynchK/Gemini3D> (simulation) and <https://rcweb.dartmouth.edu/LynchK/Gemini3D/> (MSIS).

from once to ten times per second at 500 km altitude, to a rate of 1 GHz at 80 km altitude. For ions, the ion-electron collisions are ignored as the electrons impart negligible momentum to the ions and thus virtually do not affect the ion trajectories.

What Figure 1.4b shows is how these collision frequencies compare to the cyclotron frequencies from Equation 1.10 with $B = 0.5$ G. At $\kappa_j = \omega_{cj}/\nu_j \sim 1$, on average, the charged particle's $\mathbf{E} \times \mathbf{B}$ guiding-center motion gets interrupted around once per revolution. For electrons, in this example, this happens below 80 km, while for the ions this happens at around 175 km. This suggests that, somewhere in between, exists a situation shown in Figure 1.5a.

Using an O⁺ ion and a N₂ molecule as examples, these collision-induced interruptions in cyclotron motion affect the overall drift of the ions—here, the oxygen ion both slows down and rotates toward \mathbf{E} while the electron, with its comparatively tiny cross-section, is continuing to $\mathbf{E} \times \mathbf{B}$ drift through the neutrals, without colliding.

Wherever there is a disparity between ion and electron motion, a current appears. Figure 1.5b shows how ion-neutral collisions create a gap between the ion and electron velocities, amounting to $\mathbf{v}_i - \mathbf{v}_e$ pointing somewhere between the \mathbf{E} and $\mathbf{b} \times \mathbf{E}$ directions. Panel c of this same figure shows the perpendicular current this creates. The component of this current that points in the direction of \mathbf{E} defines the Pedersen current (Pedersen, 1927), and the component directed toward $\mathbf{b} \times \mathbf{E}$ is known as the Hall current (Hall et al., 1879). It might seem strange that the latter of these currents was discovered just under a half-century earlier, but one can recognize that the Pedersen currents are equivalent to current traveling in a wire under a

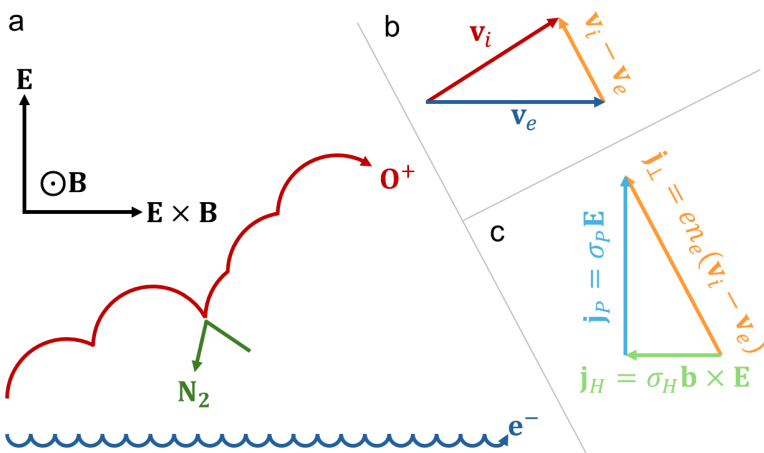


Figure 1.5: Schematic outline how ion-neutral collisions generate Pedersen and Hall currents. (a) pictographic representation of an oxygen ion (red) having its guiding center $\mathbf{E} \times \mathbf{B}$ drift interrupted by collisions with nitrogen molecules (green), while the electrons (blue) press on. (b) The resulting difference (orange) in drift velocities between the ions and electrons. (c) The perpendicular current this implies, split into the Pedersen (light green) and Hall (light blue) components. Panel a is adapted from Figure 3.1 by Paschmann et al. (2003).

potential difference—a wire which resists a portion of the electron motion imparted by the Coulomb force—a phenomenon known as Ohm’s law. This proportionality between the current and the electric field, $\mathbf{j} = \sigma \mathbf{E}$, where σ is the proportionality constant, was published by Georg Ohm in 1827; a full century prior to when Peder Pedersen postulated about currents in the upper atmosphere (Pedersen, 1927).

The specific coordinate system chosen to represent the perpendicular ionospheric currents, namely the \mathbf{E} and $\mathbf{b} \times \mathbf{E}$ directions, distinguishes the Pedersen from the Hall currents in matters of Joule heating. Simply put, the Pedersen currents produce Joule heating, $\mathbf{j}_P \cdot \mathbf{E} = \sigma_P |\mathbf{E}|^2$, while Hall currents do not, $\mathbf{j}_H \cdot \mathbf{E} = 0$, making them non-dissipative. This fact, in part, motivates the community to try and understand which closure currents are used in which situations.

Hinted at by Figure 1.5c, provided the linear physical relationship between collisions and the momentum they impart (see Equation 1.6), it can be shown (Kelley, 2009, Section 2.2) that, just like in the one-dimensional Ohm’s law, there is a proportionality between the Pedersen and Hall currents, and the electric field. These proportionality constants are the Pedersen and Hall conductivities, σ_P and σ_H . Similarly, in the parallel direction, there is the parallel conductivity σ_0 , i.e. $j_{\parallel} = \sigma_0 E_{\parallel}$, which invites a three-dimensional (3-D) description of Ohm’s law:

$$\mathbf{j} = \sigma \cdot \mathbf{E} = \begin{pmatrix} \sigma_P & -\sigma_H & 0 \\ \sigma_H & \sigma_P & 0 \\ 0 & 0 & \sigma_0 \end{pmatrix} \begin{pmatrix} \mathbf{E}_{\perp} \\ E_{\parallel} \end{pmatrix} = \sigma_0 E_{\parallel} \mathbf{b} + \sigma_P \mathbf{E}_{\perp} + \sigma_H (\mathbf{b} \times \mathbf{E}_{\perp}). \quad (1.17)$$

Kelley (2009) derives these conductivities for a ion-electron plasma in terms of physical constants and plasma parameters:

$$\sigma_0 = ne(b_i - b_e), \quad (1.18)$$

$$\sigma_P = ne \left(\frac{b_i}{1 + \kappa_i^2} - \frac{b_e}{1 + \kappa_e^2} \right), \quad (1.19)$$

$$\sigma_H = \frac{ne}{B} \left(\frac{\kappa_e^2}{1 + \kappa_e^2} - \frac{\kappa_i^2}{1 + \kappa_i^2} \right), \quad (1.20)$$

where $b_j = q_j/m_j \nu_{jn}$ is the mobility and where the (very good) assumption is made that the ion and electron densities are equal, i.e. $n = n_e = n_i$. At 200 km or so, Figure 1.4 shows the gyro-to-collision frequency ratios are $\kappa_i \sim 1$ and $\kappa_e \sim 10^4$, and $\nu_i \sim \nu_e$. This results in a mobility ratio of $b_e/b_i \sim 10^4$ for an atomic oxygen plasma, and leaves the parallel conductivity to be $\sigma_0/ne \approx -b_e \sim -10^8 \text{ T}^{-1}$. This tells us that the field-aligned currents are mainly because of electrons at this altitude. For the Pedersen conductivity, the b_i term cannot be ignored. On the contrary, the $\kappa_e/\kappa_i \sim 10^4$ deems the

b_e term negligible instead. This results in $\sigma_P/ne \approx b_i/2$. The b_i dependence is consistent with the perspective of Figure 1.5 in that, even though the ions are the less mobile ones, the collisions with the neutrals scale up the ions' ability to move in the direction of \mathbf{E} , while the electrons are much less able to move in this same direction because of their steadfast $\mathbf{E} \times \mathbf{B}$ drift.

Lastly, the Hall conductivity approaches $\sigma_H/ne \approx 1/2B$. The inverse magnetic field strength relation can be explained by the fact that, in the limit of negligible ion motion, the electrons will remain at their $\mathbf{E} \times \mathbf{b}/B$ velocity, which also has the inverse magnetic field strength relation.

Under these conditions, at 200 km altitude, the Pedersen-to-Hall conductivity ratio is $\sigma_P/\sigma_H \approx 3$. Going down further in altitude has the Hall conductivity overtake the Pedersen one, yet they remain to be at similar orders of magnitude. This results in a rotation of \mathbf{j}_\perp from parallel to perpendicular to \mathbf{E}_\perp , altering the morphology of how the perpendicular current closes with the FAC. In contrast, the parallel-to-Pedersen conductivity ratio of $\sigma_0/\sigma_P \sim 10^4$ might suggest that FAC closure with Pedersen currents might be unbalanced, but the parallel electric field is much less than the perpendicular one as shown by Farley Jr. (1959), which compensates for the conductivity imbalance. Assuming no parallel electric field in electrostatics implies an electric potential map that does not depend on the parallel direction, i.e. magnetic field lines in the ionosphere are equipotential lines, as pointed out by Farley Jr. (1959). This fact enables a beautiful, but dangerous, simplification of ionospheric current continuity, which is covered next.

1.2.4 Ionospheric Current Continuity

Once again looking at Equation 1.5, but now using the new-found ionospheric Ohm's law (Equation 1.17), it is seen that

$$\begin{aligned} -\frac{\partial j_\parallel}{\partial l} &= \nabla_\perp \cdot \mathbf{j}_\perp = \nabla_\perp \cdot (\sigma_P \mathbf{E}_\perp + \sigma_H (\mathbf{b} \times \mathbf{E}_\perp)) \\ &= \sigma_P \nabla_\perp \cdot \mathbf{E}_\perp + \mathbf{E}_\perp \cdot \nabla_\perp \sigma_P \\ &\quad + \sigma_H \nabla_\perp \cdot (\mathbf{b} \times \mathbf{E}_\perp) + (\mathbf{b} \times \mathbf{E}_\perp) \cdot \nabla_\perp \sigma_H. \end{aligned} \quad (1.21)$$

Momentarily taking on a cartesian coordinate system with perpendicular coordinates \mathbf{x} , \mathbf{y} , along with \mathbf{b} , has the third term on the right-hand side being

$$\nabla_\perp \cdot (\mathbf{b} \times \mathbf{E}_\perp) = \frac{\partial E_y}{\partial x} - \frac{\partial E_x}{\partial y} = -(\nabla \times \mathbf{E})_l = \frac{\partial B_\parallel}{\partial t}. \quad (1.22)$$

This is an inductive component, which is out-of-scope for this thesis as our focus is on persistent discrete arcs, so it is ignored. Now, the fact that

the electric field is independent of the parallel coordinate suggests, at high latitudes, a straightforward integration of Equation 1.21 over the altitudinal coordinate, $z = -l$. Most of the Pedersen and Hall conductivities are captured in an altitude range of 80 – 500 km and the magnetic field lines are relatively straight and antiparallel to \mathbf{z} here. This gives us, following Kelley (2009),

$$\int \frac{\partial j_{\parallel}}{\partial z} dz = \int \sigma_P dz \nabla_{\perp} \cdot \mathbf{E}_{\perp} + \mathbf{E}_{\perp} \cdot \nabla_{\perp} \int \sigma_P dz + (\mathbf{b} \times \mathbf{E}_{\perp}) \cdot \nabla_{\perp} \int \sigma_H dz, \quad (1.23)$$

where the parallel integration is passed through the operands of the perpendicular del operator, as these operations commute. Defining the Pedersen and Hall conductances, Σ_P and Σ_H , as the respective height-integrated conductivities gives the 2-D, horizontal relation between them, the FAC, and the perpendicular electric field:

$$j_{\parallel} = \Sigma_P \nabla_{\perp} \cdot \mathbf{E}_{\perp} + \mathbf{E}_{\perp} \cdot \nabla_{\perp} \Sigma_P + (\mathbf{b} \times \mathbf{E}_{\perp}) \cdot \nabla_{\perp} \Sigma_H. \quad (1.24)$$

This description of current continuity and Ohm's law is ubiquitous in auroral plasma physics, but it requires the privilege of knowing the 2-D conductance "maps", i.e. east-north dependent quantities. The Pedersen and Hall conductivities depend on many plasma parameters, particularly the electron density and temperature; two factors controlled by the fluid equations not yet looked at: the conservations of mass and energy density. For example, source terms for electron density include Solar and impact ionization, while loss terms include recombination. In terms of energy, there is Joule heating and various heat fluxes that affect the electron temperature.

Even though the 2-D description by Equation 1.24 holds, the fluid equations are 3-D, and thus, so are the conductivities. This is especially true in the presence of electron precipitation from discrete auroral arcs that cause significant impact ionization. This ionization varies in altitude, as well as horizontally, creating 3-D electron density enhancements—enhancements that can be transported and that are subject to ionospheric chemistry. The arc precipitation itself might vary in time, where the recombination and transport time of the newly ionized species is non-negligible in some auroral arc motions, leaving behind a hysteresis of density enhancements. Furthermore, Pedersen currents cause Joule heating which enhances the electron temperature, in turn affecting the Pedersen conductivity potentially causing a feedback loop. Herein lies the complexity of the conductance maps—this is without even mentioning neutral wind effects, which are outside of the scope of this thesis.

Next, with the knowledge of collisionless plasma transport and the general, fundamental perspective of the physical system surrounding auroral currents, we consider the magnetospheric plasma convections and the effect they have on the auroral ionosphere.

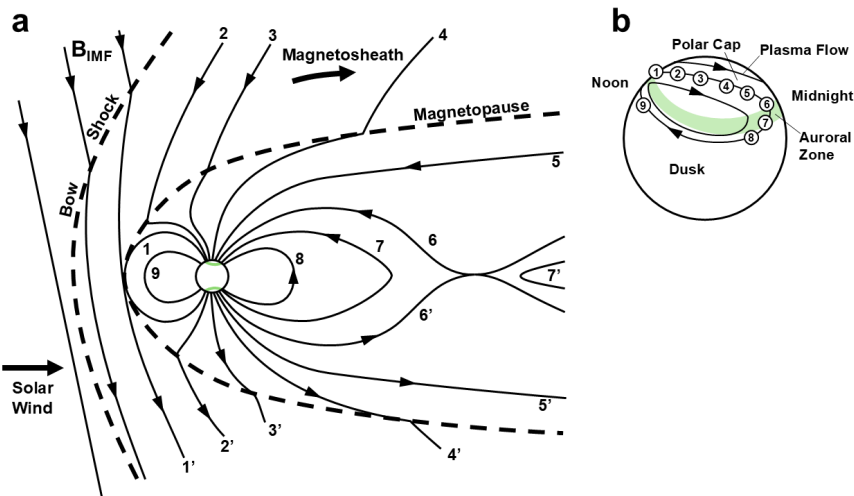


Figure 1.6: The Dungey cycle and its electric field mapping to the Earth’s ionosphere. Adapted from Figure 9.11 by Kivelson and Russell (1995)

1.3 Frozen-In Flux, Electric Field Mapping, & the Dungey Cycle

Alfvén (1943) outlines the fact that a magnetic flux tube containing plasma with infinite conductivity will hold onto that plasma as it travels through space. This is known as *Alfvén’s*, or the *frozen-in flux*, theorem. Were such a tube to move with velocity \mathbf{v} and contain a magnetic field \mathbf{B} , then it must also carry an electric field $\mathbf{E} = -\mathbf{v} \times \mathbf{B}$. In the limit of infinite parallel conductivity, there exists no parallel electric field which also means that the electric field on one end of the flux tube, lying perpendicular to the tube, can be mapped to the other end, or at least until the infinite parallel conductivity assumption becomes invalid.

A consequence of this, is that the large-scale convective motions of the plasma in the magnetosphere are imprinted onto the ionosphere, along with their electric fields. Such large-scale electric fields are a crucial part in the closing of FACs surrounding discrete auroral forms—a key point of Chapter 3. Dungey (1961) has outlined what these large-scale convections look like when driven by the solar wind, how they subsequently evolve through the magnetosphere, and how the resulting electric fields map to the ionosphere. Figure 1.6 provides a schematic overview of this cyclic system, named the Dungey cycle.

Parcels of solar wind plasma continuously stream past the Earth. For the sake of simplicity, suppose the magnetic field of a particular parcel points southward. It penetrates our bow shock and (1) meets the Earth's magnetic field on the dayside equatorial plane. Here, the two magnetic fields point in opposite directions resulting in a reconnection of the field lines². Immediately after, (2) the resulting magnetic flux tube connects the solar wind and the Earth, comprised of what are known as open field lines, and has a sharp bend sustained by the plasma interactions at the magnetopause. (3) The flux tube straightens out because of magnetic tension and gets dragged antisunward by the solar wind. (4) It continues to move toward the tail side inside the magnetosheath, again sharply bending at the bow shock. (5) The flux tube stretches for many Earth radii and moves toward the equatorial plane, putting magnetic pressure on the northern and southern tail lobes (see Figure 1.1). The same evolution applies to the southern flux tube that has reconnected to the solar wind on the dayside, shown with points 1' – 5'. This draping of magnetic flux tubes to the tail continuous, and more and more pressure pushes the northern and southern field lines closer toward the equatorial plane, where they, again, point in opposite directions. (6) This causes reconnection to happen again, now on the night side, but with no magnetopause to sustain the sharp bend in the newly connected closed flux tubes. (7) This has the new flux tube snap earthward under magnetic tension, carrying with it plasma from the plasmashell. (8) Through a spectacular auroral display, the flux tubes have dipolarized.

This is a good moment to point out the auroral oval perspective depicted by Figure 1.6b which shows the magnetic field line mapping of points 1 – 9 to the ionosphere. From points 1 – 6, the flux tubes are open to the solar wind and move antisunward—directly from the dayside to the nightside—across the polar cap. Points 6 – 8 are inside the auroral oval, here defined as the line/point where the flux tubes go from being to open to closed, to where the field lines are dipolar again. The flux tubes quickly lower in latitude during this dipolarization and, while they would stay in the nightside at this latitude, they cannot all fit. The increased nightside magnetic flux causes a magnetic pressure that convects the flux tubes both east- and westward, at this lower latitude, until they ultimately (9) replenish the missing flux on the dayside. This completes the Dungey cycle, and the pattern repeats for as long as the solar wind provides an anti-parallel component to the Earth's dayside magnetic field.

Figure 1.7 shows the top view of Figure 1.6b, looking down at the north-

²The theory surrounding magnetic reconnection is fruitful and abundant. It is the result of intense current sheets that form between anti-parallel magnetic fields to such an extent that even negligible resistivity starts to play a role, subsequently breaking the frozen-in condition of an infinitely conducting plasma (Pers. Comm. M. D. Zettergren).

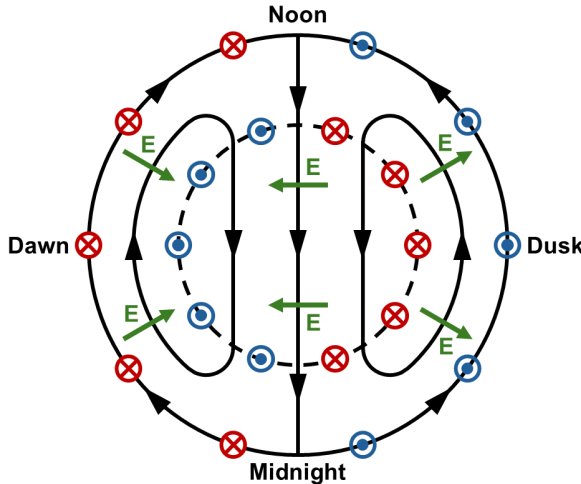


Figure 1.7: Top view of the Dungey cycle showing the related, large-scale convection (black) and electric fields (green), as well as the upward (blue) and downward (red) FACs. Adapted from Figure 1 by Cowley (2000).

ern polar cap and showing the two-cell convection pattern caused by the Dungey cycle. The magnetic field here points into the page, which gives rise to the large-scale electric fields shown in green ($\mathbf{E} = -\mathbf{v} \times \mathbf{B}$). In our regime, the roughly pre-midnight auroral oval, the electric field points mainly northward and the large-scale convection flows westward. To be self-consistent with these electric fields, and the Pedersen currents that flow along them, the FACs are directed upward wherever there is an electric field convergence, and downward where the electric field diverges. These are the Birkeland currents, named after Kristian Birkeland (Jago, 2001).

The relationship between the ionospheric plasma flow and the convection electric fields can be impacted by the dragging of this plasma behind the convective flow because of friction with the neutrals (Milan et al., 2017), however this is outside the scope of this thesis. How to incorporate the effects of neutral drag and the neutral wind as an electric generator is discussed in the future work section, Section 4.2, of this thesis.

In this thesis, situations are addressed where this large-scale perspective of FAC closure with global-scale electric fields, albeit providing crucial information to the encompassing systems, breaks down at auroral scales of ones to tens of kilometers. The Birkeland current requirements in the nightside can happen in flux tubes too tenuous to fulfill this need without the creation of parallel electric fields (see Section 1.1.2). As will be covered in Chapter 3 (and Appendix A.2), this causes accelerated electron precip-

itation to a point where the neutral atmosphere ionizes from their energetic impact, which can enhance both the Pedersen and Hall conductivities greatly—significantly more than the nightside radiative and unaccelerated impact ionization—such that these sheets of accelerated electrons largely dictate the auroral current connectivity. Herein lies the fascination of quiet discrete auroral arcs: they tell the story of how an electric circuit the size of the Earth several times over is affected by dancing curtains of light only several kilometers across.

1.4 Thesis Statement & Outline

The scope of this thesis encompasses the ability to determine geophysical, self-consistent solutions to the full ionospheric current continuity equation, Equation 1.21, for non-ideal discrete auroral arcs—ones that possess structure in the across-arc direction, but also in the along-arc and field aligned directions. The approach includes using state-of-the-art ionospheric three-dimensional modeling as a tool to provide insight into the role that the ionosphere plays in magnetosphere-ionosphere coupling for less idealized auroral events. This thesis explores how to (a) properly drive such simulations of auroral arc systems using two-dimensional electrostatic, continuous top-boundary conditions from distributed, multi-platform datasets, and (b) how sensitive these system solutions are to various driver parameters. This provides a better understanding of the dominant physics behind auroral arc current closure as well as related Joule heating. In particular, this thesis aims to determine the portions of field-aligned currents that are closed by Pedersen currents, which produce Joule heating, versus Hall currents, which are non-dissipative, giving insight into the extent to which the ionosphere acts as a load to a magnetospheric generator. This thesis addresses the following science questions (SQ) and objectives (SO):

- SQ 1: What self-consistency constraints exist in creating a geophysically coherent set of F-region quasistatic discrete auroral system drivers?
- SQ 2: What understanding of auroral system science can be gained by investigating the 3-D morphology of ionospheric current closure?
- SQ 3: What degree of along-arc structure significantly breaks the sheetlike discrete auroral model and what auroral features are most sensitive to this structure?
- SO 1: Develop a public catalog of data-driven 3-D auroral arc system simulations that illustrate non-idealized, non-sheetlike morphologies.
- SO 2: Develop infrastructure to systematically drive and query the GEMINI ionospheric model such that the catalog can be easily expanded upon.

Chapter 2 of this thesis is the first of two manuscripts, and it outlines the shortcomings of using one-dimensional, across-arc auroral data tracks when driving 3-D auroral simulations which require two-dimensional input maps. Three methods are provided for the mitigation of this issue which use multi-spectral all-sky imagery. The imagery provides information on how these data tracks can be extrapolated in a meaningful way.

The second manuscript, Chapter 3, applies the replication method outlined in Chapter 2 in full force. A total of 17 data-driven auroral arc system simulations, covering six different satellite-imagery conjunction events of quiet discrete aurorae, are covered using observations from multiple space-craft, radars (high-frequency network and incoherent scatter), and multi-spectral all-sky imagers. These simulations are iterated through different configurations of large-scale background electric fields, assumptions about accelerated versus unaccelerated electron precipitation, and along-arc FAC structure as well as the validity of the replication method used.

Chapter 4 summarizes the conclusions from Chapters 2 and 3, and follows with a discussion about how the work covered in this thesis can be expanded upon, and how the tools developed here can contribute to further research of auroral arc systems. It has been a major objective of this thesis to, not just commit to providing the scientific community substantial knowledge about current closure surrounding discrete aurorae, but also to set up for future research with a smooth transition.

Appendix A covers the derivation of a two-variable, most general polynomial harmonic function used in the plasma flow replication methodology outlined in Chapter 2, and the derivation of accelerated bi-Maxwellian differential number flux used in Chapter 3 for imagery inversion and electron precipitation methods. Appendix B covers instructions and a high-level flowchart overview of the data preparation, the replication algorithm, simulation driver preparation, and visualization tools used in this thesis, and Appendix C is the Supporting Information for the manuscript in Chapter 3. It covers simulation comparisons left out of this manuscript as well as a summary of the isometric, top, and side views of the simulations presented in this thesis.

Chapter 2

Generation of Top-Boundary Conditions for 3-D Ionospheric Models Constrained by Auroral Imagery and Plasma Flow Data

J. van Irsel¹, K. A. Lynch¹, A. Mule¹, M. D. Zettergren²

¹Dept. of Physics and Astronomy, Dartmouth College, Hanover, NH; ²Physical Sciences Dept., Embry-Riddle Aeronautical University, Daytona Beach, FL

This chapter is adapted almost verbatim, with minor formatting and stylistic modifications, from a manuscript under the same title (van Irsel et al., 2024) which is published in the Journal of Geophysical Research: Space Physics (<https://doi.org/10.1029/2024JA032722>). The majority of contributions to this manuscript are by J. van Irsel. Contributions from coauthors include, in large part, review and editing. Specific contributions are mentoring, science guidance, supervision, and funding acquisition by K. A. Lynch, the conceptualization of Appendix A.1 by A. Mule, and modeling and software support by M. D. Zettergren.

Key Points:

- We provide three methods for developing ionospheric convection flow maps from limited data tracks in conjunction with auroral imagery
- Methods for generating distributed plasma flow surrounding auroral arcs can benefit from auroral arc information provided by all-sky imagery
- Modeling realistic auroral current closure needs drivers that vary along-arc, across-arc, and in altitude via electron precipitation spectra

Abstract

Data products relating to auroral arc systems are often sparse and distributed while ionospheric simulations generally require spatially continuous maps as boundary conditions at the topside F -region ionosphere. Fortunately, all-sky auroral imagery can provide information to fill in the gaps. This paper describes three methods for creating electrostatic plasma convection maps from multi-spectral imagery combined with plasma flow data tracks from heterogeneous sources. These methods are tailored to discrete arc structures with coherent morphologies. The first method, “reconstruction”, builds the electric potential map (from which the flow field is derived) out of numerous arc-like ridges that are then optimized against the plasma flow data. This method is designed for data from localized swarms of spacecraft distributed in both latitude and longitude. The second method, “replication”, uses a one-dimensional, across-arc flow data track and replicates these data along a determined primary and secondary arc boundary while simultaneously scaling and rotating to keep the flow direction parallel to the arc and the flow shear localized at the arc boundaries. The third, “weighted replication”, performs a replication on two data tracks and calculates a weighted average between them, where the weighting is based on data track proximity. This paper shows the use of these boundary conditions in driving and assessing 3-D auroral ionospheric, multi-fluid simulations.

Plain Language Summary

The aurorae, or northern and southern lights, are embedded within a complicated system of interacting electric fields, magnetic fields, and charged particles, the more energetic of which produce the lights themselves by exciting the neutral atmosphere. This brings about a 3-D electric current system. These currents enter and exit the atmosphere along the Earth's magnetic field lines, and can only close their circuit between 80 and 150 km. This paper outlines the importance of simulating auroral arc systems in 3-D and thus the need for generating continuous, horizontal, top-boundary drivers for these simulations. This is difficult as the available data products are limited. This paper provides three methods for creating these boundary conditions using multi-color, all-sky auroral imagery in conjunction with approximately across-arc plasma flow data tracks provided by spacecraft, sounding rockets, and/or radar measurements.

2.1 Introduction

2.1.1 Motivation

Measurements of auroral arc systems are often sparse, heterogeneous (i.e. multi-sourced), and distributed, yet volumetric ionospheric simulations generally require spatially continuous, two-dimensional (2-D) boundary conditions on the top surface of the model space. Moreover, ionospheric plasma datasets commonly provide no more than one or two tracks of dense one-dimensional (1-D) data, leaving little to no information on variations along the orthogonal directions. Information about these morphologies is something that all-sky imagery can provide.

This paper discusses the development and application of three methods for creating spatially continuous, topside ionospheric, electrostatic plasma convection maps from distributed optical data, provided by all-sky, multi-spectral imagery, combined with plasma flow data tracks, provided by spacecraft, sounding rockets, and/or radar measurements. These methodologies focus on typical sheet-like discrete auroral arc structures with high across- to along-arc gradient ratios. Furthermore, this paper shows the use of these boundary conditions in driving and assessing three-dimensional (3-D) auroral ionospheric simulations.

The understanding of auroral-arc-scale system science plays an important role in interpreting magnetosphere-ionosphere (MI) coupling, the ionospheric end of which itself involves an ongoing sequence of system science studies (Wolf, 1975; Seyler, 1990; Cowley, 2000; Lotko, 2004; Fujii et al., 2011, 2012; Marghitu, 2012; Khazanov et al., 2018; Clayton et al., 2019, 2021; Yano and Ebihara, 2021; Lynch et al., 2022; Enengl et al., 2023; Wang et al., 2024). MI coupling studies near auroral arcs demand self-consistent (per Equation 2.1), topside ionospheric maps of field-aligned current (FAC) and convection plasma flow consistent with a 3-D ionospheric conductivity volume created by charged-particle, auroral precipitation and sunlight. The auroral ionosphere plays a non-passive role in this coupling; even with electrostatics, the arrangement of flows and time-dependent precipitation implies evolving conductivity making the system quasi-static at best. At high latitudes, the height-integrated relation between quasi-static convective flow, FAC, and conductances is (Kelley, 2009, Equation 8.15):

$$j_{\parallel}(x, y) = \Sigma_P \nabla_{\perp} \cdot \mathbf{E} + \mathbf{E} \cdot \nabla_{\perp} \Sigma_P + (\mathbf{b} \times \mathbf{E}) \cdot \nabla_{\perp} \Sigma_H, \quad (2.1)$$

where (x, y) is the plane orthogonal to the local magnetic field, j_{\parallel} is the ionospheric topside FAC, $\Sigma_{P,H}$ are the height-integrated Pedersen and Hall conductivities, i.e. conductances, \mathbf{E} is the ionospheric electric field, and $\mathbf{b} = \mathbf{B}/B$ is the magnetic field direction. This explains, in the absence of induction, how magnetospheric currents and convection patterns couple to

the ionosphere given height-integrated conductivity maps using ionospheric Ohm's law and current continuity. Yano and Ebihara (2021), however, have pointed out that integrating out altitudinal effects can hide significant information regarding polar ionospheric systems. Altitude dependent, finite recombination times, together with plasma transport, can produce 3-D electron density structures providing an auroral precipitation hysteresis in conductance maps. Moreover, the 3-D conductivity volume is highly sensitive to auroral precipitation by means of impact ionization, as the precipitation energy spectra determine ionization rate profiles that are altitude dependent (Fang et al., 2008, 2010). Altitudinal effects aside, the third term in Equation 2.1 is typically ignored and in some cases, where the ionosphere is modeled as a slab of constant conductance, the second term is ignored as well. For better understanding of MI coupling, it is important to study the full 3-D system when looking at FAC closure influenced by auroral precipitation that is both geophysical and self-consistent with plasma convection. Hence, we need ionospheric simulations that look at the full 3-D current continuity equation, an engagement that requires spatially continuous top-boundary input maps.

Both Equation 2.1 and topics discussed in this paper deal with self-consistency, not causal relationships, when finding solutions to auroral current continuity. Hypotheses can be made on causality through intuition, but cannot be proven within the framework outlined in this paper.

2.1.2 Background

The problem of extrapolating convection flow observations into continuous maps is not new. Nicolls et al. (2014) undertake the mapping (or “imaging”) of electric field distributions using line-of-sight (LOS) plasma flow measurements from a single, multibeam incoherent scatter radar (ISR). They outline a regularized least-squares fitting algorithm which takes direct LOS flow measurements, along with their measurement error, and produces an electric potential map. This is a difficult feat in that a single LOS measurement only carries information on one component of the electric field; multistatic beams are required to estimate the full vector field without regularization assumptions. Part of their regularization minimizes the mean squared curvature of the potential field which results in smoother solutions and minimizes gradients isotropically, something not well suited near sheet-like auroral arcs with large across-arc conductance gradients.

Bristow et al. (2016) approach a similar problem but with multiple HF radars by using Local Divergence-Free Fitting (LDFF), as opposed to a global divergence-free constraint. They impose the local constraint of divergence-free plasma convection and treat this in the same way that they do the constraint introduced by the decomposition of two LOS measure-

ments. This prevents unnecessary smoothing of sharp localized gradients (i.e. near the edges of arcs in the across-arc direction), maintaining the fine structure of the observations wherever possible. This method, which takes advantage of the broad multistatic coverage of SuperDARN, does not incorporate associated information from auroral imagery. It provides an informative counterpoint to the methods outlined in this paper.

Laundal et al. (2022) describe methodology for the “Local mapping of polar ionospheric electrodynamics” (Lompe). This is an assimilative tool that gathers relatively dense, heterogeneous observational data and performs a regional mapping of the electrodynamics in the polar ionosphere. They use Spherical Elementary Current Systems (SECS, Amm, 1997) instead of the more global spherical bases used by other assimilative tools like the Kamide-Richmond-Matsushita (KRM, Kamide et al., 1981) and the Assimilative Mapping of Ionospheric Electrodynamics (AMIE, Richmond and Kamide, 1988) methods, which allows more flexibility with spatial scales. Lompe, in its default configuration, includes a means to penalize gradients along either direction, but not along arbitrary contours. Further, it defaults to using smooth background conductance patterns derived from a statistical model which do not capture the variations from arc-scale structures.

For ideal, sheet-like auroral arcs, often only the first term in Equation 2.1 is considered. In order to address the effects of strong and anisotropic conductivity gradients in the vicinity of auroral arcs, this paper presents, first, a formalization of techniques developed during the Phase A Concept Study Report (CSR) for the Auroral Reconstruction CubeSwarm (ARCS) mission proposal (Lynch et al., 2024b; Erlandson et al., 2024) and second, an extension of techniques developed by Clayton et al. (2019, 2021). We provide methodologies for the continuous mapping of plasma flow data tracks which focus on auroral physical and gradient scale lengths, and discrete sheet-like morphologies, and we use such maps as top-boundary drivers for 3-D ionospheric simulations.

Section 2.2 describes the reconstruction, replication, and weighted replication methodology along with example usages of each. Section 2.3 outlines and compares two 3-D auroral multi-fluid simulations driven by the plasma flow maps derived by the replication method in Section 2.2.2. In section 2.4 we discuss our results and provide cautionary remarks, and in Section 2.5 we conclude this work and outline how these tools can be used in the future.

2.2 Methodologies

We outline three methods for developing continuous topside ionospheric plasma flow maps from limited remote sensed or *in situ* flow data tracks collected in conjunction with auroral imagery. Section 2.2.1 outlines the first

methodology, coined “reconstruction”, which stems from a multi-CubeSat mission study (Lynch et al., 2024b). This report proposes an arrayed, localized swarm of spacecraft spanning both multiple latitudes *and* longitudes, i.e. a “CubeSwarm”. The reconstruction method prioritizes flow representation interior to the swarm array which is consistent with auroral imagery, and extrapolates into regions beyond using information from the imagery. It builds the flow map using a pseudo-basis set of electric potential ridges, thus ensuring electrostatic (divergence-free) flow. These ridges follow some definition of a single auroral arc boundary determined using morphological features of all-sky, multi-spectral imagery or, in some cases, maps of FAC from the swarm itself. This pseudo-basis set is not orthonormal nor complete (Griffiths, 2017, Chapter 3), but the set of arc-aligned ridge functions provides a useful representation of our potential surface using a finite number of parameters. The left column of Figure 2.1 outlines the geographical context of the Observing System Simulation Experiment (OSSE) used in Lynch et al. (2024b) to demonstrate the reconstruction technique. The data volume provided by this OSSE is sampled by a virtual spacecraft swarm to provide multi-point, hypothesized *in situ* plasma flow data.

The second method, “replication”, outlined in Section 2.2.2, extends related methodology used by Clayton et al. (2019, 2021) who use data from the Isinglass sounding rocket campaign in conjunction with imagery from the UAF Geophysical Institute’s Poker Flat Digital All-Sky Camera (DASC, Conde et al., 2001). This method makes use of plasma flow data from a single auroral arc crossing, whether from a sounding rocket (Clayton et al., 2019, 2021), spacecraft (Archer et al., 2017), or ISR (Kaepller et al., 2023). In the present work, the data are replicated, scaled, and rotated in accordance with *two* auroral arc boundaries, again, determined through all-sky imagery features. After this, electrostatics is enforced. The right column of Figure 2.1 shows the geographical context of the simulation used to demonstrate the replication technique.

The third method, a permutation of the second, named “weighted replication”, is outlined in Section 2.2.3 and uses two data tracks in conjunction with all-sky imagery. This method repeats part of the replication methodology for each data track and then performs a weighted averaging on the interpolated flow maps (prior to enforcing electrostatics) with the weighting being based on the geometric distances to either data track.

In all three methods, one of the main difficulties in creating a continuous plasma flow map lies in the constraint that it is divergence-free, i.e. electrostatic since $\mathbf{v} = \mathbf{E} \times \mathbf{B}/B^2 \implies B\nabla \cdot \mathbf{v} = \nabla \times \mathbf{E}$. Vector velocity fitting algorithms exist which handle this constraint (Ruohoniemi et al., 1989; Nicolls et al., 2014). However, such algorithms will often create large flow vortices (diverging electric fields) which in our case act as spurious sources and sinks of FAC. Separately, SECS are widely used in fitting for

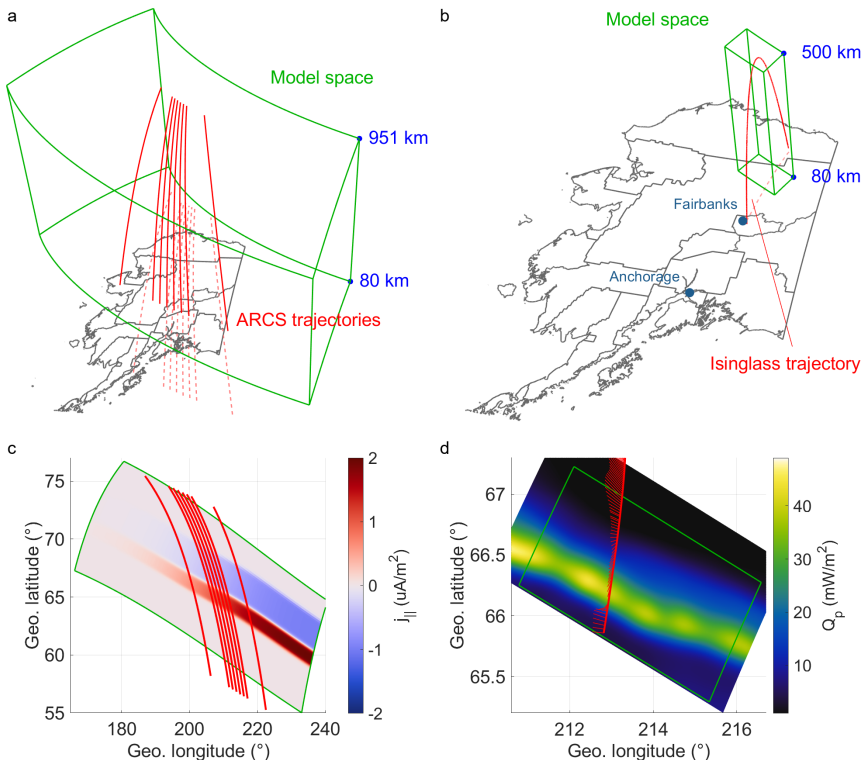


Figure 2.1: Geographical context relating to the simulations used in demonstrating the reconstruction and replication methods. (a) The 3-D simulation model space (green) and the ARCS trajectories (red), along with their ground tracks (red, dashed), in reference to Alaska. (b) Same as panel a but with the Isinglass trajectory. (c) Topside ionospheric FAC simulation driver (colormap) in reference to the model space (green) and ARCS orbits (red). (d) Total precipitating energy flux (colormap) and plasma flow data (red) in reference to the model space (green outline). Data source: <https://rcweb.dartmouth.edu/LynchK>.

divergence-free and curl-free fields (Amm, 1997; Vanhamäki and Juusola, 2020), often for reconstructing currents out of magnetic field measurements. In this paper, we use locally Cartesian coordinates and explicitly incorporate additional information obtained from auroral imagery into the vector flow fitting.

2.2.1 Reconstruction

This section provides a proof-of-concept reconstruction using an OSSE (using background conditions from February 1, 2015 at 10 UT, 23.2 MLT) from Lynch et al. (2024b) wherein a localized “CubeSwarm” of virtual spacecraft generate synthetic data from the 3-D auroral arc simulation as they orbit through (see Figure 2.1a). The simulation used in this section is data-inspired (Wu et al., 2017), but idealized; it is driven with a top-boundary map of a single pair of mostly east-west aligned FAC sheets with a slight bend in their profile and the amplitudes of which fade westward from ± 1 to $0 \mu\text{A}/\text{m}^2$ over the span of the model space (see Figure 2.1c). The associated auroral arc precipitation input maps are of a similarly shaped arc embedded within the poleward FAC sheet peaking at an energy flux of $3 \text{ mW}/\text{m}^2$ and characteristic energy of 3 keV with gradient scale lengths of 40 km.

Reconstruction Algorithm

We construct the electric potential map out of a sum of a user-defined number, N_k , of east-north dependent pseudo-basis functions, ϕ_k , each governed by a set of parameters. The functional form for each of them is an inclined Gaussian ridge, i.e. a Gaussian profile northward that extrudes east- and westward with a constant sloped amplitude while following the curved boundary of the arc. This is done to find electric potential solutions that prioritize across-arc gradients while remaining relatively unstructured along the arc. The $\mathbf{E} \times \mathbf{B}$ plasma flow derived from this potential field is then compared against the virtual plasma flow data and the mean square difference is minimized over the parameter space to find an optimal set of ϕ_k .

The arc boundary is determined by applying a standard Sobel edge detection algorithm (Sobel, 2014) to the all-sky imagery derived Pedersen conductance. Given the idealistic nature of the OSSE used in demonstrating this method, this suffices, but we caution the reader regarding the complexities of determining less idealized arc boundaries. After determining an appropriate set of boundary points, they are least-squares fit against the

following functional form:

$$b(x; \bar{A}) = \sum_{j=1}^{N_j} \left[A_{j1} + A_{j2} \tanh\left(\frac{x - A_{j3}}{A_{j4}}\right) \right], \quad (2.2)$$

with b the arc boundary, \bar{A} the $N_j \times 4$ fitting boundary parameter matrix, N_j the user-defined number of summation terms, and x the linear magnetic east coordinate. Throughout this manuscript, the coordinates x , y , and z refer to linear magnetic east, north, and anti-parallel in the northern hemisphere. The reason for the choice of summing hyperbolic tangents lies in the tendency of auroral arcs to be aligned magnetic east-west and to be relatively unstructured in this direction.

With this, we define our pseudo-basis potential ridge as

$$\phi_k(\mathbf{r}; \bar{P}, \bar{A}) = (P_{k1}x + P_{k2}) \exp\left[-\frac{(y - P_{k3} - b(x; \bar{A}))^2}{P_{k4}^2}\right], \quad (2.3)$$

where \bar{P} is the $N_k \times 4$ potential parameter matrix, giving a total electric potential field of

$$\phi(\mathbf{r}; \bar{P}, \bar{A}) = \sum_{k=1}^{N_k} \phi_k(\mathbf{r}; \bar{P}, \bar{A}). \quad (2.4)$$

We use these functional forms as they are differentiable and because they capture features that are empirically similar to those found in discrete auroral arcs. Parenthetically, prior work by Clayton et al. (2021, Appendix A) aimed to instead warp the flow field via a coordinate transformation to along/across-arc coordinates, similar to those used by Marghitu (2012), but we have found the solution used here to be both simpler to implement and faster in this context.

The plasma flow data from the virtual spacecraft provide the flow vectors $\mathbf{v}_i = (v_{xi}, v_{yi})$ at positions $\mathbf{r}_i = (x_i, y_i)$ with i being the sample number. These flow data are Gaussian smoothed, which is unavoidable, yet directly impacts the FAC sources in Equation 2.1, but more on this in Section 2.4.2. With this, the electric field components, E'_x and E'_y , to be compared against

the plasma flow data are

$$\begin{aligned} E'_x(\mathbf{r}_i; \bar{P}, \bar{A}) &= -\frac{\partial}{\partial x}\phi(\mathbf{r}; \bar{P}, \bar{A})\Big|_{\mathbf{r}_i} \\ &= -\sum_{k=1}^{N_k} \left[P_{k1} + \frac{2\gamma(\mathbf{r}_i; \bar{P}, \bar{A})}{P_{k4}^2} (P_{k1}x_i + P_{k2}) \frac{\partial b}{\partial x}\Big|_{x_i} \right] \\ &\quad \times \exp\left[-\frac{\gamma(\mathbf{r}_i; \bar{P}, \bar{A})^2}{P_{k4}^2}\right] \end{aligned} \quad (2.5)$$

$$\begin{aligned} E'_y(\mathbf{r}_i; \bar{P}, \bar{A}) &= -\frac{\partial}{\partial y}\phi(\mathbf{r}; \bar{P}, \bar{A})\Big|_{\mathbf{r}_i} \\ &= \sum_{k=1}^{N_k} \frac{2\gamma(\mathbf{r}_i; \bar{P}, \bar{A})}{P_{k4}^2} (P_{k1}x_i + P_{k2}) \exp\left[-\frac{\gamma(\mathbf{r}_i; \bar{P}, \bar{A})^2}{P_{k4}^2}\right], \end{aligned} \quad (2.6)$$

with $\gamma(\mathbf{r}; \bar{P}, \bar{A}) = y - P_{k3} - b(x; \bar{A})$ and

$$\frac{\partial b}{\partial x} = \sum_{j=1}^{N_j} \frac{A_{j2}}{A_{j4}} \operatorname{sech}^2\left(\frac{x - A_{j3}}{A_{j4}}\right). \quad (2.7)$$

From here, with $\mathbf{B} = -B\hat{z}$, we determine the plasma flow:

$$\mathbf{v}'(\mathbf{r}; \bar{P}, \bar{A}) = v'_x \hat{x} + v'_y \hat{y} = \frac{\mathbf{E}' \times \mathbf{B}}{B^2} = \frac{1}{B} (-E'_y \hat{x} + E'_x \hat{y}). \quad (2.8)$$

This reduces the problem to finding the parameter matrix, \bar{P}^0 , which solves

$$\min_{\bar{P}} \sum_i \| (v'_x(\mathbf{r}_i; \bar{P}, \bar{A}^0), v'_y(\mathbf{r}_i; \bar{P}, \bar{A}^0)) - (v_{xi}, v_{yi}) \|^2, \quad (2.9)$$

where \bar{A}^0 is the best fitting boundary parameter matrix, such that the continuous plasma flow map, v_c , is given by

$$\mathbf{v}_c(\mathbf{r}) = \mathbf{v}'(\mathbf{r}; \bar{P}^0, \bar{A}^0), \quad (2.10)$$

and subsequently the continuous potential map used to drive ionospheric models is

$$\phi_c(\mathbf{r}) = \phi(\mathbf{r}; \bar{P}^0, \bar{A}^0). \quad (2.11)$$

By using the potential ridges, we prioritize solutions for ϕ_c that have sheet-like morphologies following the visible arc, in contrast to methods based solely on flow observations (Kamide et al., 1981; Amm, 1997; Nicolls et al., 2014; Bristow et al., 2016). This maintains strong potential gradients normal to the arc boundary, as may be expected from basic current continuity considerations and observations of electric field variability near arcs (Marghitu, 2012).

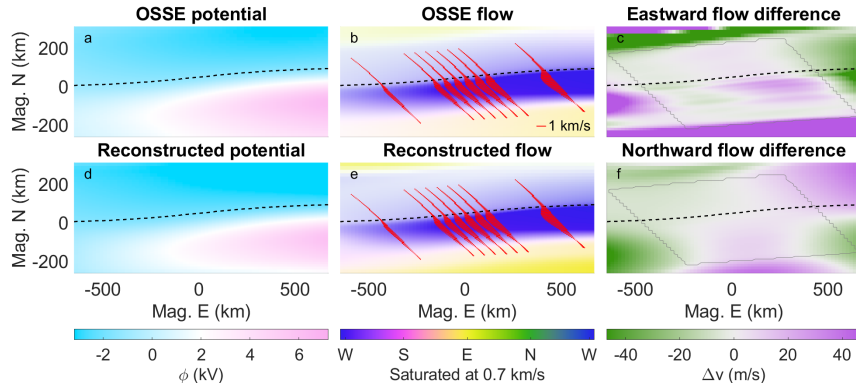


Figure 2.2: Example of a plasma flow field reconstruction. (a) The electric potential map used to drive the OSSE with the boundary, b , overlaid. (b) The resulting flow field with the virtual flow data points, \mathbf{v}_i , (red) interpolated from it. The color representation of flow has the direction depicted by hue and the intensity by the color saturation. (d – e) The reconstructed electric potential, ϕ_c , and flow, \mathbf{v}_c . (c, f) The difference between the reconstructed and OSSE east- and northward flow with the gray outline being the region of interest. Data source: <https://rcweb.dartmouth.edu/LynchK>.

Reconstruction Example

Figure 2.2 shows an example use of the reconstruction algorithm. This example was developed for the proposed ARCS mission (Lynch et al., 2024b) to verify the ability of plasma flow reconstruction given a local grouping of spacecraft. The virtual orbits are arranged densely to provide maps of along- and across-arc gradients. The black dashed lines are the imagery-derived boundary, b . The plasma flow vectors, \mathbf{v}_i , are overlaid in red. The reconstructed electric potential, ϕ_c , and reconstructed flow, \mathbf{v}_c , match well within the spacecraft region (gray outline in Figure 2.2c, f). The maximum absolute flow difference in this region is 50 m/s eastward and 30 m/s northward with averages of around 0 to 10 m/s.

2.2.2 Replication

The second method of developing continuous topside ionospheric plasma flow maps uses individual, approximately across-arc data tracks of plasma flow data in conjunction with all-sky, multi-spectral imagery. Here, data points are replicated in the along-arc direction using direct and indirect information from the imagery. Primary *and* secondary boundaries are determined along which the data track is translated, scaled, and the flow data

are rotated to be parallel with the primary boundary. The example here uses dataset “c5” from Clayton et al. (2021) on March 2, 2017 at 7:54:10 UT (20.2 MLT).

Arc Boundary Definitions

Determining the arc boundaries from multi-spectral imagery data first requires an inversion to a map of total energy flux, Q_p , and characteristic energy, E_p , of the precipitating electrons. There are several methods for doing this (Janhunen, 2001; Hecht et al., 2006; Dahlgren et al., 2011; Hecht et al., 2012), but we’ve opted for one based off of work done by Grubbs II et al. (2018b). From these maps, an estimate for the Pedersen conductance is made using Equation 3 by Robinson et al. (1987):

$$\Sigma_P(x, y) = \frac{40E_p(x, y)}{16 + E_p^2(x, y)} Q_p^{1/2}(x, y), \quad (2.12)$$

with E_p in keV and Q_p in mW/m². It is possible to use multi- and/or two-stream transport models (similar to how Q_p and E_p are determined), such as the GLobal airglOW (GLOW) model (Solomon, 2017), or look-up tables generated by such models, to determine a more accurate Pedersen conductance; however, Equation 2.12 suffices in providing a proof-of-concept.

The primary and secondary arc boundaries are established in one of two ways: (1) finding the magnetic latitude of the first two most prominent arc edges at each magnetic longitude using Sobel edge detection (Sobel, 2014) in the magnetic northward direction, or (2) following a contour line at two isovalues which can be chosen directly, or determined at the locations of the central two most prominent edges along the data track. In either case, the boundary is Gaussian smoothed. Both of these methods can be applied to the *either* the total energy flux *or* Pedersen conductance. Clayton et al. (2019, 2021) use method 1 on the total energy flux, whereas, for the remainder of this paper, we use boundaries determined using Pedersen conductance contour lines. Figure 2.3 shows the Pedersen conductance and its magnetic northward Sobel convolution along with the primary and secondary boundaries determined using method 2 with Pedersen conductance and method 1 with total energy flux. The choice of using conductance, over total precipitating energy flux or brightness, lies in the Ohmic relation between it and the electric fields and currents, making it more geophysically representative. Furthermore, the default choice for the primary boundary is the equatorward one, but the user can swap this choice.

Flow Data Replication

After the boundaries are determined, they are used to replicate the plasma flow data track, but first, the flow data are Gaussian smoothed (more on this

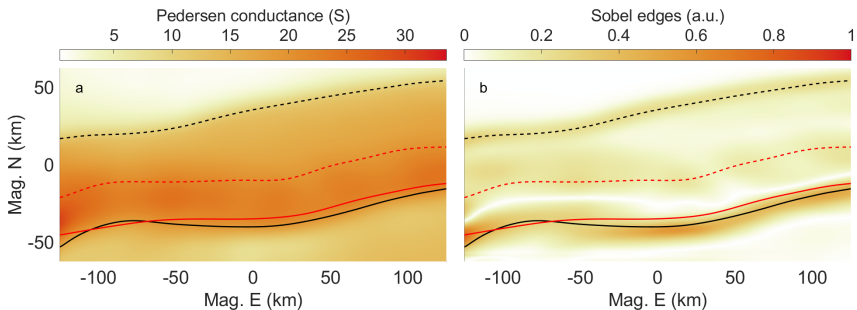


Figure 2.3: Primary (solid) and secondary (dashed) boundaries using Pedersen conductance and contour lines at 19.1 S and 10.5 S (black). In red are the boundaries determined using the energy flux (not shown) with the steepest gradient method, as is done by Clayton et al. (2019, 2021). (a) Pedersen conductance determined via Equation 2.12. (b) Magnetic northward Sobel convolution of the Pedersen conductance. Both sets of boundaries have an approximate smoothing window of 15 km.

in Section 2.4.2) and, prior to doing any replication, we split the plasma flow into two components: (1) the background flow, \mathbf{v}_{bg} , treated as a constant, global-scale disturbance, and (2) the arc-scale disturbances, \mathbf{v}_{arc} :

$$\mathbf{v}(\mathbf{r}) = \mathbf{v}_{\text{arc}}(\mathbf{r}) + \mathbf{v}_{\text{bg}}. \quad (2.13)$$

Throughout the remainder of Section 2.2, this background flow is subtracted and is only added back when performing 3-D simulations (see Section 2.3.2). In absence of background flow, the most basic model of an auroral arc is composed of only across-arc flow shear (Marghitu, 2012). Thus, we define the background flow such that, once removed, the arc flow at the intersection of the data track and the primary boundary is parallel to that boundary. Furthermore, this simplistic model has the arc defined as a band of enhanced conductance in which we expect the electric field to decrease (Marghitu, 2012; Kelley, 2009). Thus, we replicate these data along the arc boundaries, while remaining parallel to it, and scaling such that the shorted-out electric fields remain inside the area of enhanced conductance. This leads to the following plasma flow data track replication algorithm:

1. The original data track is translated in the east-north plane by some amount following the primary arc boundary such that the original and replicated flow data are equal at the primary boundary-track intersections.
2. The replicated data track is scaled in the along-track direction such

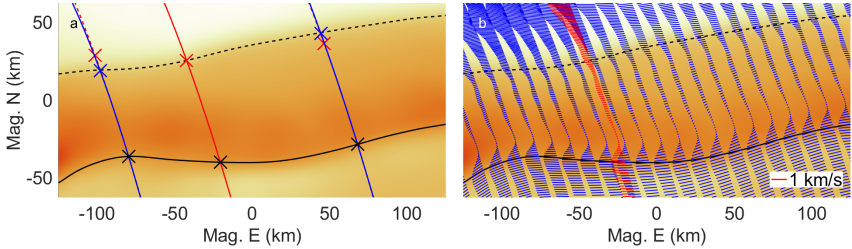


Figure 2.4: In situ trajectory flow data replication overlaid on the same conductance map from Figure 2.3a. (a) Two example replications (blue) of the original trajectory (red) along the primary arc boundary (solid black). The black crosses have the same flow data. The red/blue crosses indicate flow data before/after scaling to meet up with the secondary arc boundary (dashed black). (b) A low density replication (blue) along with the original, smoothed flow data (red). Data source: <https://rcweb.dartmouth.edu/LynchK>.

that the original and replicated flow data are equal at the secondary boundary-track intersections.

3. The flow data of the replicated track is rotated by a constant angle per data track such that it remains to be parallel to the primary arc boundary.
4. This replication is repeated for multiple translations along the arc until the top-boundary is filled with a sufficient replication rate.

Figure 2.4 illustrates these steps given the boundaries of Figure 2.3. The left panel of Figure 2.4 shows two examples of how replications of the original trajectory are translated and scaled. The western replication example is scaled down to have the data at the red cross meet the secondary boundary, while the eastern replication is scaled up to do the same. The right panel shows the replication done only for a few instances for illustration purposes. This also shows the rotated flow vectors keeping parallel with the primary boundary.

Enforcing Electrostatic Flow

The replication procedure does not, in general, produce a flow field that is divergence-free, implying a non-electrostatic component to the replicated field which we seek to remove for use in electrostatic models. The replicated flow data are first interpolated onto the model grid (more on this in Section 2.4.2). Next, as described in this section, there are two choices for fitting

an electric potential map to this interpolated flow field, $\mathbf{v}_{\text{arc}} = \mathbf{E}_{\text{arc}} \times \mathbf{B}/B^2$, where \mathbf{B} is the magnetic field from Equation 2.8 and \mathbf{E}_{arc} is the arc disturbed ionospheric electric field perpendicular to \mathbf{B} . The Helmholtz decomposition of the interpolated flow fields' associated electric field reads:

$$\mathbf{E}_{\text{arc}}(\mathbf{r}) = \mathbf{E}_I(\mathbf{r}) + \mathbf{E}_S(\mathbf{r}) = -\nabla\phi_c(\mathbf{r}) + \nabla \times \mathbf{A}(\mathbf{r}), \quad (2.14)$$

where ϕ_c is the electric potential map we are looking for and \mathbf{A} is the vector potential. We want to remove the non-electrostatic part, i.e. find the irrotational electric field, \mathbf{E}_I , and remove the solenoidal field, \mathbf{E}_S , in a way that best agrees with the interpolated flow field. Two choices of doing so are:

1. **Brute force:** Perform a least-squares fitting algorithm (Levenberg-Marquardt in our case) that fits a potential map, ϕ , to minimizes the residual between the original and irrotational fields:

$$\begin{aligned} \min_{\phi} \|\nabla \times \mathbf{A}(\mathbf{r})\|^2 &= \min_{\phi} \|\nabla\phi(\mathbf{r}) + \mathbf{E}_{\text{arc}}(\mathbf{r})\|^2 \\ &= \min_{\phi} \sum_{i,j} \left\| (\nabla\phi)_{ij} + \mathbf{E}_{\text{arc},ij} \right\|^2, \end{aligned} \quad (2.15)$$

the solution of which, ϕ_c , is the continuous potential map we want. While straightforward, this choice is computationally expensive.

2. **Fourier Representation Of Poisson's Equation (FROPE):** We take the divergence of Equation 2.14 to get Poisson's equation:

$$\nabla^2\phi_c(\mathbf{r}) = -\nabla \cdot \mathbf{E}_{\text{arc}}(\mathbf{r}). \quad (2.16)$$

We can solve for the particular solution using a Fourier representation:

$$-\|\mathbf{k}\|^2 \tilde{\phi}_c(\mathbf{k}) = -i\mathbf{k} \cdot \tilde{\mathbf{E}}_{\text{arc}}(\mathbf{k}) \implies \tilde{\phi}_c(\mathbf{k}) = i \frac{\mathbf{k} \cdot \tilde{\mathbf{E}}_{\text{arc}}(\mathbf{k})}{\|\mathbf{k}\|^2}, \quad (2.17)$$

where $\mathbf{k} = (k_x, k_y)$ is the wave vector, such that the particular potential solution map is

$$\phi_p(\mathbf{r}) = (\mathcal{F}^{-1}\tilde{\phi}_c)(\mathbf{r}), \quad (2.18)$$

where \mathcal{F}^{-1} denotes the inverse Fourier transform. The homogeneous solution, ϕ_h , where $\phi_c = \phi_p + \phi_h$ and $\nabla^2\phi_h = 0$, usually is determined using a Laplace solver enforcing the boundary conditions of \mathbf{E}_{arc} . However, in order to have more control over the weighting of the plasma flow generated by our replication and interpolation procedure, we opt for one of two options: the first, $\phi_h = \phi_a$, has the average electric field before and after enforcing electrostatics remain, i.e.

$$\phi_a(\mathbf{r}) = \langle -\nabla\phi_p(\mathbf{r}) - \mathbf{E}_{\text{arc}}(\mathbf{r}) \rangle \cdot \mathbf{r}. \quad (2.19)$$

This option requires no optimization (i.e. it can be computed directly from the particular solution found above), whereas a second option, $\phi_h = \phi_b^m$, solves the optimization problem

$$\min_{\bar{F}} \| -\nabla(\phi_p(\mathbf{r}) + \phi_b^m(\mathbf{r}; \bar{F})) - \mathbf{E}_{\text{arc}}(\mathbf{r}) \|^2 \quad \text{with } \mathbf{r} \in \mathcal{M}, \quad (2.20)$$

where \bar{F} is an $m \times 2$ parameter matrix and \mathcal{M} is a user defined masking domain surrounding the primary and/or secondary boundary, and original data track. This mask prioritizes locations closer to where the replication is assumed to be most true. This homogeneous solution, ϕ_b^m , is the most general polynomial of degree m in x and y that satisfies Laplace's equation (See Appendix A.1):

$$\begin{aligned} \phi_b^m(\mathbf{r}; \bar{F}, \rho) &= \sum_{n=1}^m \sum_{q=0}^{\lfloor n/2 \rfloor} (-1)^q \\ &\times \left[\frac{F_{n1}}{\rho^{n-1}} \binom{n}{2q+1} x^{2q+1} y^{n-2q-1} + \frac{F_{n2}}{\rho^{n-1}} \binom{n}{2q} x^{2q} y^{n-2q} \right], \end{aligned} \quad (2.21)$$

where ρ is a scaling parameter used to facilitate fitting higher order terms. An example for $m = 2$ and $\rho = 10$ m gives

$$\phi_b^2(\mathbf{r}; \bar{F}) = F_{11}x + F_{12}y + \frac{F_{21}}{10}(x^2 - y^2) + \frac{F_{22}}{10}xy. \quad (2.22)$$

Note that x , y , and ρ in meters and \bar{F} in V/m has ϕ_b^m in volts. When solving for this optimization problem the initial guess is taken to be ϕ_a .

Along with the replicated, interpolated flow field (column 1), examples of the brute force and FROPE electrostatic fields are shown in Figure 2.5 (columns 2 – 3). The divergence panel (Figure 2.5g) shows that of the interpolated flow field and indicates spurious effects from the replication and interpolation. Although the brute force method is easiest to justify being the “best” fit, it is also by far the slowest. The FROPE method, on the other hand, has the advantage of using the fast Fourier transform method and it compares reasonably well, even when using the direct harmonic solution, ϕ_a . This is illustrated in Figure 2.6 which shows the residual between the brute force solution and the potential from Equation 2.18 compared against a masked and unmasked harmonic fit. A constant background electric field match, i.e. a harmonic function that is a constant sloped plane, ϕ_a , is a first order solution in this particular case but this requires further confirmation for other cases. Figure 2.6c shows how the masking allows the user to loosen the constraints in regions where the replication is less trusted, such as in the corners and in areas far from the regions-of-interest.

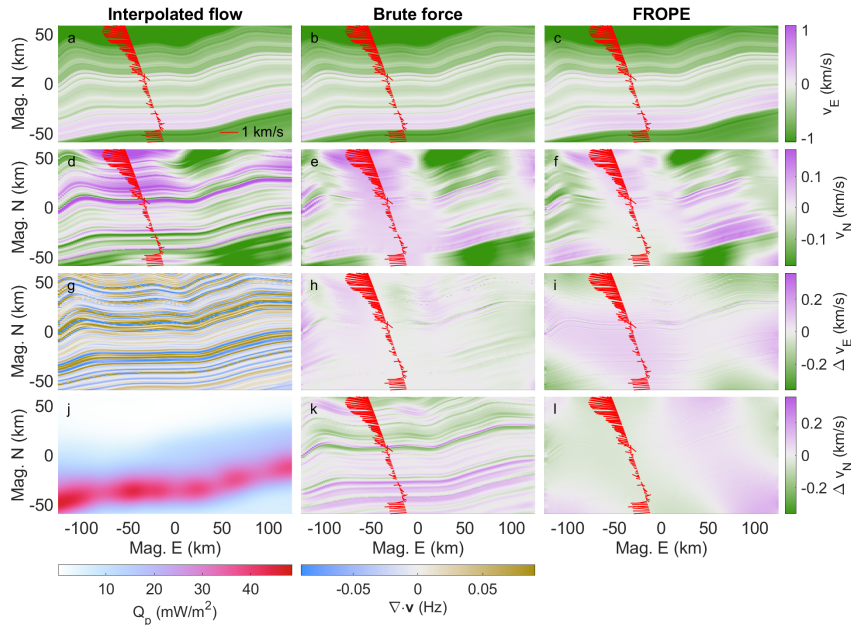


Figure 2.5: Comparison of methods for determining a potential map from an interpolated flow map, \mathbf{v}_{arc} . In red are the in situ plasma flow data which have no smoothing applied in an effort to stress test these methods. (a – c) Eastward plasma flow from interpolation, the brute force method, and the FROPE method. (d – f) Same as panels a – c but northward. (g) Divergence of the interpolated flow. (h, k) Difference in east- and northward flow between brute force and interpolated. (i, l) Difference in east- and northward flow between the FROPE and brute force. (j) Total precipitating energy flux (for reference). Data source: <https://rcweb.dartmouth.edu/LynchK>.

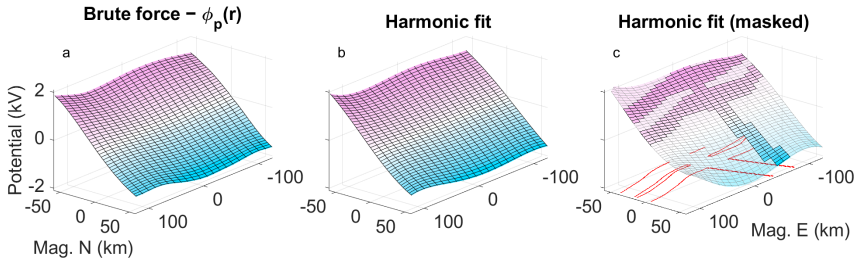


Figure 2.6: Validity of a harmonic function fit. (a) Residual potential between brute force fitting and Equation 2.18. (b) Unmasked harmonic function fit from Equation 2.21 with $m = 5$ and $\rho = 10$ m. (c) Same as panel b but masked with the mask, \mathcal{M} , in red.

Replication Example

Figure 2.7 shows the replication methodology applied to the “c5” example by Clayton et al. (2021, see their Table 1). The top row has the scaling and rotating applied, whereas the bottom row has neither applied, as is done in (Clayton et al., 2021). For the top row, the masked histogram 2-sigma ranges of the residuals in enforcing electrostatics are ± 110 m/s eastward and ± 140 m/s northward. For the bottom row, these numbers are ± 80 m/s and ± 100 m/s. Both histograms are centered close to 0 m/s. The higher residuals for the top row are attributed to having to fit electrostatic flow to a more complex interpolated flow map. Qualitatively, the applied scaling to the replication results in a co-location of the shorted-out electric field and the auroral precipitation as seen by the Σ_P contour lines in panel a, in comparison to panel d. Secondly, the applied rotation provides more streamlined plasma flow as seen by the change from southwest to west to southwest flow in panel a. In contrast, without rotation the flow remains westward resulting in a changing angle between the electric field and the conductance gradients. This has direct physical effects on auroral current closure, i.e. generation of FACs as per Equation 2.1.

2.2.3 Weighted Replications

For a conjunction between auroral imagery and *two* flow data tracks, the replication method can be repeated for both tracks up to and including the interpolation step (at the beginning of Section 2.2.2). Both replications use the same primary and secondary boundaries as well as the same background flow, \mathbf{v}_{bg} . This background flow is determined by whichever replication is done first. The flow data smoothing is also performed with approximately

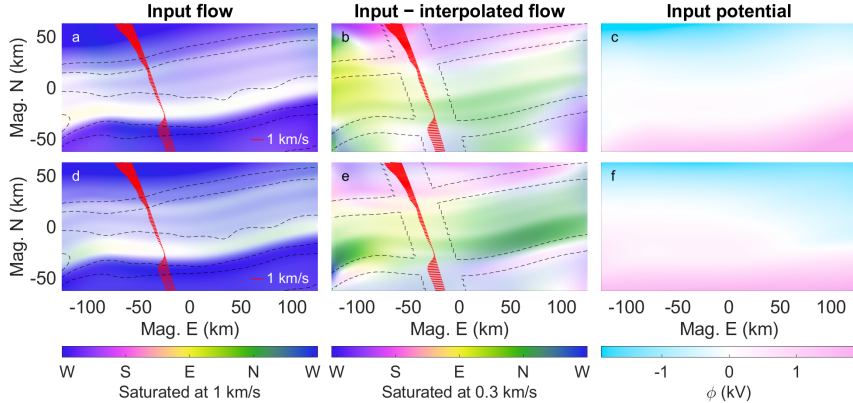


Figure 2.7: Input flow and potential maps used to drive simulations with (top row) and without (bottom row) replication scaling/rotating. (a, d) Hue-saturation plots of input flow maps, $-\nabla\phi_c$, with contour lines of Pedersen conductance, Σ_P . (b, e) Difference between input and interpolated plasma flow maps, i.e. $-\nabla\phi_c - \mathbf{v}_{arc}$, with masking contours where the harmonic function is fit. (c, f): Input potential maps, ϕ_c . Data source: <https://rcweb.dartmouth.edu/LynchK>.

equal Gaussian filter physical window widths.

Once both data tracks have their replicated, interpolated flow fields, the two fields are weighted averaged with the weighting functions

$$w_A(\mathbf{r}) = \frac{1}{2} \left[1 + \tanh \left(\frac{d_{min,B}(\mathbf{r}) - d_{min,A}(\mathbf{r})}{s_w} \right) \right], w_B(\mathbf{r}) = 1 - w_A(\mathbf{r}). \quad (2.23)$$

Here, $d_{min,A}$ is a map of the shortest straight-line distances from points \mathbf{r} to data track A and similarly for data track B . This configuration of weighting allows for two intersecting data tracks. The scale length, s_w , will introduce flow gradients and has to be chosen with care. From here we have a new interpolated arc-disturbed plasma flow,

$$\mathbf{v}_{arc}(\mathbf{r}) = w_A(\mathbf{r})\mathbf{v}_{arc,A}(\mathbf{r}) + w_B(\mathbf{r})\mathbf{v}_{arc,B}(\mathbf{r}), \quad (2.24)$$

from which the methodology from Section 2.2.2 takes over. This ensures electrostatics, but on top of the spurious divergences still remaining in either data track's replicated field, this weighting function introduces additional divergence of the form

$$(\nabla \cdot \mathbf{v}_{arc})_w = \nabla w_A(\mathbf{r}) \cdot (\mathbf{v}_{arc,A} - \mathbf{v}_{arc,B}). \quad (2.25)$$

This weighting function, however, has small northward gradients and the interpolated flows often do not vary much eastward, i.e. ∇w_A is approximately orthogonal to $\mathbf{v}_{\text{arc},A} - \mathbf{v}_{\text{arc},B}$ resulting in minimal diverging flow. This ensures that the subsequent Helmholtz decomposition provides an electrostatic solution of the final flow map that does not differ much from the interpolated replication.

Weighted Replication Example

To illustrate the double replication methodology, a conjunction from the *Swarm-over-Poker-2023* campaign is used (February – March 2023, Poker Flat Research Range, AK). This campaign facilitated conjunctions of, in part, ion flow data from the Thermal Ion Imagers (TII, Knudsen et al., 2017) on ESA’s Swarm mission, convection flow data from AMISR’s Poker Flat Incoherent Scatter Radar (PFISR, Kelly and Heinselman, 2009; Nicolls and Heinselman, 2007; Heinselman and Nicolls, 2008), and multi-spectral, all-sky imagery from the Poker Flat DASC (Conde et al., 2001). This season provides a rich source of heterogeneous auroral observations for the winter months of 2023. Our example uses data from March 19 at 8:23:44 UT (20.4 MLT).

The Swarm spacecraft include a horizontal and vertical TII which both provide a ram ion flow component, and separately provide the remaining two cross-track components. The quality flags for the version 0302 Swarm ram ion flow data (Burchill and Knudsen, 2022) are always set to 0 (use with caution), hence we consulted with the EFI team and received confirmation that the ram flow data for our events appear to be of sufficient quality for this application (pers. comm. J. K. Burchill, 2024). The data streams from both the horizontal and vertical TII are simultaneously fit using locally weighted scatterplot smoothing to both filter noise and suppress outliers. The calibration flags for all components only indicate *BNE* (baseline noise exceeding 100 m/s) for at most around 1% of the data.

Figure 2.8a summarizes this event showing an auroral arc peaking at $Q_p \approx 30 \text{ mW/m}^2$ (and $E_p \approx 7 \text{ keV}$, not shown) with minor along-arc structure. The left trajectory shows ion flow data from Swarm B and the right data track shows convection flow data from PFISR. Panel b also shows the Pedersen conductance (in this case inverted using GLOW (Solomon, 2017; Grubbs II et al., 2018b)) which is used to determine the arc boundaries, and panel c shows the weighting function used for the Swarm data (the PFISR weighting, not shown here, is one minus the Swarm weighting). The bottom row gives the final continuous plasma flow maps using only the Swarm data, or only the PFISR data, or both. The individual reconstructions in panels d and e are dissimilar which is to be expected given the along-arc structure; the flow data are different at the two locations surrounding the arc, as are

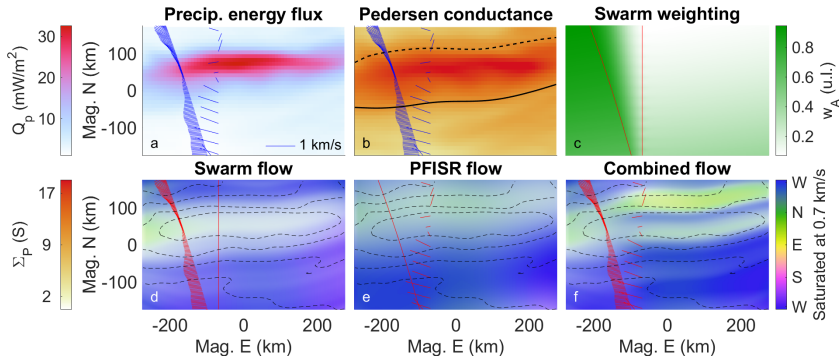


Figure 2.8: Weighted replication example. (a) Precipitating total electron energy flux with plasma flow data from Swarm (left trajectory) and PFISR (right data track) in blue. (b) The GLOW derived Pedersen conductance with the primary (solid) and secondary (dashed) boundaries overlaid. (c) The weighting map, w_A , used for the Swarm data with a scale length of $s_w = 200$ km. (d – f) Resulting flow maps from using only Swarm data, only PFISR data, and from using both datasets, respectively. The dashed contours are of Pedersen conductance. Data sources: <http://optics.gi.alaska.edu/optics> (DASC), <https://data.amisr.com/database> (PFISR), and <https://swarm-diss.eo.esa.int> (Swarm).

the conductance gradients. The final combined flow (panel f) before and after enforcing electrostatics have residual 2-sigma standard ranges of ± 90 m/s eastward and ± 160 m/s northward.

Note that the combined flow, panel f of Figure 2.8, is not merely a weighted average of panels d and e. This is because the weighted average is applied to the interpolated maps, after which the electrostatic enforcing is performed which relies on a multitude of parameters. This is something to keep in mind when applying these techniques.

2.3 Auroral Ionosphere 3-D Modeling with Potential Map Estimates

2.3.1 The GEMINI model

To investigate the effects of continuous topside ionospheric plasma flow maps in conjunction with auroral precipitation, we use state-of-the-art 3-D ionospheric simulations provided by the Geospace Environment Model of Ion-Neutral Interactions (GEMINI, Zettergren and Semeter, 2012; Zettergren and Snively, 2019). This is a multi-fluid (6 ions + electrons), quasi-

electrostatic model with its calculations of particle continuity consisting of chemical production/loss and photo/impact ionization. Calculations of local densities, plasma flows, and temperatures are treated self-consistently and the model includes thermal conduction heat flux, collisional heating, thermoelectric electron heat flux, and inelastic cooling/heating from photo-electrons. This is supplemented with Maxwell's equations and, at the time of writing, includes no displacement current or magnetic induction effects. With this, the system is solved through enforcing divergence-free currents, curl-free electric fields, and invoking Ohm's law. The model can be forced with a top-boundary potential map which is copied to all altitudes, or with a top-boundary map of FAC where the remaining boundaries are set to zero. A full description of governing equations solved by GEMINI is given in Appendix A of Zettergren and Snively (2015).

2.3.2 Simulation Examples

Figure 2.9 shows GEMINI output data with Figure 2.7c as the plasma flow driver and the same precipitation data used by example “c5” from Clayton et al. (2021). Unlike previous figures, here the figure/simulation includes \mathbf{v}_{bg} . This simulation has $440 \times 504 \times 814$ nonuniform cells in the magnetic east, north, and anti-parallel directions and runs for 90 seconds. The calculated FAC slice is taken at an altitude of 200 km, but is plotted at 80 km for visualization purposes. Similarly, the electron density slice is taken at the center but plotted at the eastern wall. In order to visualize FAC closure, we opt for current flux tubes which are made possible by (a) the GEMINI enforced condition of $\nabla \cdot \mathbf{j} = 0$, and (b) the use of streamlines sourced at closed elliptical curves (solid black curves). This enables an improved interpretation of auroral current closure by showing where a patch of FAC joins back with the magnetosphere, or where a region of Hall current exits the model space. These flux tubes are analogous to electrical wires in that they carry a single amperage. The dotted black and blue curves show the projection of the terminating ends of the flux tubes onto the FAC map. The green flux tube (27.8 kA) represents a traditional example of FAC closure via the Pedersen layer, closing down between 118 - 159 km. The orange tube (31.0 kA) runs underneath it near the Hall layer and shows exchange between a region of Hall current and Pedersen current (see magenta electric field vectors) up near the bottom of the Pedersen layer. This tube enters at the poleward wall between 90 - 110 km in altitude, spans between 87 - 100 km at its lowest point, and exits the equatorward wall between 101 - 126 km. The red flux tube (23.9 kA) is, to some extent, a combination of these two, and has two exit regions. When this tube runs out of upward FAC to close through in its adjacent current sheet, it continues onto the next upward FAC sheet poleward of it where the

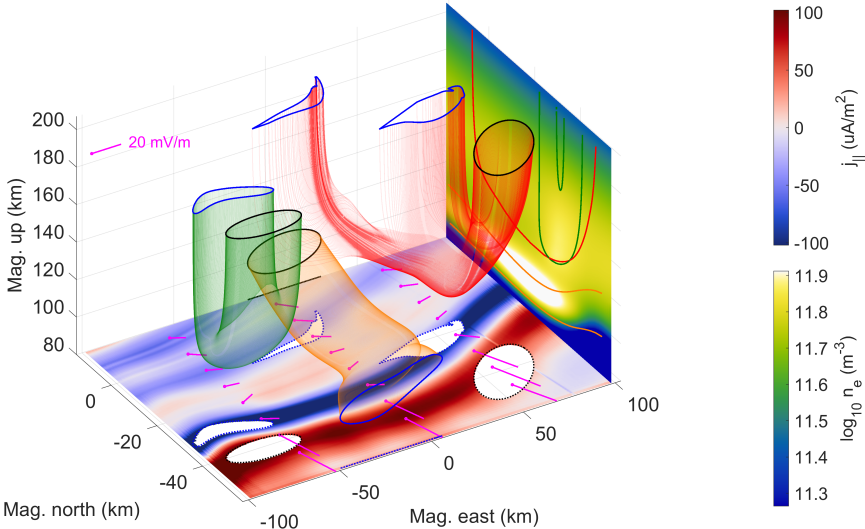


Figure 2.9: Plasma flow driven GEMINI output with input from the potential in Figure 2.7c. Current flux tubes are colored for distinction purposes and start/end at solid black/blue curves. The orange flux tube runs in reverse from the poleward to the equatorward boundary walls. (Eastern boundary) A north-up slice of electron density taken at 0 km east along with flux tube outline projections. (Bottom boundary) An east-north slice of FAC (with parallel being down) taken at 200 km altitude along with flux tube start/end curve projections (dashed) and electric field vectors (magenta). These electric field vectors include the background electric field.

remaining 2.5 kA is closed.

To show the effects of steps 2 and 3 of section 2.2.2 we run additional simulations (at a lower resolution of $128 \times 512 \times 212$) using the same precipitation maps but with the replication scaling and rotating turned on and off (see Figure 2.7, panels d – f). Figure 2.10 divides the topside ionospheric FAC maps of both simulations into the three terms from Equation 2.1 in order to look at the effects of the plasma flow shear and precipitation gradients separately. Panels 2.10a – c (replicated with scaling and rotating) show good alignment at both arc boundaries for all three FAC terms. In contrast, panels 2.10d – f (replicated without scaling or rotating) show that, at the poleward boundary, the FAC structure does not follow the contour of the arc; the directions of \mathbf{E} , $\mathbf{E} \times \mathbf{B}$, and the conductance gradients are not simultaneously considered in constructing the driver of this simulation.

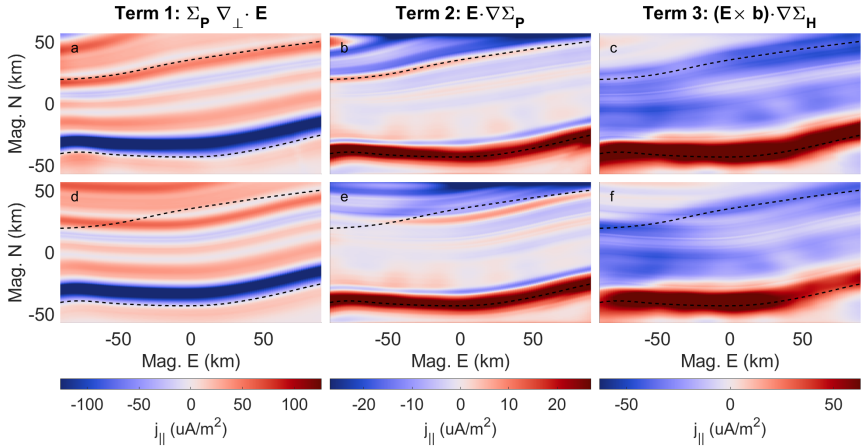


Figure 2.10: Calculated FAC components from Equation 2.1. (a – c): Terms 1 through 3 respectively split from the FAC map shown in Figure 2.9 along with arc boundaries (dashed). (d – f) Same as terms from the top row but with replication scaling and rotating turned off.

2.4 Discussions

2.4.1 Improvements to Auroral Plasma Flow Mapping

Figure 2.9 indicates that, even for basic examples of auroral arc systems, the morphology of current closure is 3-D in nature. The green flux tube depicts a simpler auroral current closure type (Mallinckrodt, 1985) using largely Pedersen currents to close. The red flux tube illustrates a less common view of FAC closure where not all current from one FAC sheet has to close with its neighbouring sheet. The section of the sourced FAC furthest equatorward has to “dig” deeper into the Hall layer, subsequently horizontally rotating, in search of another closure path. The reason why the tube splits, and does not simply enlarge one of its exit regions, is because the neighbouring regions of FAC are occupied by other flux tubes not shown. The orange flux tube is mostly Hall current, but includes divergence, i.e. the last term in Equation 2.1, which is being fed by Pedersen currents as the tube descends from regions of higher conductivity (see the electron density panel). The Pedersen current being used by this closure can no longer be used to close FACs, which is how diverging Hall currents can indirectly effect topside ionospheric currents. Moreover, FAC closure is not restricted to the 90 - 130 km altitude range where Pedersen and Hall conductivities maximize; depending on the perpendicular distance from the FAC sheet inflection line, Pedersen closure can happen at altitudes as high as 159 km

in this instance. From a current flux conservation standpoint, this is a matter of balancing the lower conductivity at these heights with a larger flux tube cross-section.

This 3-D structure is attributable to the interplay between the altitude dependent Pedersen and Hall conductivities as a region of current follows the path of least resistance. To better understand electrostatic auroral arc scale science, and the non-passive role the ionosphere plays in quasi-static MI coupling, these 3-D features require further studies, which in turn requires 3-D auroral simulations and thus this creates the need for continuous, topside ionospheric, electrostatic plasma convection maps.

We have developed techniques for creating such maps from sparse, heterogeneous, and distributed measurements which focus on the anisotropic physical scales and gradient scale lengths of aurorae, and discrete sheet-like morphologies. The reconstruction, replication, and weighted replication methodologies all use maximal information from imagery derived precipitation maps to provide geophysically meaningful extrapolations of plasma flow maps surrounding auroral arcs. This is achieved by the following extensions to work done by Clayton et al. (2019):

1. Opting for imagery derived Pedersen conductance contour lines, in place of energy flux gradients, as a more natural choice for replicating electric field data.
2. Using a secondary auroral arc boundary to which the plasma flow data are scaled in an attempt to co-locate shorted-out electric fields with enhanced precipitation.
3. Rotating replicated plasma flow data to ensure the arc-flow related disturbance remains parallel to auroral arcs.
4. Using the Fourier Representation Of Poisson's Equation technique in enforcing electrostatics, enabling large numbers of simulations to be developed.

Figures 2.7 and 2.10 demonstrate these improvements. These additional measures ensure that the relative directions between the electric fields and the imagery related gradients are more geophysical, and they represent the next step toward studying auroral arcs that stray from ideal, sheet-like morphologies.

2.4.2 Cautionary Remarks

The Gaussian smoothing of the plasma flow data (referred to in Section 2.2.2) cannot be avoided, but does require careful thought. Replications need to accommodate similar resolutions in both flow and conductance. If

this is not done there is a possibility that one will end up with FACs that are purely an artifact of mismatched gradient scale lengths in estimated flow and precipitation maps. Figure 2.8 shows a well-matched example where the precipitation and conductance map each have similar minimal structure sizes to that of the resulting plasma flow maps. If available, the simulated FAC can, of course, be compared against in situ current data for validation.

As a further cautionary reminder, the replicated plasma flow interpolation (see Section 2.2.2) needs to be done using cubic or cubic spline methods to ensure continuous derivatives. Using linear interpolation results in strong rippling of simulated FAC because of discontinuous first derivatives in the electric field.

2.5 Conclusions & Applications

Measurements of auroral arc systems can be sparse, heterogeneous, and widely distributed, while ionospheric models generally require continuous top-boundary drivers. We address this challenge by using extensive information from multi-spectral, all-sky imagery. We have outlined three empirical methods for creating electrostatic, spatially continuous, topside ionospheric convection boundary conditions that focus on typical sheet-like discrete auroral arc structures. The main takeaways are as follows:

1. Even for the most basic auroral arc systems, a 1-D or 2-D description can be insufficient and may hide the 3-D nature of current closure.
2. When extrapolating ionospheric topside plasma flow data surrounding auroral arcs, it is important to scale the data in a way that co-locates the associated shorted-out electric fields with the region of enhanced conductance.
3. Similarly, it is important to rotate the plasma flow data in a way that avoids introducing arbitrary angles between the ionospheric electric field and the conductance gradients.
4. Current flux tubes whose ends are near the FAC inflection line between an upward and downward current sheet can close through Pedersen current at altitudes well above where Pedersen conductivity maximizes.
5. Current flux tubes surrounding auroral arcs can split; a region of FAC inside one downward current sheet can close in two upward current sheets.

It is possible to merge the techniques described in this paper with Lompe (Laundal et al., 2022). This can be done directly by using replicated flow maps (with appropriate weighting) and FAC data as input to Lompe. Another way is by adding constraints to Lompe that prioritize solutions with small angles between conductance gradients and flow, and solutions with small products between electric field and conductances to act as step 2 and 3 in Section 2.2.2.

Finding a set of electrostatic auroral conductances, convection flow, and FAC maps that are physical and self-consistent can be fully determined through current continuity. Finding a set that appears in nature, on Earth, and is likely, however, requires a greater understanding of the three-dimensional interplay between these three ingredients. The techniques outlined in this paper can be used to develop a series of data-driven 3-D simulations provided by conjunctions like those from the Swarm-over-Poker-2023 campaign. Conjunctions which include convection flow data provided by EISCAT 3-D (Stamm et al., 2021) can also be used in the future using these techniques. Such simulations can be idealized to retain only the fundamental auroral structures (peak precipitation flux, flow shear, arc width, etc.) where the resulting data-*inspired* simulations can be defined by a manageable number of parameters. This parameter space can be strategically explored, gradually straying auroral systems from ideal, sheet-like structure. Understanding the physical mechanisms connecting these various parameters will enable more quantitative understanding of what the visible aurorae indicates about its coupled environment.

Open Research

All 3-D simulation data, Isinglass data, imagery inversions, and reconstruction/replication tools (van Irsel, 2024) are available at <https://rcweb.dartmouth.edu/LynchK>. The data for the Poker Flat DASC are available at <http://optics.gi.alaska.edu/optics/archive>, for AMISR at <https://data.amisr.com/database>, and for the Swarm TII at <https://swarm-diss.eo.esa.int>. The GEMINI source code and documentation is available at <https://github.com/gemini3d>.

Acknowledgments

We thank NASA for funding Jules van Irsel from grant 80NSSC23K1622 through the FINESST program and Dartmouth College for providing internal funding for Phase A of the Auroral Reconstruction CubeSwarm proposal from which a lot of this research stems, and we acknowledge NASA grant 80GSFC21C0009 for the ARCS MIDEX CSR funding. We are grateful for the data providers from the Isinglass rocket team and we acknowledge Isinglass LCAS support from NASA grant NNX14AH07G. The Poker Flat Incoherent Scatter Radar and Digital All-Sky Camera are operated by the SRI International for the National Science Foundation as part of the AMISR program through cooperative agreement AGS-1840962. This work uses version 0302, level 1B data from the Thermal Ion Imagers made possible by the European Space Agency’s Swarm Data, Innovation, and Science Cluster. We thank NASA for providing funding for the GEMINI model development from grant 80NSSC24K0126. 3-D simulations supporting this work were facilitated by the Discovery cluster at Dartmouth Research Computing and the NASA High-End Computing (HEC) Program through the NASA Advanced Supercomputing (NAS) Division at Ames Research Center. We thank Michael Hirsch, Terry Kovacs, and John Griffin for GEMINI and computational technical support. We also thank Meghan Burleigh for her invaluable input in reviewing this manuscript, and Leslie Lamarche and Hayley Clevenger for insightful discussions. Lastly we thank Don Hampton and Leslie Lamarche, along with NSF grant 2329979, for providing support for the Swarm-over-Poker-2023 campaign.

Chapter 3

Current Closure and Joule Heating in Data-Driven 3-D Auroral Arc Simulations

J. van Irsel¹, K. A. Lynch¹, A. Mule¹, M. D. Zettergren², J. K. Burchill³, L. J. Lamarche⁴, D. L. Hampton⁵

¹Dept. of Physics and Astronomy, Dartmouth College, Hanover, NH; ²Physical Sciences Dept., Embry-Riddle Aeronautical University, Daytona Beach, FL; ³Dept. of Physics and Astronomy, University of Calgary, Calgary, AB; ⁴SRI International, Menlo Park, CA; ⁵Geophysical Institute, University of Alaska Fairbanks, Fairbanks, AK

This chapter is adapted almost verbatim, with minor formatting and stylistic modifications, from a manuscript under the same title (van Irsel et al., 2025) which is under review and submitted to the Journal of Geophysical Research: Space Physics (#2025JA034311). The majority of contributions to this manuscript are by J. van Irsel. Contributions from coauthors include, in large part, review and editing. Specific contributions are mentoring, science guidance, supervision, and funding acquisition by K. A. Lynch, Section 3.2.1 by A. Mule, modeling and software support by M. D. Zettergren, and resources, data curation, and validation by J. K. Burchill, L. J. Lamarche, and D. L. Hampton.

Key Points:

- Understanding current closure in discrete auroral arc systems requires data-driven, three-dimensional ionospheric simulations
- Large-scale convection fields play a significant role in determining auroral arc current closure morphology and associated Joule heating
- Details of precipitating electron energy distributions can significantly affect current closure and Joule heating in auroral arc systems

Abstract

Discrete auroral arcs, despite many symmetries, are three-dimensional in nature, encapsulating latitude and longitude variations in precipitation and field-aligned currents combined with important altitude variations in conductivities, hence closure currents. This study presents data-driven, 3-D numerical simulations of these processes based on a coordinated campaign of heterogeneous measurements collected from the Poker Flat Research Range during a sequence of Swarm spacecraft overpasses. These measurements include field-aligned current, global-scale convection flow, and auroral emissions, which are used to create top-boundary drivers for auroral arc simulations. Six conjunctions between the spacecraft, all-sky imagers, and radars are investigated and their measurements are used to simulate auroral arcs through multiple iterations per conjunction event. We look at different estimates of the background convection flow, assumptions about the energy distributions of electron precipitation, and along-arc structures in field-aligned current, and see what effect they have on current closure and Joule heating in auroral arc systems. Across the six conjunction events, 11 comparisons of auroral arc systems are presented, covering a catalog of 17 simulations in total. These comparisons allow us to look at the sensitivity of auroral arc systems to input parameters and envelop the simulations in a qualitative confidence interval. Our results suggest that discrete aurorae should be studied in three dimensions to fully understand field-aligned current closure and, by extension, Magnetosphere-Ionosphere-Thermosphere coupling. Additionally, our results demonstrate that both large-scale convection flows and specifics about the energy distributions of auroral precipitation can significantly affect current closure and Joule heating in auroral arc systems.

Plain Language Summary

The aurorae, or northern and southern lights, are embedded within a system of interacting electric and magnetic fields, and charged particles, the more energetic of which produce the lights themselves by exciting the neutral atmosphere. This brings about a three-dimensional current system and resistive heating, known as Joule heating. These currents enter and exit the atmosphere along the Earth's magnetic field, and can only close their circuit between altitudes of 80 – 150 km, where the current carriers collide with the atmosphere. This paper outlines the importance of simulating aurorae in three-dimensions, and looks at how sensitive these simulations are to various input choices by observing the resulting differences in current connectivity and Joule heating. We look at collections of measurements from six different events and simulate them multiple times with different combinations covering 17 simulations in total. This allows us to gain insight into how much confidence can be had in our auroral arc simulations, and, by extension, what aspects are important to get right when studying auroral arcs. We conclude that large-scale plasma motion and the distribution of energies of the light-producing electrons both significantly affect the auroral system, and that current connectivity should be studied in three dimensions.

3.1 Introduction

Laws governing the physics of auroral arc systems are intrinsically three-dimensional—the conservation of mass, momentum, and energy density, in conjunction with Maxwell’s equations, outline a system whose across-arc, along-arc, and field aligned directions are coupled. In the last decade or two, interest in three-dimensional (3-D) studies of the auroral ionosphere has slowly picked up (Amm et al., 2008; Fujii et al., 2011, 2012; Marghitu, 2012; Zettergren and Snively, 2019; Clayton et al., 2019, 2021; Lynch et al., 2022; Yano and Ebihara, 2021; van Irsel et al., 2024), and we continue this trend by investigating quiet, discrete auroral forms in 3-D. Specifically, this paper looks at how electric current closure and Joule heating are affected by global-scale electric fields, the energy distributions of precipitating electrons, and along-arc structure in field-aligned currents (FAC), to provide insight into the geophysical domain of auroral arc systems.

The conductivity of the ionospheric volume surround auroral arcs is highly sensitive to impact ionization from electron precipitation (Fang et al., 2008, 2010). This ionization increases with increased energy flux, varies horizontally depending on arc structure, and varies in altitude depending on the energy distribution of the precipitation. Furthermore, the overarching, large-scale convection electric field guides the current continuity solution and directly affects the Joule heating of the system. For these reasons, to better understand auroral arc system currents, it is crucial that such systems are studied in 3-D.

Auroral-arc-scale science plays an important role in the interpretation of magnetosphere-ionosphere (MI) coupling. The ionospheric end plays a non-passive role in this coupling (Marghitu, 2012, & references therein) and is involved in an ongoing sequence of system science studies (Wolf, 1975; Seyler, 1990; Cowley, 2000; Lotko, 2004; Fujii et al., 2011, 2012; Marghitu, 2012; Khazanov et al., 2018; Clayton et al., 2019, 2021; Yano and Ebihara, 2021; Lynch et al., 2022; Enengl et al., 2023; Wang et al., 2024; van Irsel et al., 2024). Such MI studies require *F*-region ionospheric maps of FAC and electric potential to be consistent with a 3-D ionospheric conductivity volume created by sunlight and charged-particle, auroral precipitation. However, what is often looked at is the two-dimensional (2-D) perspective of auroral arc systems, whether that is north-up or east-north. In this case of the horizontal ($\perp \mathbf{B}$) perspective, high-latitude electrostatic coupling assumes the height-integrated relation between quasi-static electric field, FAC, and conductances given by Kelley (2009, Equation 8.15):

$$j_{\parallel}(x, y) = \Sigma_P \nabla_{\perp} \cdot \mathbf{E} + \mathbf{E} \cdot \nabla_{\perp} \Sigma_P + (\mathbf{b} \times \mathbf{E}) \cdot \nabla_{\perp} \Sigma_H, \quad (3.1)$$

where (x, y) is the plane orthogonal to the local magnetic field, j_{\parallel} is the ionospheric topside FAC, $\Sigma_{P,H}$ are the height-integrated Pedersen and Hall

conductivities, i.e. conductances, \mathbf{E} is the ionospheric electric field, and $\mathbf{b} = \mathbf{B}/B$ is the magnetic field direction. Yano and Ebihara (2021) (as well as Marghitu, 2012; Fujii et al., 2012, among others,) however, have pointed out that integrating out altitudinal effects can hide significant information regarding polar ionospheric systems, especially in terms of current closure. They use simplified 3-D Hall-magnetohydrodynamic simulations, taking into account ion-neutral collisions, to show that 2-D FAC closure assumed by the thin-layer approximation of the ionosphere is fundamentally different from the 3-D description, if alone for the fact that current streamlines can pass underneath one another.

The electric field solution from Equation 3.1 can be separated it into a constant, large-scale electric field, $\bar{\mathbf{E}}$, and a perturbation field, $\delta\mathbf{E}$, which gives two FAC contributions: $j_{\parallel} = \bar{j}_{\parallel} + \delta j_{\parallel}$ where

$$\bar{j}_{\parallel}(x, y) = \bar{\mathbf{E}} \cdot \nabla_{\perp} \Sigma_P + (\mathbf{b} \times \bar{\mathbf{E}}) \cdot \nabla_{\perp} \Sigma_H, \quad (3.2)$$

and

$$\delta j_{\parallel}(x, y) = \Sigma_P \nabla_{\perp} \cdot \delta\mathbf{E} + \delta\mathbf{E} \cdot \nabla_{\perp} \Sigma_P + (\mathbf{b} \times \delta\mathbf{E}) \cdot \nabla_{\perp} \Sigma_H. \quad (3.3)$$

After calculating and height-integrating the conductivities at a particular point in time, one can subtract \bar{j}_{\parallel} from a specified *F*-region map of FAC, j_{\parallel} , with which $\delta\mathbf{E}$ can be determined, i.e. solving current continuity and ionospheric Ohm's law with source term $\delta j_{\parallel} = j_{\parallel} - \bar{j}_{\parallel}$. In this sense, the electrostatic drivers are j_{\parallel} and $\bar{\mathbf{E}}$, and the ionosphere responds by introducing polarization fields to provide the remaining FAC. In other words, $\delta\mathbf{E}$ is a result from local polarization charge densities within the ionospheric volume, while $\bar{\mathbf{E}}$ is an electric field external to our auroral-arc-scale system. With this perspective, a constant global estimate of the background flow, $\bar{\mathbf{v}} = \bar{\mathbf{E}} \times \mathbf{b}/B$, from either SuperDARN or PFISR, is an additional current driver and thus should be accounted for when interpreting FAC observations. Both Equation 3.1 and topics discussed in this paper deal with self-consistency, not causal relationships, when finding solutions to auroral current continuity.

Marghitu (2012) reviews sequentially more complex descriptions of auroral arcs, the first of which takes on a band of enhanced uniform conductance with negligible altitudinal thickness and polarization electric fields that are fully in the across-arc direction. Having no along-arc gradients whatsoever results in FAC closure which relies only on Pedersen currents (see Equation 3.1), while the electrojet current flows underneath, but plays no part in FAC closure. The second description introduces an along-arc component in the electric field which can greatly enhance the auroral electrojet current by means of the Cowling effect (Cowling, 1932). With a partial Cowling channel (one with some FAC blockage), Amm et al. (2008) point out that

this requires taking into account the ionospheric thickness when looking at current continuity. This is because, as Yano and Ebihara (2021) have also pointed out, divergence-free currents cannot flow through one another. Amm et al. (2011); Fujii et al. (2011, 2012) therefore take on a finite length Cowling channel model, which includes a thin Pedersen layer on top of a thin Hall layer, allowing for primary and secondary Pedersen and Hall currents to connect. The third description by Marghitu (2012) only ignores the along-arc variation in the electric field, but does take on gradients of conductance along the arc. To understand FAC closure with this description, Marghitu (2012) uses 2-D (east-north) modeling given the non-linear nature of this problem. Marghitu (2012) concludes, however, that, even though various one- or two-dimensional descriptions of auroral arcs capture a substantial interpretation, a complete 3-D description is necessary to fully understand, even sheet-like, auroral arc systems.

This paper builds from work done by Clayton et al. (2021), who study auroral arc systems and, to do so, developed new methods for driving simulations with 2-D maps of auroral data to study the surrounding ionosphere in 3-D. Similar to the work presented in this paper, they use multi-spectral auroral imagery from the Poker Flat DASC to both (a) infer the electron precipitation energetics and (b) replicate one-dimensional, in situ measurements of plasma flow, creating continuous 2-D driver maps. Their plasma flow measurements are provided by the Isinglass sounding rocket campaign and the replication methods are described by Clayton et al. (2019). In this paper, we use replication methods by van Irsel et al. (2024), which expand upon these ideas, yet altered slightly in order to use in situ FAC data from orbital spacecraft (Swarm) instead of plasma flow data. With these tools, and given an abundance of observational datasets from the winter months of 2023, we explore the dependencies of current closure paths and Joule heating in auroral arc systems to different values of $\bar{\mathbf{E}}$, forms of electron precipitation spectra, and top-boundary FAC structures.

In this paper, we aim to determine geophysical, self-consistent solutions to ionospheric current continuity in non-ideal discrete auroral arcs that possess structure in across-arc, along-arc, and field aligned directions. In doing so, we explore how to properly drive 3-D simulations of auroral arc systems using 2-D electrostatic, continuous top-boundary conditions from distributed, multi-platform datasets: all-sky, multi-spectral imagery, in situ FAC data, and radar-based background convection flow data. Additionally, we study the sensitivity of current continuity solutions to various driver parameters, particularly background convection flow and precipitation parameters, in order to envelop auroral arc simulations in a form of qualitative confidence estimates. This provides a better understanding of the dominant physics behind auroral current closure and Joule heating for different situations. Ancillary to this, this study provides a catalog of auro-

ral arc simulations covering six conjunction events with multiple modeling iterations per event, as well as driver and visualization tools to facilitate future studies of auroral arc systems.

In Section 3.2 we outline the instrumentation used in this work, a brief description of the ionospheric model used to produce our simulations, along with methods for imagery inversion, the replication technique, the implementation of precipitating electron impact ionization, and our use of flux tubes for 3-D visualization of current closure. Section 3.3 summarizes the 6 conjunction events and Section 3.4 covers the simulation results and comparisons thereof. We conclude our findings and discuss possible improvements and future uses of our work in Section 3.5. A.2 covers the derivation of the differential hemispherical number flux of accelerated Maxwellian precipitation, and figures of simulations not included in this paper are in the Supporting Information (Appendix C), along with other supporting figures and descriptions.

3.2 Observational Data, Instrumentation, & Methodologies

The data products we use are of six conjunction events that are part of the *Swarm-over-Poker-2023* campaign. This campaign facilitated simultaneous observations in February – March, 2023, of a variety of auroral arcs during times when the European Space Agency’s (ESA) Swarm spacecraft orbited overhead of the Poker Flat Research Range in Alaska. These observations are of key ionospheric electromagnetic parameters including, but not limited to, (1) the ESA Swarm mission’s ion flow data from the Thermal Ion Imagers (Knudsen et al., 2017, TII,) and (2) FAC data derived from its magnetometers (Ritter et al., 2013), (3) convection flow data from AMISR’s Poker Flat Incoherent Scatter Radar (Kelly and Heinselman, 2009; Nicolls and Heinselman, 2007; Heinselman and Nicolls, 2008, PFISR,), (4) global convection flow maps from the Super Dual Auroral Radar Network (Greenwald et al., 1995, SuperDARN,), and (5) multi-spectral, all-sky imagery from the Poker Flat Digital All-Sky Camera (Conde et al., 2001, DASC,). Figure 3.1 shows the geographical context of the February 10, 2023 conjunction event. In this section we cover the details surrounding these data products and any methodologies applied to them, as well as the model used to create our auroral arc simulations.

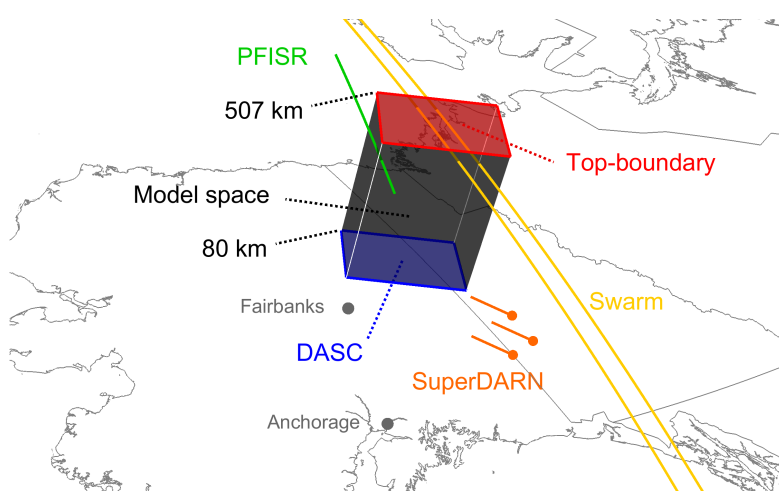


Figure 3.1: Geographical context of our simulations, using the February 10, 2023 conjunction as an example, showing the model space (black), the Swarm A and C crossings (yellow), the PFISR track (green), the top-boundary for the driver maps (red), the approximate location of the imagery from below (blue), and a symbolic depiction of some flow vectors from the SuperDARN global data map (orange) on top of Alaska.

3.2.1 Poker Flat Digital All-Sky Cameras & Imagery Inversion

The all-sky, multi-spectral auroral imagery we use comes from the University of Alaska Fairbanks Geophysical Institute's Poker Flat Digital All-Sky Cameras (Conde et al., 2001, DASC,) located at 212.57° east and 65.12° north (geographic). From this imagery we use a Python-based routine and the GLobal airglOW model (Solomon, 2017, GLOW,) to produce estimated maps of both total precipitating energy flux, Q_p , and expected energy, $\langle E \rangle$. In this work, the expected energy is either the characteristic energy, E_0 , or acceleration potential, U_a (see Section 3.2.7).

As shown by Rees and Luckey (1974), and later expanded on by several others (Strickland et al., 1989; Janhunen, 2001; Hecht et al., 2006; Grubbs II et al., 2018a,b), the ratio of green line (558 nm) to red line (630 nm) intensity for emissions driven by electron precipitation mostly depends on $\langle E \rangle$, while the blue line (428 nm) intensity mostly depends on Q_p . Roughly following Grubbs II et al. (2018b), we use GLOW, driven with ionospheric background conditions, to generate a lookup table of emission line intensities for a variety of driving precipitation energy spectra. Each energy spectrum in the table is parameterized by its values of Q_p and $\langle E \rangle$, and GLOW simulates emission line intensities separately for each.

After denoising and calibrating the imagery, mapping each color to its rough emission altitude, and removing background brightness, we apply a simple Python routine¹ that uses the lookup tables to invert each usable pixel of the image to a value of Q_p and $\langle E \rangle$, along with rough error bars associated with the inversion. After inversion, all precipitation maps are Gaussian smoothed in the magnetic northward direction with a window size of 32 km ($\sigma \approx 5.3$ km).

3.2.2 Swarm Spacecraft

The European Space Agency's Swarm mission consists of three satellites which were launched into nearly polar, low Earth orbits on 22 November, 2013, with the goal of providing highly detailed measurements of variations in the Earth's magnetic field. We use their version 0401, level 2 FAC data derived down to 1 Hz from the Vector Field Magnetometer (Ritter et al., 2013, VFM,) data, along with their version 0302, level 1B Electric Field Instruments data, specifically the 2 Hz TII ion drift measurements (Knudsen et al., 2017; Burchill and Knudsen, 2022). The TII data, like the precipitation maps, are Gaussian smoothed to 32 km, while the FAC data are smoothed to 16 km ($\sigma \approx 2.7$ km) to account for the differential relationship between the \mathbf{E} and $\Sigma_{P,H}$ maps, and j_{\parallel} (see Equation 3.1). The

¹<https://github.com/317Lab/asispectralinversion>

ion drift measurements have a 100 – 200 m/s one-sigma accuracy, and are used only in our discussions (Section 3.5) as a point of comparison with our simulation results.

We note that the choice of smoothing window, an important and carefully deliberated choice, strongly affects the science scales we can investigate. The specific smoothing window is chosen to match and align the available input data scales; we know that driving the model with inconsistent drivers (i.e., fine-scale fields data and large-scale imagery) leads to spurious signatures. For this study, therefore, we have not fully characterized the dependence on this scale choice. Instead we focus our studies on permutations of input parameters at these scales (i.e. on/off or from instrument A versus instrument B and so on).

3.2.3 Poker Flat Incoherent Scatter Radar

The Poker Flat Incoherent Scatter Radar (Kelly and Heinselman, 2009; Nicolls and Heinselman, 2007; Heinselman and Nicolls, 2008, PFISR,) is an Advanced Modular Incoherent Scatter Radar facility and has been operational since 2007. PFISR is located at the Poker Flat Research Range (212.53° E, 65.13° N), which is owned by the University of Alaska Fairbanks Geophysical Institute, and the radar is maintained for the US National Science Foundation by SRI International. The antenna boresight points at an azimuth of 15° east-of-north and elevation of 74° . In this paper, we take single-value, uniform averages of plasma drift velocity within the latitude ranges of our simulation regions, and use these averages as large-scale background flow estimates. We use their resolved vector velocity (“vvels”) data based on long pulse experiments with a five minute integration time. These data products are produced by Python scripts found at <https://zenodo.org/records/10892410>. We use these data to provide one plasma drift velocity average per conjunction event.

3.2.4 Super Dual Auroral Radar Network

The Super Dual Auroral Radar Network (SuperDARN) is comprised of 35+ HF and VHF radars located across the northern and southern hemispheres and is operated by 20 institutions across 10 nations. This paper uses plasma convection flow estimates over Poker Flat, AK—one global estimate per conjunction event—that are interpolated by the pyDARN open-source python library. Greenwald et al. (1995) describe the SuperDARN global-scale network and the pyDARN repository can be found at <https://zenodo.org/records/14796490>. SuperDARN convection map data shown in this paper was processed using the FITACF3 algorithm with a spectral width-based Heppner-Maynard Boundary. Both the order and

degree of the fit was 6.

3.2.5 FAC Replication

Our simulations require spatially continuous, *F*-region ionospheric FAC maps. van Irsel et al. (2024) outline how this can be done for electrostatic plasma convection maps. Here we have adjusted their methods for FAC maps instead. The replications can be done using distributed optical data, provided by all-sky, multi-spectral imagery, combined with FAC data tracks, provided by spacecraft or sounding rockets. We first invert the imagery using methods outlined in Section 3.2.1, from which preliminary estimates of the height-integrated conductivities (conductances) are gathered. The conductance maps are then queried for two iso contours at user-defined conductance values which are the primary and secondary arc boundaries. With these boundaries, the replication process is as follows:

1. The original FAC data track is translated in the east-north plane by some amount following the primary arc boundary such that the original and replicated data are equal at the primary boundary-track intersections.
2. The replicated data track is scaled in the along-track direction such that the original and replicated data are equal at the intersections of the secondary boundary and the tracks.
3. This replication is repeated for multiple translations along the arc until the top-boundary is filled with FAC values at a sufficient replication density.
4. The replicated FAC data map is then interpolated onto the simulation grid, providing the top-boundary simulation driver.

For replications whose data lie just outside of the simulation region, the arc boundaries are extrapolated, ensuring sensible matching between FAC and precipitation.

3.2.6 GEMINI Simulations

Simulations for this study use the Geospace Environment Model of Ion-Neutral Interactions (Zettergren and Semeter, 2012; Zettergren and Snively, 2019, GEMINI,). GEMINI solves for 3-D electrostatic current continuity and ionospheric Ohm’s law, accounting for changes in state parameters which affect conductivities as it steps forward in time; it calculates the electric field that is consistent with how the top-boundary FAC requirements connect through the ionospheric volume—one whose conductivity is

highly sensitive to impact ionization from electron precipitation, which is implemented into GEMINI using methods by Fang et al. (2008, 2010).

GEMINI is a multi-fluid model (six ion species and electrons) that is quasi-electrostatic with calculations of particle continuity consisting of chemical production/loss and photo/impact ionization. Calculations of local densities, plasma flows, and temperatures are treated self-consistently and the model includes thermal conduction heat flux, collisional heating, thermoelectric electron heat flux, and inelastic cooling/heating from photoelectrons. This is supplemented with Maxwell's equations and, at the time of writing, includes no displacement current or magnetic induction. With this, the system is solved through enforcing divergence-free currents, curl-free electric fields, and invoking Ohm's law. GEMINI can be driven with (aside from maps of precipitation energetics handling impact ionization) a map of FAC *or* electric potential at the top-boundary. When driving GEMINI with a top-boundary map of FAC, a user-specified background electric field, \mathbf{E} , is input separately. GEMINI assumes equipotential magnetic field lines, providing horizontal electric fields that are constant in altitude (Farley Jr., 1959). For a full description of the governing equations solved by GEMINI, see Zettergren and Snively (2015, Appendix A).

3.2.7 Electron Precipitation Methods

Electron Precipitation Energy Spectra

For auroral arc systems, electron precipitation energy spectra, $\phi(E)$, are often assumed to be of a standard unaccelerated Maxwellian form (Fang et al., 2008) whose differential number flux, $\phi_u(E)$, is

$$\phi_u(E) = \frac{Q_p}{2E_0^2} \frac{E}{E_0} \exp\left(-\frac{E}{E_0}\right), \quad (3.4)$$

where Q_p is the total precipitating energy flux, E_0 is the characteristic energy, and E is the precipitation energy. This has its flux peak at an energy of E_0 , representing the arc energy, however, it also incurs an energy spread of

$$\sqrt{\langle (E - E_0)^2 \rangle} = \sqrt{\frac{\int_0^\infty (E - E_0)^2 \phi_u(E) dE}{\int_0^\infty \phi_u(E) dE}} = \sqrt{3}E_0. \quad (3.5)$$

In contrast to this formulation, in auroral situations, there is often an accelerated signature (Evans, 1968; Paschmann et al., 2003), where the energy spread is related to the source region thermal motions, while the peak energy is related to the auroral acceleration region (Evans, 1974). Therefore, we look at an alternative $\phi(E)$; that of an accelerated Maxwellian whose

differential number flux, $\phi_a(E)$, is (see Appendix A.2)

$$\phi_a(E) = \frac{Q_p}{T_s^2 + (T_s + U_a)^2} \frac{E}{T_s} \exp\left(-\frac{E - U_a}{T_s}\right), \quad E \geq U_a, \quad (3.6)$$

where T_s is now the source region characteristic energy, and U_a is the auroral acceleration region potential drop. With $U_a/T_s \sim 3$, which is not untypical, this has an energy spread of $\sqrt{3}T_s$. This choice for $\phi(E)$ has decoupled the energy spread and peak energy, which in this case is U_a when $U_a > T_s$, which is the case for all our conjunction events.

Relationships between the acceleration potential and the source region/ionospheric characteristic energy exists via the FAC this system holds (Knight, 1973; Rönnmark, 2002), but these are not the focus of this paper. Equation 3.6 is implemented into GEMINI using methods described by Fang et al. (2010). Both the GLOW model and the methods described by Fang et al. (2008, 2010) take into account secondary and back-scattering electrons (Evans, 1974).

Figure 3.2 shows examples of $\phi_u(E)$ and $\phi_a(E)$ (Equation 3.4 and 3.6) with $U_a = E_0 = 3$ keV and $T_s = 490$ eV. Both these spectra have the same integrated energy flux, Q_p , and both peak at 3 keV, yet the accelerated Maxwellian has a significantly lower energy spread: 0.8 keV compared to 5.2 keV in the unaccelerated case. Along with this, their respective electron density altitude profiles are shown, determined using the GLOW transport model (Solomon, 2017). It is evident that the assumption of $\phi_u(E)$ can overestimate the electron density at lower altitudes given the high energy tail of these spectra. It is noted that with $U_a = 0$, i.e. no auroral acceleration, we have $\phi_a/\phi_u = 1$, which covers the relatively low energy background precipitation surrounding auroral arcs. This fact is what we use to determine T_s .

Determining Source Region Characteristic Energies, T_s

The differential number flux for an accelerated Maxwellian population approaches that of the unaccelerated population as U_a approaches zero. In this limit T_s becomes analogous to E_0 , thus, in order to find an estimate for T_s , we first invert the imagery (see Section 3.2.1) assuming an unaccelerated population, which provides a map of E_0 . Figure 3.3, panels a – b, show this map of E_0 and the total energy flux, Q_p , for our February 10, 2023 event.

Next, assuming that U_a vanishes outside of discrete auroral arcs, we filter the arc region out of this map of E_0 by removing pixels corresponding to the top 40th percentile of Q_p . We also remove the lower 30th percentile of the red emissions, as the inversion to E_0 performs sub-optimally for lower red intensities. This is shown in Figure 3.3c. We then look at the histogram

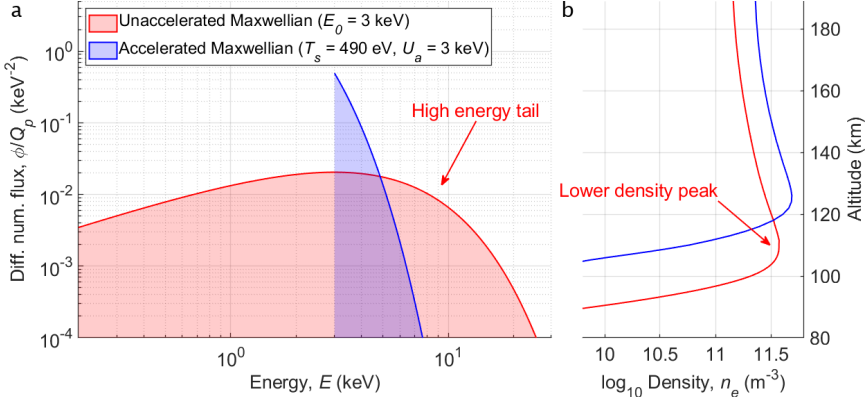


Figure 3.2: Comparison between unaccelerated and accelerated Maxwellian electron precipitation spectra. (a) Normalized energy spectra of $\phi_u(E)/Q_p$ (red) and $\phi_a(E)/Q_p$ (blue). Note that both spectra peak at 3 keV. (b) Electron density altitude profiles modeled by GLOW (Solomon, 2017) with the same color scheme.

of the remaining E_0 values and fit a Gaussian magnitude distribution to it, the peak of which is selected as the source region characteristic energy. In this case, we have $T_s = 490$ eV, as is shown in panel d. This panel also shows the unfiltered distribution which shows two distinct populations, suggesting different physics behind them—presumably that of the accelerated electrons and that of the unaccelerated precipitation.

The percentiles used in filtering are chosen by simultaneously minimizing the 95% confidence range and maximizing the adjusted R-squared value of the fits. The different choices for these percentiles raise a rough precision of around $\pm 10 - 20\%$ surrounding the T_s estimations.

We assume this value of T_s to be constant over the relevant source region and use it in Equation 3.6, with which we perform the inversion described in Section 3.2.1. This inversion now happens over a (Q_p, U_a) parameter space, for a given T_s , instead of (Q_p, E_0) , when creating lookup tables, providing 2-D maps of Q_p and U_a . This is all done for each of the six conjunction events. Reassuringly, we find that inversions of these six events done with either the $\phi_u(E)$ or $\phi_a(E)$ assumptions provide nearly identical maps of Q_p ; however, as we will show, they imply quite different conductivity and current density distributions through the ionosphere.

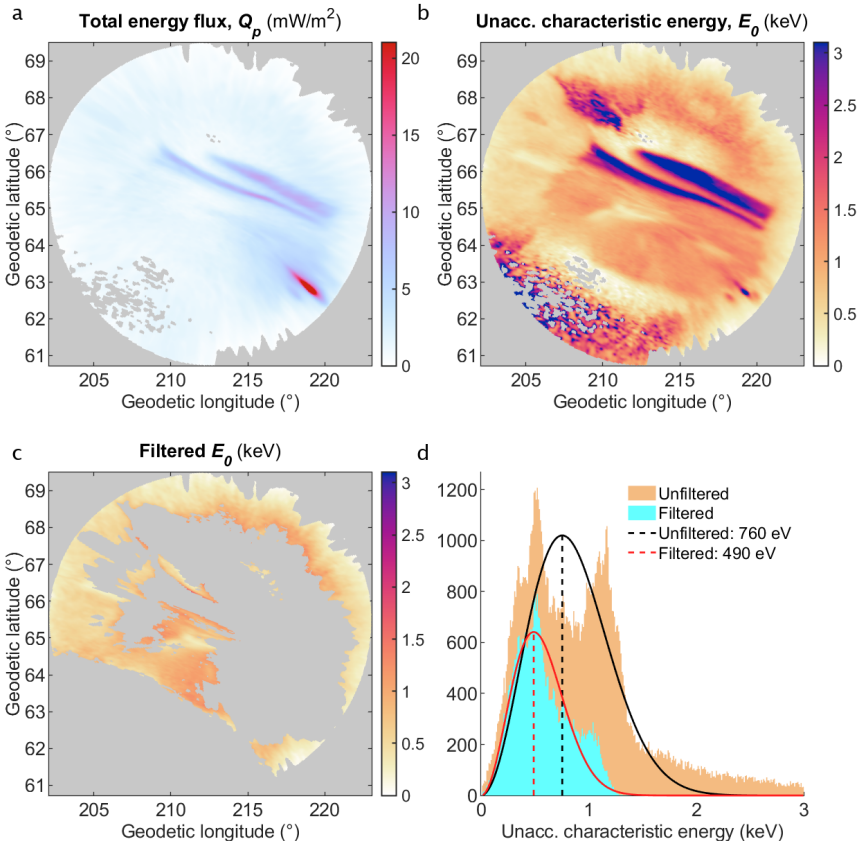


Figure 3.3: Steps in determining the source region characteristic energy. (a) The total precipitating electron energy flux, Q_p , inverted assuming unaccelerated Maxwellian energy spectra. (b) The characteristic energy, E_0 , inverted assuming unaccelerated Maxwellian energy spectra. (c) E_0 filtered by removing the top 40th percentile of Q_p and the lower 30th percentile of the red line emissions. (d) Histograms of data in panels b (orange) and c (light blue) along with Gaussian magnitude fits (black and red respectively) and their peaks (dashed). Data source: DASC (2025).

3.2.8 Current Flux Tube Visualization

In order to visualize current closure in GEMINI output data, we show flux tubes of electric current. GEMINI enforces $\nabla \cdot \mathbf{j} = 0$, where \mathbf{j} is the current density, which makes the usage of flux tubes as a visualization tool sensible. We have developed tools to generate current flux tubes starting at user-defined ellipses contained inside the GEMINI simulation volume. From these ellipses, a number of current vector streamlines are sourced, which, by definition, are tangent to \mathbf{j} throughout the simulation volume. This ensures the current flux through such ellipses is equal to the flux through the orientable surface enclosed by the curve connected by the streamline endpoints. Current fluxes are calculated for tubes that meet flat exit surfaces and are compared against entry fluxes as a check for numerical error. Streamline endpoints that are too far apart, or that meet at a corner of the simulation volume, are locations where the flux tube splits into multiple tubes. In this case, the fluxes of each tube are provided separately. This method of visualization is part of the toolset available at https://github.com/317Lab/aurora_gemini.

Figure 3.4 shows three example current flux tubes. This $425 \times 288 \times 384$ cell (up, east, north) magnetically aligned volume contains a GEMINI calculated 3-D current density from which the flux tubes are derived. In this paper, simulations are all located in the northern hemisphere and magnetic east, north, and up refer to a locally orthonormal basis with up being anti-parallel to the local magnetic field, east in the direction of increasing modified apex longitudes, and north completing the set. The simulation in Figure 3.4 is driven by a top-boundary map of FAC which is plotted at the bottom for visualization purposes. The colormap of FAC has red associated with the downward, parallel-to- \mathbf{B} (in the northern hemisphere) current vector, also referred to hereinafter as return current (i.e. “red is return”). The blue represents the upward current (downward-moving electrons in the Northern hemisphere) where, often, the accelerated auroral electron precipitation is found. On the eastern wall, a central cut of electron density is plotted. The density perturbations, which are in most part the result of the top-boundary precipitation driver maps, govern the 3-D conductivity volume and thus, in part, the current closure. The black arrows plotted on the FAC map are a sparse sample of the GEMINI calculated electric field—the second aspect governing the current closure—and the yellow arrow is the imposed constant, background convection electric field, $\bar{\mathbf{E}}$. The pink lines indicate the FAC data from, in this example, Swarm A and C, that are footpointed down to the top-boundary and plotted at the bottom as well (these form the basis of the replicated FAC map in red and blue).

The current flux tubes are color-coded for easy distinction. In this example, the red flux tube originates from an ellipse at the top-boundary

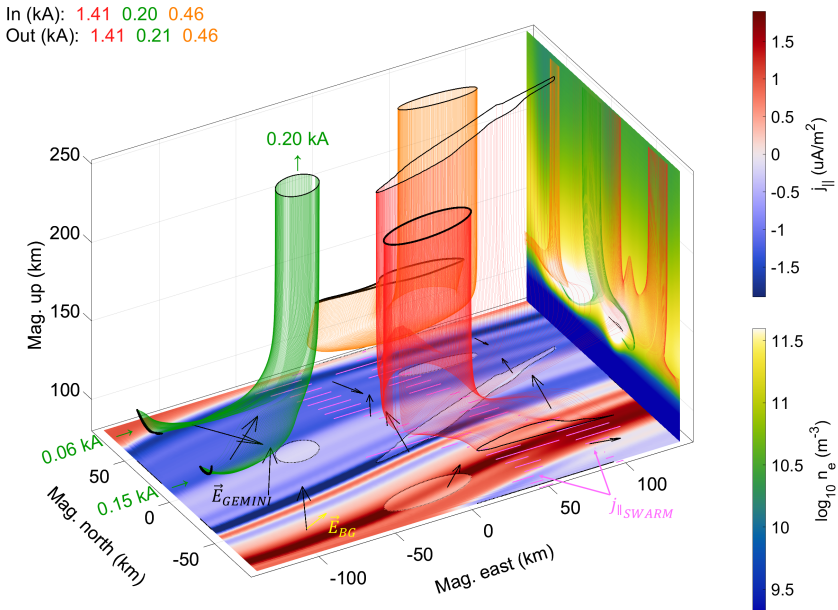


Figure 3.4: Example of a current flux tube plot using an example February 10 simulation. The top-boundary FAC driver is plotted at the bottom for visualization purposes. Similarly, a central cut of electron density is plotted at the eastern wall. The current flux tubes are color-coded for distinction purposes and start/end at the bold/thin solid curves. The black dashed lines are their counterparts projected on top of the FAC map. The pink lines indicate FAC data from Swarm A (right track) and C (left track) with parallel being right. The black arrows are a sparse sample of the electric field calculated by GEMINI and the yellow arrow indicates the constant background electric field. Data sources: Swarm (2025), Super-DARN (2025), and Simulations (2025).

inside the southernmost downward, return current sheet. It carries 1.4 kA down through the volume, splitting in three, finding its way out through the top-, south-, and east-boundary. The influx and outflux regions are outlined by bold and thin closed black curves, and shadows of these curves are projected to the bottom to visualize which portion of the FAC map they embody. The green flux tube has its user-defined ellipse in the upward current and is calculated in reverse. It carries around 0.2 kA from two sources on the western wall, combines into a single tube, and connects with the top-boundary. Lastly, the orange flux tube (also calculated in reverse) is sourced at the northern boundary and also connects to the upward FAC. Figure 3.4, and similar figures in the remainder of this paper, display in-and out-fluxes to two decimal places and illustrate the degree of precision of the flux tube calculations. Most current flux tubes in this paper are precise up to one decimal place, with a few exceptions of more complex current flux tubes or ones with higher amperage (> 10 kA).

3.3 Conjunction Events

This study uses a total of six conjunction events ranging from February 10 to March 19, 2023, from the Swarm-over-Poker-2023 campaign (Poker Flat Research Range, AK). As a summary of the conjunctions used in this work, Figure 3.5 shows the top-boundary simulation data-drivers for each of the six events: the total energy flux of the precipitating electrons, Q_p , the acceleration potential, U_a , and the FAC maps, j_{\parallel} , replicated from the Swarm data. Driver maps of E_0 or those of j_{\parallel} using fewer than all available spacecraft are not shown. Also plotted are the primary and secondary boundaries used in the replication process (see section 3.2.5) and the FAC data tracks themselves. In addition, Table 3.1 displays information regarding which Swarm spacecraft are part of the conjunction, the activity levels, the PFISR and SuperDARN background flow estimates, and the rough peak values of the simulation top-boundary drivers for each event. The distance from Poker Flat to the nearest SuperDARN plasma flow estimate, \bar{v}_{SD} , is denoted d_{SD} .

Not all events have PFISR data tracks available because either they are too far from their respective, chosen simulation regions, or the data are considered inadequate for our purposes. Also, not all of the events have a simulation using the unaccelerated assumption for $\phi(E)$. Determining plausible arc boundaries requires meticulous care and determines where the simulation boundaries are, which is why, for several conjunction events, the FAC data track(s) lie(s) just east or west of simulation region. In such cases, the arc boundaries are extrapolated to the data tracks. Following are brief synopses of each of the six conjunction events after which, in Section 3.4, we cover their simulation results.

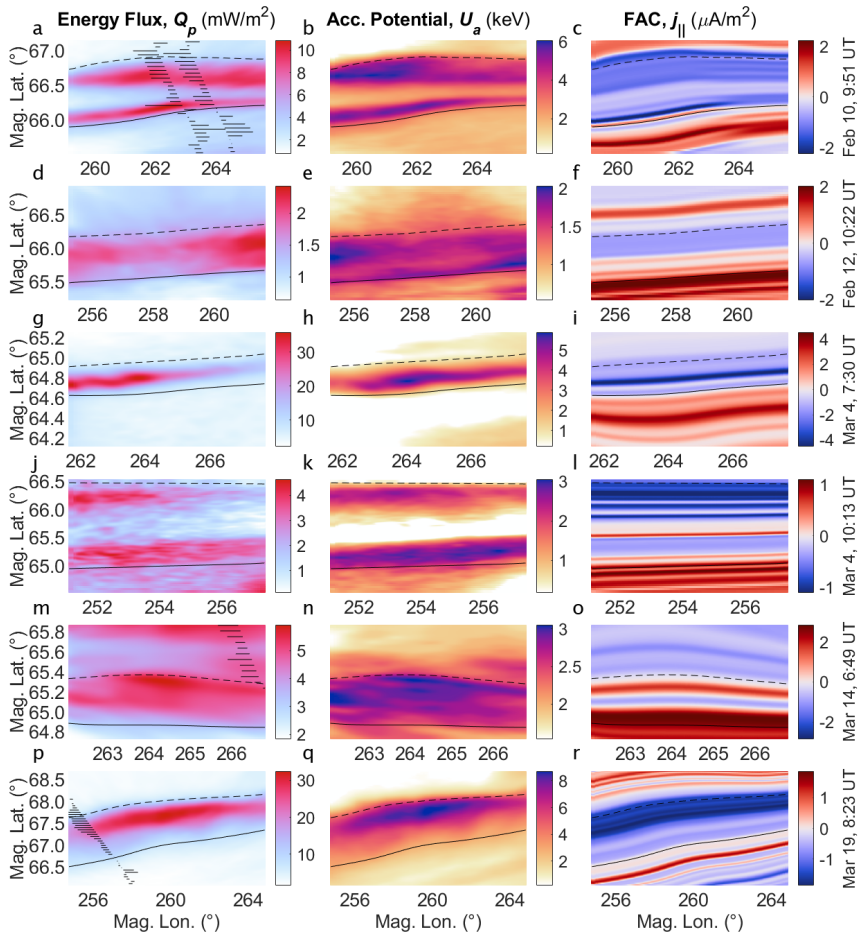


Figure 3.5: Top-boundary drivers of conjunction events. (a) The total precipitating electron energy flux, Q_p , for the February 10, 9:51 UT event. (b) The acceleration potential, U_a , for the same event. (c) The replicated FAC map, j_{\parallel} , for the same event. (d-r) Same format for remaining events. Note that the respective colorbars change per event. The solid black feather plot indicates the Swarm FAC data tracks with right being parallel. Not all Swarm data tracks are within the simulation volume and are thus not shown. Data sources: Swarm (2025) and DASC (2025).

Table 3.1: Summary of conjunction events with input map values^a.

Event ID	1	2	3	4	5	6
Date	Feb 10	Feb 12	Mar 4	Mar 4	Mar 14	Mar 19
Time (UT) ^b	9:51:27	10:22:11	7:30:12	10:13:49	6:49:07	8:23:30
MLT (Hours)	23.1	23.3	20.7	22.9	20.1	21.4
Region (km) ^c	290×182	290×189	290×126	290×225	220×126	432×291
Swarm S/C	A + C	C	C	B	A + C	B
Ap	15	7	16	16	18	9
F10.7 (a) (s.f.u.)	208 (175)	200 (175)	182 (161)	182 (161)	138 (162)	143 (162)
\bar{v}_{SD} (m/s) ^c	-14, 29	-170, -31	-323, 269	-45, 0	-200, -9	-494, 96
d_{SD} (km) ^d	51	51	184	373	51	375
\bar{v}_{PF} (m/s) ^c	-343, 2	-237, -17	-	-	-418, -44	178, -68
Q_p (mW/m ²) ^e	10.0	2.3	32.3	4.1	5.8	31.3
U_a (keV) ^e	5.8	1.9	5.4	2.9	3.0	8.5
T_s (eV)	490	580	800	860	240	680
E_0 (keV) ^e	4.2	1.4	4.0	2.3	-	-
j_{\parallel} ($\mu\text{A}/\text{m}^2$) ^e	-2.3, 2.0	-0.7, 1.9	-4.5, 3.8	-1.1, 1.0	-1.2, 2.8	-1.9, 1.4

^aVariables \bar{v}_{SD} , \bar{v}_{PF} , Q_p , U_a , T_s , E_0 , and j_{\parallel} are defined in-text.^bTimes indicate the spacecraft crossing approximately through the simulation center.^cRegions and flows are in GEMINI magnetic coordinates/components.^dDistances from Poker Flat to nearest SuperDARN data point.^eValues for Q_p , U_a , E_0 , and j_{\parallel} are 99% quantiles of maps within a 10 cell border.

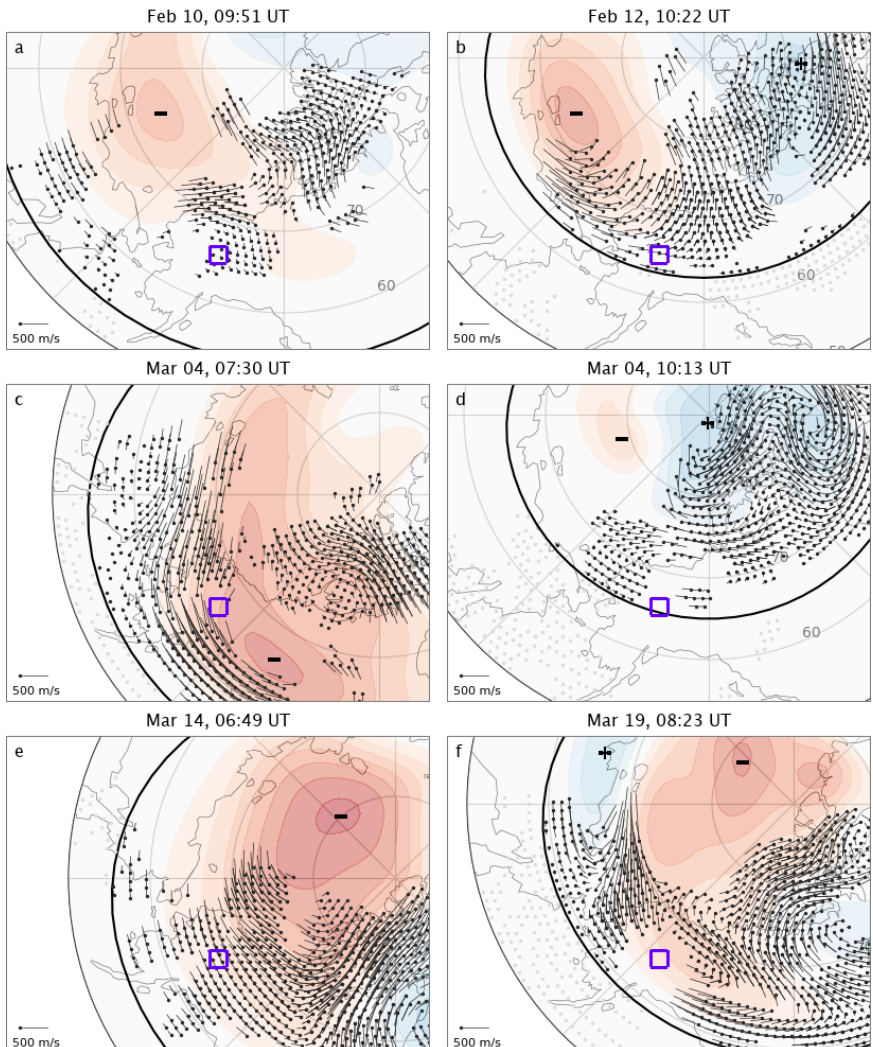


Figure 3.6: SuperDARN convection maps of conjunction events. Panels a – f represent event IDs 1 – 6 (see Table 3.1). Purple boxes are approximately centered on Poker Flat, AK and are on the order of the simulation sizes. The bold black line is the Heppner-Maynard Boundary. The colormap shows the electric potential and the “+” and “–” symbols indicate the maximum and minimum potential points. Local magnetic midnight is at the bottom and the dusk side is left. Data source: SuperDARN (2025).

3.3.1 February 10, 9:51:27 UT

Figure 3.5a – c: This event includes both Swarm A and C cutting through the center of the simulation around 47 km apart. It has a curved double arc precipitation pattern with each peaking around a total energy flux of $Q_p = 10.0 \text{ mW/m}^2$ and acceleration potential of $U_a = 5.8 \text{ keV}$. The precipitation is collocated with the FAC replication where the precipitating and return current sheets are between $j_{\parallel} = -2.3$ to $2.0 \mu\text{A/m}^2$. The PFISR convection flow data are positioned at the western edge of the simulation space and estimate a strong magnetic westward flow of $\bar{\mathbf{v}}_{PF} = (-343, 2) \text{ m/s}$. In contrast, SuperDARN estimates a nearly stagnant flow of $\bar{\mathbf{v}}_{SD} = (-14, 29) \text{ m/s}$. The Magnetic Local Time (MLT) is 23.1, however, as is shown in Figure 3.6a, the event occurs 3 – 4 hours duskside of the Harang discontinuity.

3.3.2 February 12, 10:22:11 UT

Figure 3.5d – f: This is a low flux, low energy, and generally inactive event with a Swarm A conjunction roughly 153 km west of the simulation space and with a PFISR data cut through the center. It has a single, blurry but straight arc of around $Q_p = 2.3 \text{ mW/m}^2$ and $U_a = 1.9 \text{ keV}$, with the FAC sheets ranging from $j_{\parallel} = -0.7$ to $1.9 \mu\text{A/m}^2$. Both PFISR and SuperDARN suggest a large westward flow of $\bar{\mathbf{v}}_{PF} = (-237, -17) \text{ m/s}$ and $\bar{\mathbf{v}}_{SD} = (-170, -31) \text{ m/s}$ respectively. The MLT is 23.3—roughly 1 hour prior to the Harang discontinuity.

3.3.3 March 4, 7:30:12 UT

Figure 3.5g – i: In contrast to the previous event, this one has an intense arc of $Q_p = 32.3 \text{ mW/m}^2$ and $U_a = 5.4 \text{ keV}$ with a Swarm C crossing around 141 km eastward of the simulation space and FAC data of $j_{\parallel} = -4.5$ to $3.8 \mu\text{A/m}^2$. This arc has reasonable along-arc structure; the total energy flux ranges from its peak to around 20 mW/m^2 going from west to east. Unfortunately, this event does not have usable PFISR data, but SuperDARN shows a very strong northwestern flow of $\bar{\mathbf{v}}_{SD} = (-323, 269) \text{ m/s}$. This strong, skewed flow is the result of a skewed two-cell convection pattern determined by pyDARN v4.1 (Greenwald et al., 1995) as shown in Figure 3.6c. The event’s MLT is 20.7, but this convection pattern places it around 5 – 7 hours before the two-cell split.

3.3.4 March 4, 10:13:49 UT

Figure 3.5j – l: This event, just under three hours later than the previous at an MLT of 22.9, has a straight double arc pattern at $Q_p = 4.1 \text{ mW/m}^2$ and $U_a = 2.9 \text{ keV}$ with Swarm B an average of 94 km westward of the

simulation. This event has $T_s = 860$ eV, which is 60 eV higher than 2.75 hours earlier, and the currents have now subsided down to $j_{\parallel} = -1.1$ to $1.0 \mu\text{A}/\text{m}^2$. Again, this event includes no PFISR data, while SuperDARN now estimates a stagnant flow of $\bar{\mathbf{v}}_{SD} = (-45, 0)$ m/s. Compared to the previous event, Figure 3.6d shows a much subdued convection pattern with the Harang region sits right around local magnetic midnight.

3.3.5 March 14, 6:49:07 UT

Figure 3.5m – o: This event is distinct in that it has its precipitation collocated with downward, rather than upward, FAC. There is a down-up-down FAC sheet set ranging from $j_{\parallel} = 2.8$ to -1.2 to $2.0 \mu\text{A}/\text{m}^2$ centered around a $Q_p = 5.8 \text{ mW/m}^2$, $U_a = 3.0 \text{ keV}$ precipitation pattern. It is also the second event with both Swarm A and C conjunctions. The reason for the apparent mismatch between precipitation and FAC can be the result of FAC data resolution, imagery inversion obliquity errors, or non-visible current carriers. Given that the data reduction methodology used is nearly identical in all of our conjunctions, it is reasonable that it is the latter case. Swarm A sits around 44 km east of the model space, while the Swarm C crossing is just inside at the northeastern corner, and the southernmost PFISR data point is located around 100 km west of the simulation. The direction of both the PFISR and SuperDARN convection flow estimates are very similar, however, the PFISR flow estimate of $\bar{\mathbf{v}}_{PF} = (-418, -44)$ m/s is around twice as strong as the SuperDARN estimate of $\bar{\mathbf{v}}_{SD} = (-200, -9)$ m/s. This 20.1 MLT event sits at around 2 hours duskside to the Harang discontinuity.

3.3.6 March 19, 8:23:30 UT

Figure 3.5p – r: The last event, and the second Swarm B conjunction, is unaligned to magnetic latitudes and has strong precipitation with along-arc structure; the energy flux peaks at around $Q_p = 31.3 \text{ mW/m}^2$ and subsides to around 20 mW/m^2 at the eastern and western boundaries. The acceleration potential is the highest among our events, peaking at around $U_a = 8.5 \text{ keV}$ and the FAC data range from around $j_{\parallel} = -1.9$ to $1.4 \mu\text{A}/\text{m}^2$. PFISR cuts through the center and estimates a flow of $\bar{\mathbf{v}}_{PF} = (178, -68)$, where SuperDARN estimates $\bar{\mathbf{v}}_{SD} = (-494, 96)$ m/s. The MLT is 21.4, however, Figure 3.6f shows a multi-cell convection pattern which gives a relatively nonstandard context.

3.4 Simulation Results

The six conjunction events are each simulated multiple times, iterating through different parameters, allowing the simulations to be systematically compared. This highlights and isolates the relevant physics involved and allows us to study sensitivities to these parameters. Table 3.2 provides the list of simulation comparisons covered in this paper (and its Supporting Information, Appendix C), labeled IDs I-XI, where individual simulations are denoted Ia, Ib, IIa, and so on. The comparisons are divided into three categories of feature permutations: (1) background convection flow and its source, (2) the assumption of unaccelerated versus accelerated Maxwellian precipitation spectra, and (3) single versus double spacecraft replications, highlighting along-arc FAC structure.

Each simulation has $425 \times 288 \times 384$ cells in the magnetic up, east, and north directions respectively and are simulated for 60 seconds with static drivers. The altitudinal extent is 80 – 507 km, with cell heights of 0.3 – 10 km respectively, and the magnetic east/north extents are given in Table 3.1 and Figure 3.5. Horizontal cell dimensions settle at 700 – 1400 m in the magnetic east direction, and 238 – 700 m in the magnetic north direction. Unless otherwise stated, all simulations default to SuperDARN background flow estimates, accelerated Maxwellian precipitation, and FAC replication using maximal data tracks. The simulations can be found at <https://rcweb.dartmouth.edu/LynchK/Gemini3D>.

3.4.1 Background Flow & Electric Field

There are two factors which dictate the existence of closure currents: (1) the Pedersen and Hall conductivities, and (2) the strength of the electric field. The conductivities require enhanced ionization at closure altitudes which is largely dictated by electron precipitation—enhanced energy fluxes, Q_p , increase the conductivity overall, while stronger acceleration potentials, U_a , give preference to Hall over Pedersen closure. Adding to this, spatial structure in the precipitation means that these conductivities have 3-D structure, affecting current closure in all directions. The magnitude of the electric field, however, dictates the magnitude of closure currents overall. We argue that strong electric fields can render the need for Hall closure to be negligible. We therefore begin by looking at comparisons of simulations that have different background electric field assumptions.

Figure 3.7 shows three view angles of the results for Simulation Ia, referenced in Table 3.2, where Section 3.2.8 explains the format of this figure. It uses FAC data from Swarm A and C, the accelerated Maxwellian precipitation assumption, and a background plasma flow estimate from SuperDARN. In this first example, the background flow of $\bar{\mathbf{v}}_{SD} = (-14, 29)$

Table 3.2: Summary of event comparisons^a

Category	ID	Datetime (UT) ^b	BG flow (m/s) ^c	BG source	Acc.	Swarm
			a	b	a	b
Background flow	I	Feb 10, 9:51	(-14, 29)	(-343, 2)	SD	PFISR
	II	Feb 12, 10:22	(-170, -31)	(-237, -17)	SD	PFISR
	III	Mar 4, 7:30	(-323, 269)	(0, 0)	SD	None
	IV	Mar 14, 6:49	(-200, -9)	(-418, -44)	SD	PFISR
	V	Mar 19, 8:23	(-494, 96)	(178, -68)	SD	PFISR
Accelerated vs. unaccelerated	VI	Feb 10, 9:51	(-14, 29)	-	SD	-
	VII	Feb 12, 10:22	(-170, -31)	-	SD	-
	VIII	Mar 4, 7:30	(-323, 269)	-	SD	-
	IX	Mar 4, 10:14	(-45, 0)	-	SD	-
Along-arc structure	X	Feb 10, 9:51	(-14, 29)	-	SD	-
	XI	Mar 14, 6:49	(-200, -9)	-	SD	-

^aComparisons are labeled I-XI with individual simulations labeled Ia, Ib, IIa, etc.

^bTimes indicate the spacecraft crossing approximately through the simulation center.

^cPFISR and SuperDARN background flows are in GEMINI magnetic east/north components.

m/s amounts to a constant background electric field of 1.6 mV/m directed roughly 26 degrees north-of-east (geomagnetic).

What follows are descriptions of three of our five comparisons (see Table 3.2) that outline the sensitivity of auroral current closure to the constant background electric field, $\bar{\mathbf{E}}$, around which GEMINI solves current continuity and Ohm's law for $\mathbf{E} = \bar{\mathbf{E}} + \delta\mathbf{E}$. The remaining comparisons, along with their associated figures and descriptions, can be found in the Supporting Information (Appendix C).

Comparison I: Background Flow

In Comparison I, we compare and contrast the use of SuperDARN derived background flow against using the PFISR observed background flow. Figure 3.7 illustrates three current closure paths of Simulation Ia, which assumes the SuperDARN background flow, and shows the complexity of current closure in a reasonably typical discrete auroral arc system. The red current flux tube, carrying 1.4 kA, starts at the center of southernmost return current sheet and rotates to closure currents at an altitude range of 110 – 150 km. The bulk of the current continues northward, however, 0.2 kA exits through the southern boundary and > 0.1 kA exists through the eastern boundary. Focusing on the remaining 1.2 kA, panel c shows that this segment opens up to the northeast, aligning the tube with the electric field at first, i.e. Pedersen closure. The relatively weak strength of the electric field, however, renders the Pedersen closure infective and requires the tube to traverse through lower altitudes to find sufficient paths for closure. At these lower altitudes, the Hall currents dominate and thus this portion of the tube rotates perpendicular to the electric field. This increases the length it has to travel while crossing into the upward FAC region and stretches the overall current closure morphology in the along-arc direction. The portion which exits through the eastern wall, presumably, would follow this same pattern somewhere outside the simulation volume, but this is speculative. More notably, however, the remaining unclosed portion on the southern part of the tube traverses southward, but this is for the same reason: the tube rotates in the Hall layer looking for upward FAC somewhere outside the simulation.

The green tube is sourced from the western boundary with two ends, both carrying around 0.1 kA, which combine into a single, 0.2 kA upward segment of the tube closing in between the two precipitation current sheets. Panel a shows how they cling to the higher density, i.e. higher conductivity, regions caused by the double-arc precipitation; they wrap around these density enhancements in the northward direction following the local electric field.

The orange tube is sourced from the northern boundary with 0.5 kA

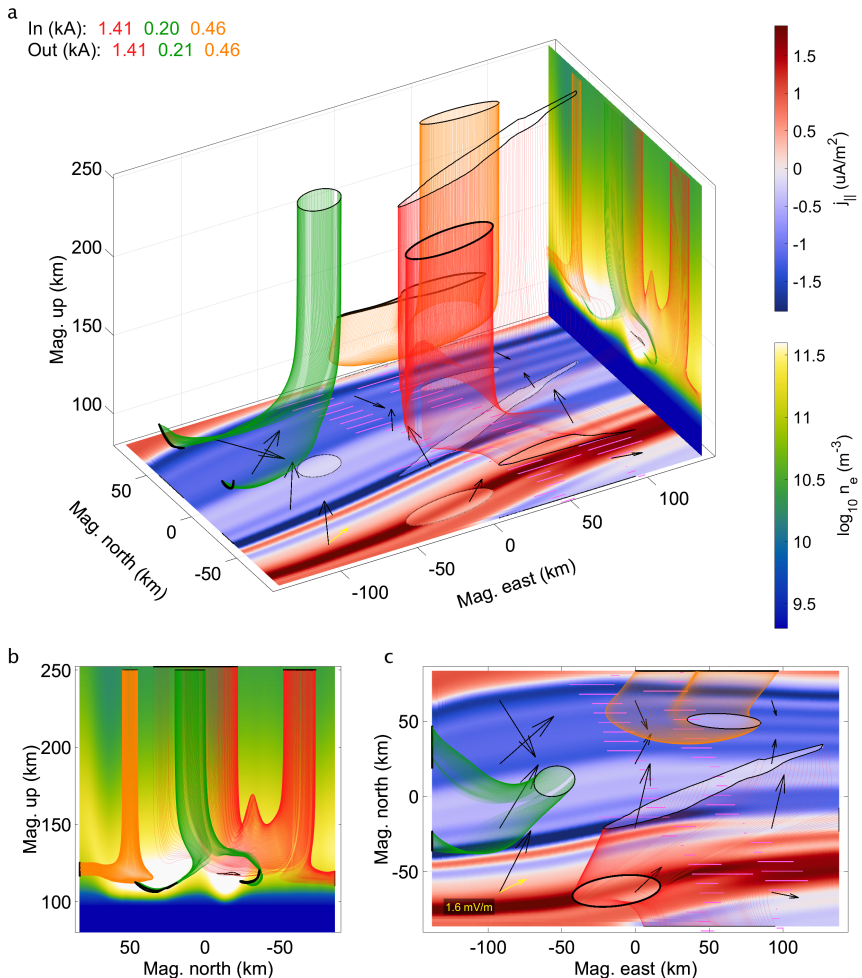


Figure 3.7: Isometric (a), side (b), and top (c) view of the GEMINI results for Simulation Ia. For plot details, see Section 3.2.8. Data sources: Swarm (2025), SuperDARN (2025), and Simulations (2025).

and travels southward, somewhat aligned to the electric field, before it hits an electric field convergence. Thus, to avoid going against the electric field, the flux tube lowers in altitude, in search of Hall conductivity, and abruptly turns to the east. This outlines the self-consistency aspect of the nature of auroral current closure—the flux tube (a) lowers in altitude where (b) the density is higher, (c) the electric field converges, and (d) the Hall conductivity increases allowing for an eastward turn, all spatially coincident. Finally, the tube further rotates to gain just enough Pedersen current, and hence altitude, to allow for a connection with the upward FAC sheet. This current flux tube, along with the previous two, highlights a set of 3-D considerations needed when trying to understand current closure morphology, and thus MI coupling. This is especially true when Hall currents are required in this closure, which is the case for Simulation Ia, given its weaker electric field.

In contrast, Figure 3.8 shows three current flux tubes for Simulation Ib (panels c – d) that capture the same FAC regions, whether at the start or end of each tube. The only change here is that the simulation now assumes the PFISR derived constant background flow of $\bar{\mathbf{v}}_{PF} = (-343, 2)$ m/s, which amounts to 17.2 mV/m directed nearly northward compared to the northeasterly 1.6 mV/m from Simulation Ia (panels a – b). This larger background flow drastically changes the current closure morphology of all three flux tubes. Given the tenfold increase in the electric field magnitude, on top of a more direct Pedersen pathway across the arcs, the Pedersen closure has become significantly more effective. Panels a and c show an increase in closure altitudes of 110 – 150 to 130 – 180 km, which means the Hall layer is virtually untouched by these Simulation Ib closure patterns. Panel d solidifies this idea, as all three tubes follow the electric fields almost directly. This outlines the ability of the background electric field, $\bar{\mathbf{E}}$, to actively drive auroral arc systems in conjunction with the top-boundary map of j_{\parallel} .

To emphasize the sensitivity to the background electric field from the perspective of energy dissipation, panels e – f of Figure 3.8 show the height-integrated Joule heating for Simulations Ia – b respectively. They show the extent to which this auroral arc system can be an electrostatic load, and how $\bar{\mathbf{E}}$ can change this greatly; aside from having an order-of-magnitude higher electric field strength, Simulation Ib also closes mostly in Pedersen currents—parallel to the electric field—both facts favoring higher $\mathbf{j} \cdot \mathbf{E} = \sigma_P |\mathbf{E}|^2$ values throughout. Not only does this increase the Joule heating for Simulation Ib, it also relocates a bulk portion of it equatorward of the precipitation.

The simulations in the next comparison, Comparison III, have a similar disparity in electric field strengths, yet both have higher FAC requirements, dictating a larger need for closure currents. However, they both also have

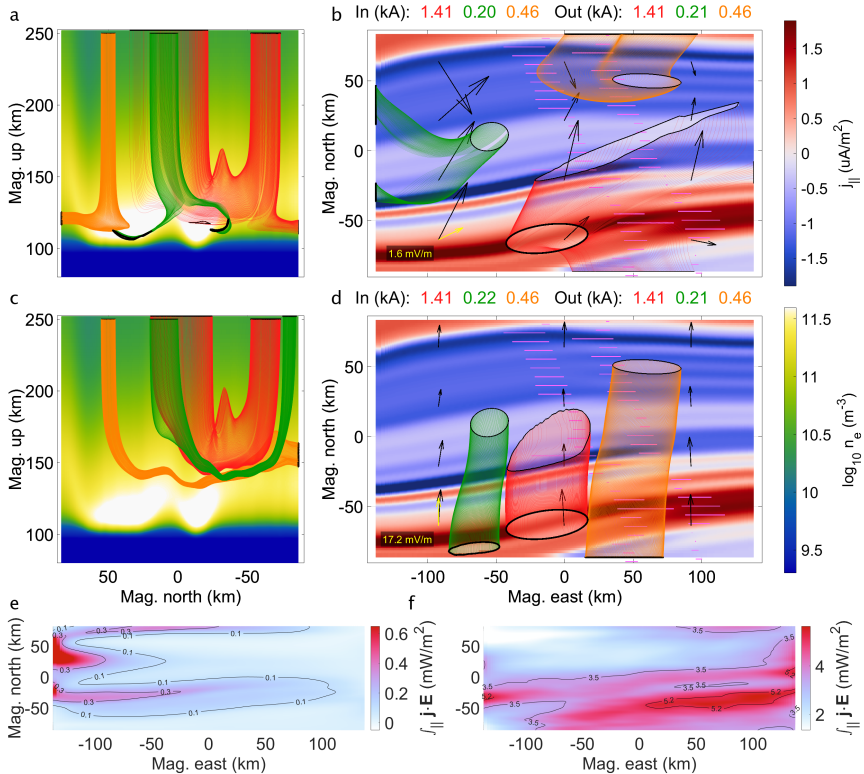


Figure 3.8: Comparison I (February 10, 9:51 UT): Top and side views of Simulation Ia with SuperDARN derived background flow (a, b) versus Simulation Ib with PFISR derived background flow (c, d) along with height-integrated Joule heating for Simulation Ia (e) and Ib (f). For plot details, see Section 3.2.8. Data sources: Swarm (2025), SuperDARN (2025), PFISR (2025), and Simulations (2025).

more precipitation; a factor which partially fulfills this need for additional closure.

Comparison III: Background Flow

The conjunction event for Comparison III, unfortunately, occurs too far from the PFISR field-of-view and therefore has no PFISR-deduced background flow estimate. Nevertheless, Figure 3.9 demonstrates the sensitivity to the choice of background flow by looking at Simulation IIIa, where the SuperDARN derived background convection amounts to 21.0 mV/m directed 40 degrees east of north (first row), and comparing it to Simulation IIIb, which has the background flow set to zero, as there is no estimate for it (second row). As explained in Section 3.1, having zero background electric field amounts to assuming most of the top-boundary FAC, j_{\parallel} , comes from electric fields caused by local polarization, $\delta\mathbf{E}$, alone. This comparison shows how much such an assumption affects current closure. Note that, with $|\bar{\mathbf{E}}| = 0$, for illustration purposes, the electric field label (black here) indicates the magnitude of the GEMINI calculated electric field vector shown nearest the label.

Comparisons I and III both look at simulations whose difference in their electric field strengths is an order-of-magnitude and both cover conjunction events whose acceleration potentials peak at around $U_a = 5$ keV. Comparison III, however, has the precipitation energy flux more than triple, and FAC requirements roughly double, with respect to Comparison I (see Tables 3.1 and 3.2). This creates a higher need for current closure—a need partially fulfilled by increased conductivity at all altitudes and the strong electric field strength. Hindering these needs, however, is the less direct path for Pedersen closure given the roughly 40 degrees angle at which the electric field crosses the arc in Simulation IIIa. The combination of these features allows us to look at how the sensitivity to electric field strength is affected by a different arrangement of auroral arc parameters.

Simulation IIIb, with $\bar{\mathbf{E}} = 0$, depicts a typical perspective of discrete aurorae (Marghitu, 2012)—an arc-aligned line of diverging electric field at the downward current sheet, and a converging one at the upward current sheet, as suggested by Equations 3.1 – 3.3. In this simulation, this is the result of the absence of a background electric field causing current continuity and Ohm’s law to be solved with electric fields from local polarization alone. The red flux tube in Simulation IIIb digs deep into the Hall layer while closing and is forced to split when bottoming out. This causes 0.4 kA to exit through the southern wall, 0.7 kA through the top-boundary, and > 0.1 kA through the eastern wall. (Note that this tube loses around 0.2 kA throughout its path which is a result of edge effects at the eastern wall). In contrast, the order-of-magnitude higher electric field in Simula-

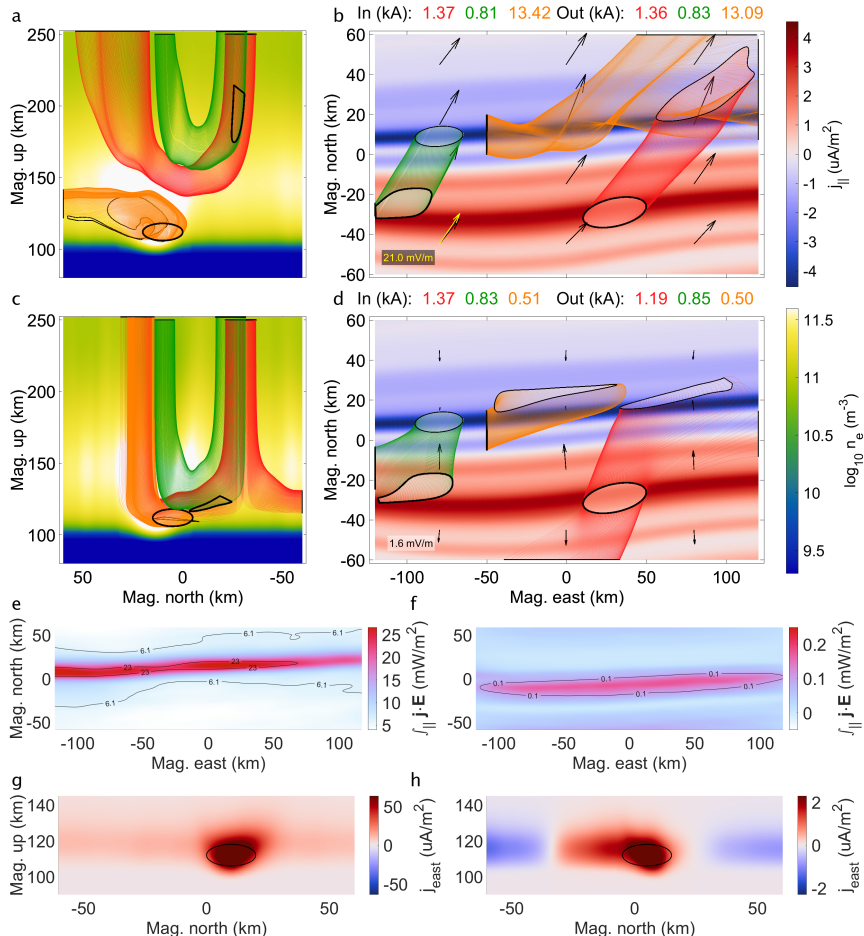


Figure 3.9: Comparison III (March 4, 7:30 UT): Top and side views of Simulation IIIa with SuperDARN derived background flow (a, b) versus Simulation IIIb with no derived background flow (c, d) along with height-integrated Joule heating for Simulation IIIa (e) and IIIb (f). (g, h) North-up slices of the magnetic eastward current component for Simulations IIIa – b respectively taken at 50 km west from center with the start curves of their respective orange flux tubes (solid black). For plot details, see Section 3.2.8. Data sources: Swarm (2025), SuperDARN (2025), and Simulations (2025).

tion IIIa means that its red flux tube carries that 1.4 kA from the return current sheet across to the precipitation sheet all throughout Pedersen altitudes and, thus, its closure is directed almost completely in the electric field direction. Contrarily, the green flux tubes for both simulations close largely with Pedersen currents given that their ends are relatively near one-another. Even though the green Simulation IIIb flux tube finds its closing currents at lower altitudes, it is still mostly dominated by Pedersen conductivity throughout; only the bottom apex of this tube veers to the across-E direction.

Morphologically speaking, the most striking difference between Simulations IIIa and IIIb lies in their connection to the electrojet current. Figure 3.9, panels g – h, for Simulations IIIa – b respectively, show a slice of the magnetic eastward component of \mathbf{j} taken at 50 km west-from-center, along with the intake ends of their respective orange flux tubes in panels a – d. With its stronger electric field, Simulation IIIa has a much higher electrojet current. This makes this auroral arc system closely resemble a 3-D version of the description from Section 4 by Marghitu (2012): A “thick uniform 2-D arc” whose current closure is separated into a thin Pedersen and Hall layer as shown by Fujii et al. (2012). Expanding on this description, here we show how current flux tubes can navigate around each other in a coherent and self-consistent way by venturing into the 3-D perspective.

Given the more complex shape of the orange flux tube in Simulation IIIa, Figure 3.10 shows the isometric view of the simulation results, in addition to the side and top views in panels a – b from Figure 3.9. Here we see the almost helical shape of the orange Simulation IIIa current flux tube, resembling that of Example 3 by Mallinckrodt (1985) but in 3-D. This tube captures 13.4 kA of the electrojet current, while its Simulation IIIb counterpart carries around 0.5 kA. Both intake ellipses have the same dimensions and are centered on their respective peaks of magnetic eastward currents slices. The simulations both have the same relatively strong precipitation arc ($Q_p = 32.3 \text{ mW/m}^2$, $T_s = 800 \text{ keV}$) around 10 – 20 km north, resulting in a high amount of impact ionization at relatively lower altitudes. This provides plenty of Hall conductivity and, thus, has both simulations susceptible to strong electrojet currents. These currents, however, are still proportional to the electric field strength which is why the order-of-magnitude increase in electric field results in a similarly increased electrojet current.

The enhanced electrojet current in Simulation IIIa does not partake in parallel current closure, whereas the Simulation IIIb electrojet current *is* required in the coupling of magnetospheric currents. As mentioned before, the lower electric field strength overall renders all closure currents less effective, hence the FAC has to rely on enhanced conductivity—Pedersen and then Hall—to connect. Naturally, Simulation IIIa is a more energetic

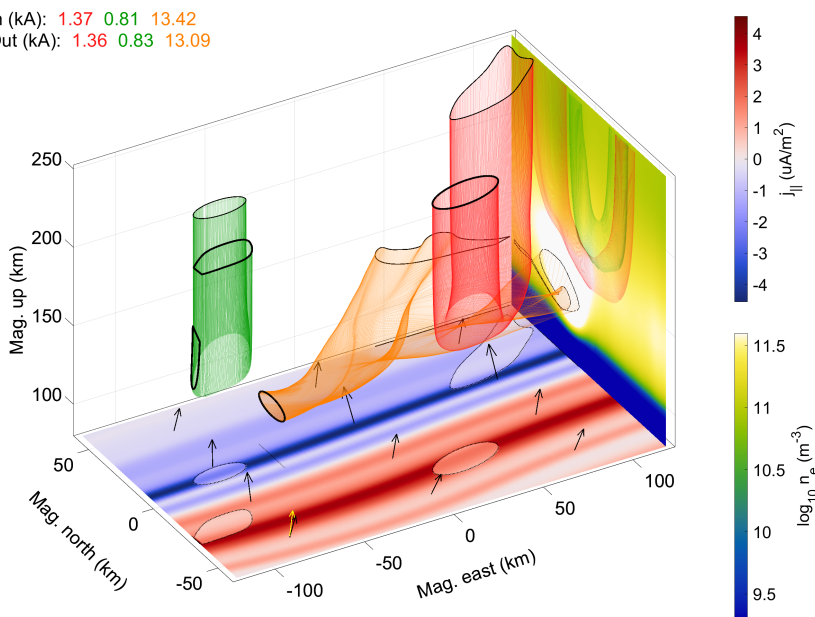


Figure 3.10: Isometric view of the GEMINI results for Simulation IIIa. For plot details, see Section 3.2.8. Data sources: Swarm (2025), SuperDARN (2025), and Simulations (2025).

configuration in terms of Joule heating; the integrated Joule heating peaks are at around 26.6 mW/m^2 and 0.17 mW/m^2 for Simulations IIIa – b respectively, as shown in panels e – f of Figure 3.9. This is consistent with the order-of-magnitude difference in electric field strengths, given the $|\mathbf{E}|^2$ relationship. Given that Hall currents are dissipationless (Kaepller et al., 2012), Simulation IIIb is thus able to rely on the electrojet currents for closure instead. In Simulation IIIa, the electrojet largely is assumed to follow the global-scale convection pattern D-shaped Hall currents instead, and is much less involved in auroral FAC closure.

As with Comparison I (as well as II and IV in the Supporting Information, Appendix C), here, yet again, we see that a sufficiently large background electric field has FAC close with Pedersen currents, and thus in the direction of the electric field. Even with the less-direct Pedersen pathway for closure and the higher FAC requirements, the strong electric field and relatively large precipitation energy flux provides sufficient conductivity at higher altitudes and renders Pedersen closure to be the dominant method in MI coupling for Simulation IIIa. Furthermore, the Simulation IIIb solution features a distinct $\nabla \cdot \mathbf{E}$ signature. In Simulation IIIa, however, this signature is masked by the its large background electric field (compared to no background field in Simulation IIIb). This emphasizes the dominance of the $\nabla \Sigma_{P,H}$ terms in balancing the FAC map for auroral systems with large electric fields. Next, we move onto Comparison V whose simulations both have strong electric fields, yet in severely different orientations.

Comparison V: Background Flow

Simulation Va assumes a background electric field of 25.2 mV/m directed 11 degrees east of magnetic north as estimated by SuperDARN. In the almost complete opposite direction to this, Simulation Vb has PFISR estimate 9.5 mV/m directed 21 degrees west of south. This results in drastic differences in both current closure morphology and Joule heating, as depicted by Figure 3.11. Both the red and green flux tubes completely flip directions in their current closure. The green flux tube, in its attempt to connect to the broad, primary precipitation current sheet, changes from sourcing its roughly 5.3 kA from the southwest corner in Simulation Va, to doing so from the northern end in Simulation Vb. The red flux tube, closing the southern primary downward current sheet, simply flips direction by following the electric field, and, interestingly, in both simulations it ends up skipping over an adjacent, lesser downward current sheet when closing its 0.8 kA .

As shown in panels g – h of Figure 3.11, the orange flux tube, like in Comparison III, captures the electrojet current for both Simulations Va – b. (Here, the user-defined ellipse sits at 0 km east and the tube is calculated in

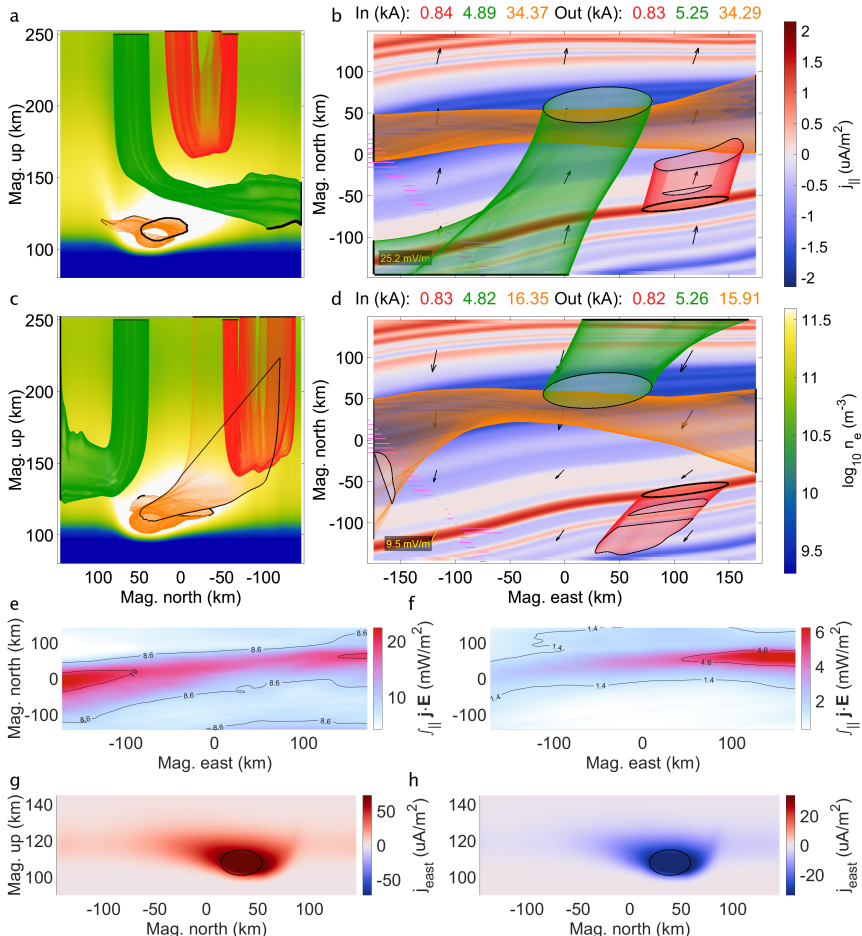


Figure 3.11: Comparison V (March 19, 8:23 UT): Top and side views of Simulation Va with SuperDARN derived background flow (a, b) versus Simulation Vb with PFISR derived background flow (c, d) along with height-integrated Joule heating for Simulation Va (e) and Vb (f). (g, h) Central north-up slices of the magnetic eastward current component for Simulations Va – b respectively with the start curves of their respective orange flux tubes (solid black). For plot details, see Section 3.2.8. Data sources: Swarm (2025), SuperDARN (2025), PFISR (2025), and Simulations (2025).

both directions.) As expected, this flux tube also flips its orientation, with the current flowing from west-to-east in Simulation Va, and east-to-west in Simulation Vb. However, like in Comparison III (Figure 3.9) but to a lesser extent, the weaker electric field strength in Simulation Vb requires the need of this electrojet current to help close some of the FAC, 0.3 kA in this case. The 62% weaker field also has reduced this Hall current flux tube by about 52%.

As in Comparisons I and III, the height-integrated Joule heating shown in panels e – f of Figure 3.11 varies roughly in proportion to the electric field strength squared. One notable difference, however, lies in the tapering off of this Joule heating in simulation Vb. This indicates that the western boundary of this simulation relies more on Hall closure; an idea supported by the electrojet usage in FAC closure depicted by the orange flux tube in panels c – d. Regardless of the reasoning behind this, Comparison V has shown that a mere directional change in the background electric field completely changes the connectivity of a given map of FAC. It is tempting to assume that a precipitation current sheet connects with its closest adjoining return current sheet, but as we have shown here, knowledge of the global-scale convection has considerable influence when it comes to FAC connectivity.

Summary: Background Flow

Auroral arc systems are very sensitive to the electric field in matters of current closure. Given that there are many self-consistent solutions for \mathbf{E} in Equation 3.1 that can be considered geophysical, we have shown here that it is crucial to get a good estimate of the global background flow in order to properly interpret behavior at auroral arc scales. In terms of simulation confidence, we can have more trust in simulations whose sources for background electric field estimates agree, such as Comparisons II and IV. However, when attempting to best understand the auroral arc system pertaining to a particular conjunction event, more certainty is needed for systems like those shown in Comparisons I, III, or V. Future conjunction campaigns will therefore benefit greatly from dedicated, multi-platform observations of large-scale convection flow—observations of comparable importance to in situ FAC measurements.

3.4.2 Electron Precipitation Spectra

As discussed in Section 3.2.7, the choice of precipitating electron energy spectra can affect the impact ionization rate at different altitudes; an unaccelerated Maxwellian profile, Equation 3.4, often carries an erroneous high-

energy tail which overestimates the E -region density enhancement from electron precipitation. Moreover, choosing to use unaccelerated Maxwellian spectra in inverting multi-spectral imagery results in a de facto source region characteristic energy equal to the accelerating potential drop, i.e. $T_s = U_a = E_0$. This is not unlike how a choice of $\bar{\mathbf{E}} = 0$ carries hidden assumptions about j_{\parallel} . With an accelerated Maxwellian profile, Equation 3.6, we estimate T_s prior to multi-spectral image inversion which allows for much “colder” source populations and, we argue, more geophysical precipitating electron modeling.

Below are two comparisons which look at how decoupling the source region characteristic energy from the auroral acceleration potential changes auroral current closure. See Table 3.2 for details on these comparisons and Table 3.1 for the (peak) values for Q_p , U_a , T_s , and E_0 .

Comparison VI: Precipitation Spectra

Returning back to the February 10 conjunction event from Comparison I, Figure 3.12 depicts Comparison VI which looks at the differences between Simulation VIa (also named Ia) with the accelerated precipitation spectra assumption given by $\phi_a(E)$ (first row), and Simulation VIb which assumes $\phi_u(E)$ instead (second row). The first feature to point out is the central, north-up electron density slices shown in panels a and c: simulation VIa has both precipitation arc induced density enhancements tucked above 100 km in altitude, while the use of $\phi_u(E)$ in Simulation VIb has these same two arcs increasing their electron density enhancements to the bottom of the simulation volume. This limits the closure paths of current flux tubes in Simulation VIa, compared to Simulation VIb.

Panels a and c show that all three current flux tubes are squished to higher altitudes in Simulation VIa, compared to Simulation VIb, forcing them to have a preference of Pedersen, over Hall, current closure. Panels b and d show how this affects the curvature of the flux tubes from a topside view. The red flux tube in Simulation VIa extends significantly further north given its preferred direction of that of the electric field, whereas the Simulation VIb red flux tube stays more parallel to the arc, traveling perpendicular to the electric field. Note that, despite the morphology being more along-arc, this flux tube does not extend much further east compared to the one in Simulation VIa, as it is able to capture higher upward FAC densities in this direction. Subsequently, its end region has a smaller overall area needed to capture 1.5 kA of upward FAC. Similar to the red flux tubes, the Simulation VIb orange current flux tube travels more often in the direction perpendicular to \mathbf{E} compared to its Simulation VIa tube, again because the flux tube is able to traverse lower altitudes.

Panels e – f show that, in this instance, the height-integrated Joule heat-

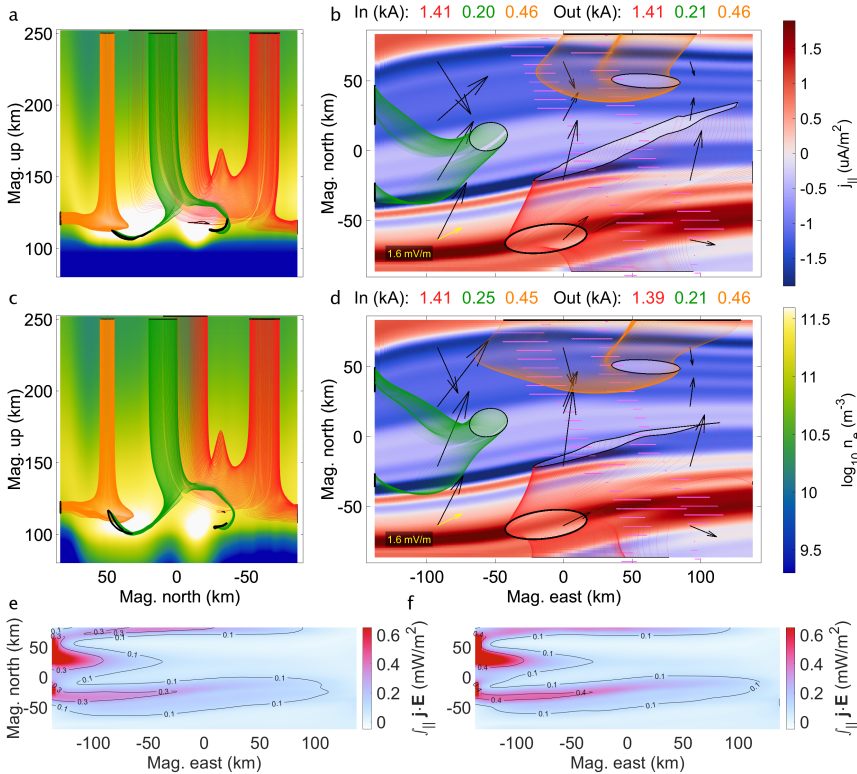


Figure 3.12: Comparison VI (February 10, 9:51 UT): Top and side views of Simulation VIa with accelerated Maxwellian electron precipitation (a, b) versus Simulation VIb with unaccelerated Maxwellian electron precipitation (c, d) along with height-integrated Joule heating for Simulation VIa (e) and VIb (f). For plot details, see Section 3.2.8. Data sources: Swarm (2025), SuperDARN (2025), and Simulations (2025).

ing increases by around 30% with the unaccelerated, over the accelerated, Maxwellian precipitation assumption. This can be counterintuitive when considering the Pedersen closure preference of Simulation VIa. Looking at panels b and d of Figure 3.12, however, tells us that the electric fields (black arrows) surrounding the arcs are higher in strength with the unaccelerated assumption which, evidently, is consistent with an increase in Joule heating. Ultimately, along with having the same FAC and background electric field drivers, both simulations have near identical maps of total precipitating electron energy, even though their imagery inversions assume two different spectral shapes. This implies that the altitudinal distribution of impact ionization alters the energy accounting, and thus the electric load characteristic of this auroral arc system.

Both Simulations VIa – b assume the relatively weak, SuperDARN derived $|\bar{\mathbf{E}}| = 1.6 \text{ mV/m}$, which makes them more susceptible to changes in the Hall closure layer as we have shown in Section 3.4.1. Adding to this susceptibility, the precipitation arcs have relatively high values of $U_a = 5.8$ and $E_0 = 4.2 \text{ keV}$ respectively. This deposits the impact ionization to lower altitudes, rendering the Hall layer more important still. This, along with the altered Joule heating, puts emphasis on the energy distribution shape of precipitating electrons in such auroral systems. Up next, we look at Comparison VIII whose simulations have both much stronger background electric fields and significantly higher total precipitation energy flux, which, along this line of reasoning, implies both Simulations VIIIA – b are less reliant on Hall closure in MI coupling.

Comparisons VIII: Precipitation Spectra

The precipitation arcs in Simulation VIIIA (also named IIIA) assume an acceleration potential peaking at around $U_a = 5.4$, and the characteristic energy for the arcs in Simulation VIIIB reach around $E_0 = 4.0 \text{ keV}$ —similar to the values from Comparison VI. However, with respect to Comparison VI, the simulations in Comparison VIII have more than three times the energy flux, $Q_p = 32.3 \text{ mW/m}^2$, background electric fields that are more than 13 times stronger, $|\bar{\mathbf{E}}| = 21.0 \text{ mV/m}$, and FAC sheets whose magnitudes around double, $|j_{\parallel}| = 3.8 - 4.5 \mu\text{A/m}^2$. Additionally, at $T_s = 800 \text{ eV}$, the source region characteristic energy for simulation VIIIA also nearly doubles that of Simulations VIa. Figure 3.13 shows how unaccelerated Maxwellian precipitation at these more energetic parameters compares to accelerated Maxwellian precipitation.

By proxy of the electrojet currents shown in panels g – h, the unaccelerated Maxwellian precipitation deposits ionization to both lower altitudes—around 6 km lower compared to Simulation VIIIA—and to a larger altitudinal range given the nearly four times higher energy spread of the unaccel-

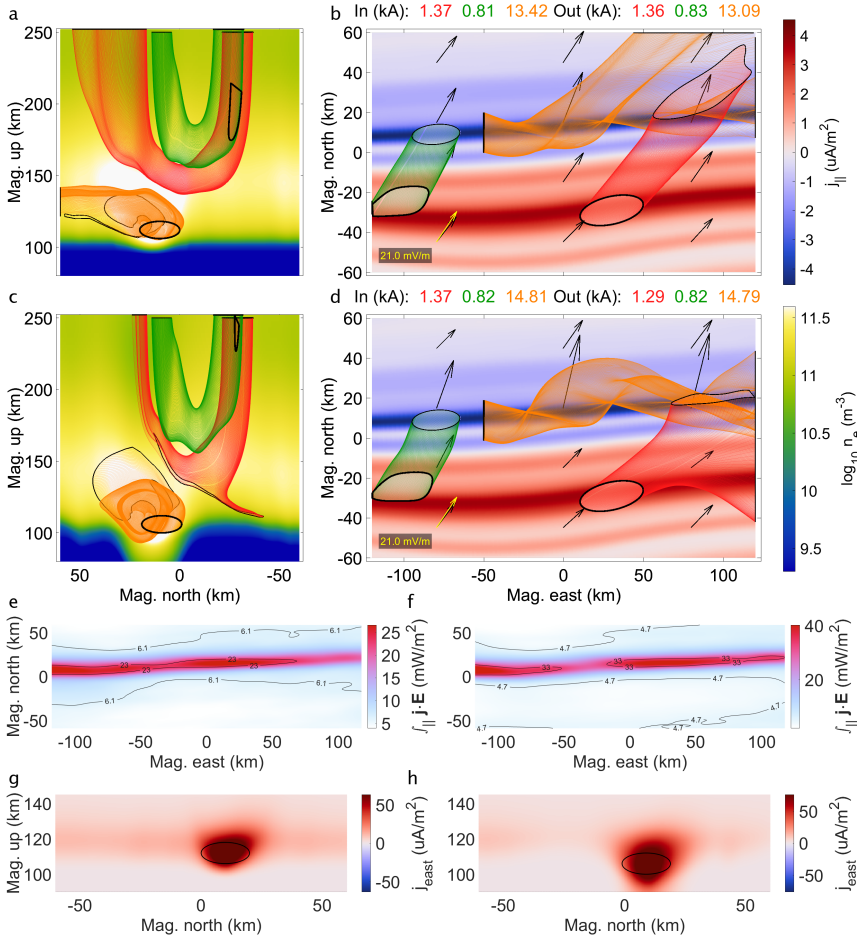


Figure 3.13: Comparison VIII (March 4, 7:30 UT): Top and side views of Simulation VIIa with accelerated Maxwellian electron precipitation (a, b) versus Simulation VIIb with unaccelerated Maxwellian electron precipitation (c, d) along with height-integrated Joule heating for Simulation VIIa (e) and VIIb (f). (g, h) North-up slices of the magnetic eastward current component for Simulations VIIa – b respectively taken at 50 km west from center with the start curves of their respective orange flux tubes (solid black). For plot details, see Section 3.2.8. Data sources: Swarm (2025), SuperDARN (2025), and Simulations (2025).

erated energy spectra. We focus on these electrojet currents by looking at both orange flux tubes, which capture similar values of 13.1 and 14.8 kA for Simulations VIIIa – b respectively. As before, the density volume resulting from the accelerated Maxwellian assumption is restricted to above around 100 km, forcing the respective orange tube to take on more Pedersen current. This means the electrojet in Simulation VIIIa veers to the northeast, directed toward the electric field (see panel b). The orange flux tube in Simulation VIIIb, being overall at lower altitudes, travels more easterly, staying relatively orthogonal to the electric field.

As shown in panels a – b, the red flux tube in Simulation VIIIa takes advantage of the energy deposition at higher altitudes and the large electric field strength, and finds closure through Pedersen alone. In Simulation VI-IIb, however, only around 0.7 of the 1.4 kA is able to connect with the FAC, while the remainder exists through the eastern boundary. Interestingly, the existence of the electrojet current in Simulation VIIIb appears to push the red flux tube away from the highest densities, subsequently squeezing it to lower altitudes. The green flux tube, having to travel a shorter horizontal distance compared to the other tubes, remains at altitudes where the $\phi_u(E)$ versus $\phi_a(E)$ assumption matters much less, and so it barely changes its morphology and amperage across the two simulations.

Panels e – f of Figure 3.13 show a band of enhanced Joule heating just equatorward of the precipitating arc in both simulations, yet Simulation VIIIa has this band peak at around 26.6 mW/m², while Simulation VIIIb peaks closer to 40.0 mW/m²—around a 50% increase. Between the two simulations, the Pedersen current density remains fairly similar; it is the significantly varying Hall current density that creates the different morphologies (see Figure 3.14, panels a – d). This points to the electric field strength; in Simulation VIIIa there is a band of enhanced across-arc electric field collocated with the Joule heating and peaks at around 20 mV/m, while the same is true for Simulation VIIIb except that it peaks around 40 mV/m (see panels e – f).

The band of precipitation enhanced Hall conductance for Simulations VIIIa – b peak at around 60 and 80 S respectively, as shown in panels g – h. Now, since their spatial morphology comes from the same imagery, it implies that this increase in peak value also increases $\nabla_{\perp}\Sigma_H$, enhancing its associated FAC contributions as per Equation 3.1. Panels i – j show that these contributions, in this case, are in the opposing direction with respect to the total FAC driver—the third term in Equation 3.1 creates an upward current sheet where the driver map expects a downward sheet, and vice-versa. Given that the second term, $\mathbf{E}\cdot\nabla_{\perp}\Sigma_P$, can only help balance this by increasing $|\mathbf{E}|$, it would do so equally to that third term, $(\mathbf{E}\times\mathbf{b})\cdot\nabla_{\perp}\Sigma_H$. This leaves the local polarization to help balance the FAC, as is evident in panels k – l of Figure 3.14. As before, all the input maps have nearly the

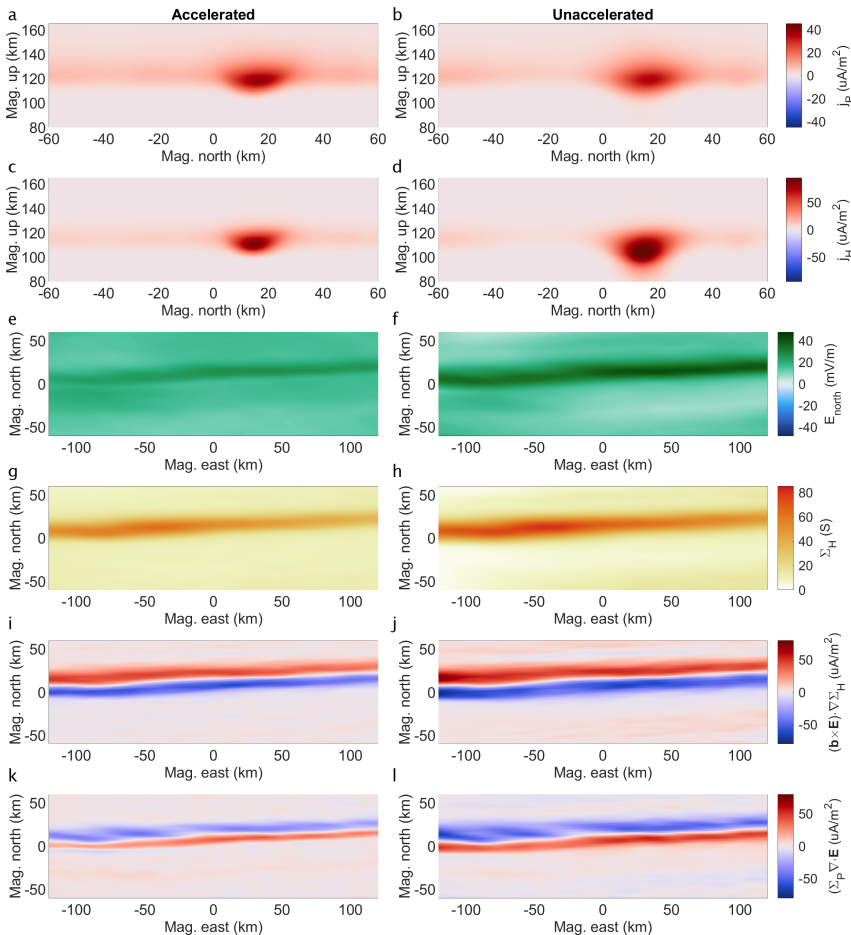


Figure 3.14: Factors that play a role in enhancing Joule heating for Simulation VIIb over VIIa. (a, b) Central up-north cuts of Pedersen current for Simulation VIIa – b. (c, d) Same for Hall current. (e, f) East-north plots of electric field's magnetic north component from Simulation VIIa – b. (g, h) Same for Hall conductance. (i, j) East-north plots of the third term in Equation 3.1 for Simulation VIIa – b. (k, l) Same for the first term in Equation 3.1. Data sources: Simulations (2025).

same spatial morphology for both simulations, hence, to increase $\nabla_{\perp} \cdot \mathbf{E}$, the simulation assuming an unaccelerated spectrum has a higher peak electric field, resulting in enhanced Joule heating despite the dissipationless Hall current enhancement.

In all, even though Simulations VIIa – b both have high total energy flux and strong electric field strengths, the large FAC requirements and the higher electron energy distribution peaks mean that these systems do touch on the Hall layer in their current closure. In contrast, Comparisons VII and IX (see Supporting Information, Appendix C) both pertain to auroral arc systems whose FAC requirements, precipitation energy fluxes, and energy distribution peaks are relatively low. These combinations of parameters, even in the case of a weaker electric field in Comparison IX, results in simulations whose assumption of electron energy distributions matter less in both current closure and Joule heating as a result of FAC source term balancing.

Summary: Precipitation Spectra

We have shown that, if a particular auroral arc system requires Hall currents for FAC closure, choosing unaccelerated Maxwellian energy spectra for precipitating electrons is too restrictive when attempting to best represent the resulting impact ionization. Decoupling the energy spread from the most probable energy allows the modeling of auroral arcs whose electrons are accelerated from much colder source regions compared to their acceleration potential. Even for relatively “hot” accelerated precipitation, such as that from Comparisons VIII and IX ($T_s = 800 - 860$ eV), the alternate, unaccelerated choice of $U_a = T_s = E_0$ still grossly overestimates the depth reached by the electron density enhancements. Holding FAC demands constant, this matters most when the average electric field strength is sufficiently weak, and/or the precipitation is low-reaching, i.e. any factor that puts emphasis on the Hall conductivity layer. Furthermore, unaccelerated Maxwellian electron distributions can overestimate the Hall currents as a whole, as well as the height-integrated Joule heating.

We have shown that specific assumptions of electron precipitation spectra can change the interpretation of auroral arc systems. Aptly, recent increases in the availability of multi-spectral, rather than white-light, all-sky imagery allows the community to move away from the assumption of unaccelerated Maxwellian precipitation spectra, and toward energy distributions which decouple the energy spread from the peak energy, allowing for more flexibility in modeling electron precipitation.

3.4.3 Along-Arc FAC Structure

Of our six conjunction events, two have a double-spacecraft arc crossing. This gives us an opportunity to look at two sensitivities: (1) how does along-arc structure in FAC affect current closure, and (2) how much confidence can be had in the replication technique we use. Our double replications have a weighting scale length of 50 km (roughly the distance between the orbits of Swarm A and C) when transitioning from replications of either track. This is described in more detail by van Irsel et al. (2024, Section 2.3). When performing a weighted replication with plasma flow data, this can result in arbitrary along-arc gradients which affect the first term in Equation 3.1. In our case, though the along-arc gradient in j_{\parallel} resulting from this weighting scale length is arbitrary, such gradients have less physical implication on the system as a whole. Following are comparisons between double versus single replications of our two double-spacecraft conjunction events.

Comparison X: Along-Arc FAC Structure

Comparison X looks at our February 10 conjunction event with Simulation Xa using a weighted replication of both Swarm A (east) and C (west), and Simulation Xb which uses a replication of Swarm A data only. Their orbits cut roughly through the center of the simulation volume at about 47 km apart, which allows us to look at current closure on either side of the tracks. Looking at Figure 3.15, panels b and d, reveals an up-down FAC sheet pair that exists in Simulation Xa, but not in Xb. From the western boundary, centered around 40 km south-from-center, a roughly -2 to 1 $\mu\text{A}/\text{m}^2$ FAC pair follows the arc boundary up until just past the Swarm C FAC data track, from which this signature is replicated. Furthermore, the southernmost downward FAC sheet narrows and intensifies, when transitioning from the Swarm A to C tracks, from about 25 km wide and 1 – 1.5 $\mu\text{A}/\text{m}^2$ in magnitude, to around 10 km and 2 $\mu\text{A}/\text{m}^2$. Simulation Xb has this FAC sheet remain unchanged along the arc.

With these differences in replicated FAC maps in mind, Simulation Xa (Figure 3.15a – b), though being the same as Simulation Ia, here shows a different set of current flux tubes. They are calculated (in reverse) from ellipses placed at the southernmost upward, precipitating current sheet located east of, west of, and in between the two FAC data tracks. This helps illustrate the affect on current closure resulting from the difference between the two data tracks. Figure 3.15c – d (Simulation Xb) shows flux tubes that are calculated from the same three ellipses.

The orange flux tube (0.5 kA) lies almost entirely east of the Swarm A track, hence it remains mostly unchanged, both in morphology and quantity. The green flux tube, however, is encroaching on the aforementioned Swarm C replicated FAC pair and thus captures around 0.1 kA more in

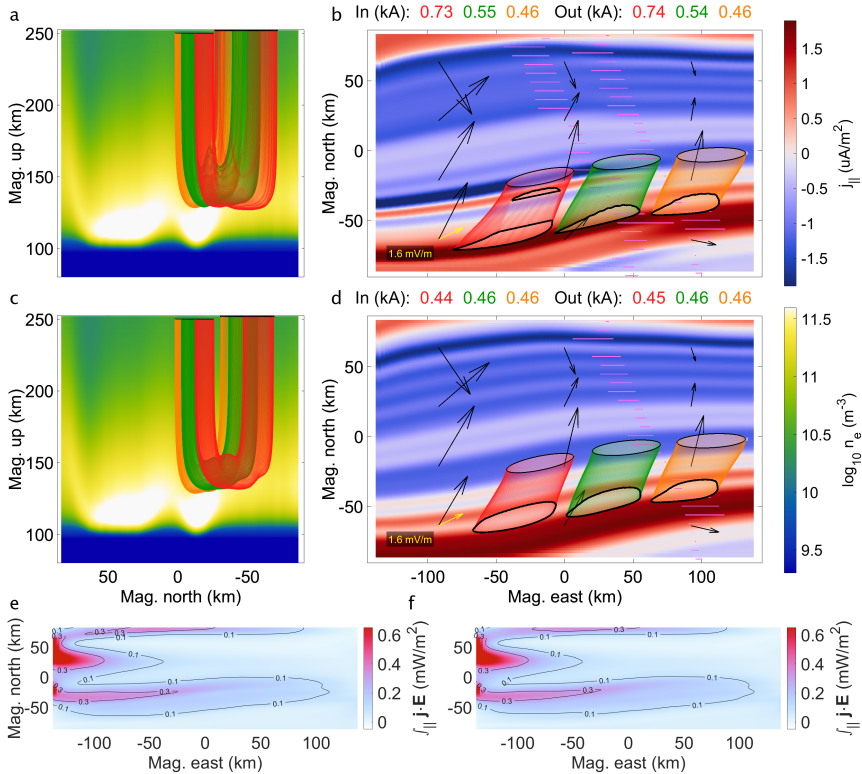


Figure 3.15: Comparison X (February 10, 9:51 UT): Top and side views of Simulation Xa with a FAC replication using both Swarm A (east) and C (west) (a, b) versus Simulation Xb with a FAC replication using only Swarm A (c, d) along with height-integrated Joule heating for Simulation Xa (e) and Xb (f). For plot details, see Section 3.2.8. Data sources: Swarm (2025), SuperDARN (2025), and Simulations (2025).

Simulation Xb. The electric field across the arc has the flux tubes directed southwest to northeast, such that the green flux tube has its influx end entirely on the western side of Swarm C. Here, the Simulation Xa downward current sheet is stronger, but less than half the width compared to its Simulation Xb counterpart. The steeper FAC across-arc gradient in Simulation Xa pinches the downward green flux tube end into a teardrop shape (at roughly 25 km east and 50 km south), while its higher FAC density aids in capturing that additional 0.1 kA.

The red flux tube lies completely on the western side of Swarm C and captures the upward part of the FAC sheet pair introduced by Swarm C. At 0.7 kA, this gives it an additional 0.3 kA over the red flux tube in Simulation Xb. The adjacent downward current sheet helps close 0.1 kA of this added current, while the remainder is closed with a similar teardrop shaped flux tube end.

Comparison X outlines how a double versus a single FAC data track replication can introduce, albeit relatively minor, FAC signatures in the along-arc direction. We have to assume such signatures can appear and disappear over distances on the order of 50 km in every FAC replication. The major FAC structure, however, is conserved, suggesting the replication methodology holds.

Comparison XI: Along-Arc FAC Structure

Because of limitations of the all-sky imagery of the March 14 conjunction event, the simulation region for Comparison XI is almost completely west of both Swarm tracks. This prevents us from sourcing current flux tubes on either side of the data tracks, however we can still use Comparison XI to provide insight into what confidence can be had in the replication technique, and deliberate about the extent to which auroral arc FAC varies in the along-arc direction.

Panels a – b in Figure 3.16 show results from Simulation XIa, which is driven by a FAC map replicated from both Swarm A and C data. However, given the locations of the data tracks, most of this replication uses data from Swarm C, as it is the closest to the simulation region. With Simulation XIb (panels c – d) using only Swarm A in its FAC replication, this is essentially a Swarm A versus Swarm C comparison.

In contrast to Comparison X, here we see two FAC replications that, though varying somewhat, are structurally very similar. The southernmost return current sheets for both Simulations XIa – b are similar in strength, width, and location, as is shown by the red flux tubes who capture around 1.2 kA in the same place for both simulations. The return current sheet just above, captured by the green flux tubes, is around half as strong in Simulation XIb and positioned \sim 7 km southward, and the orange flux tubes

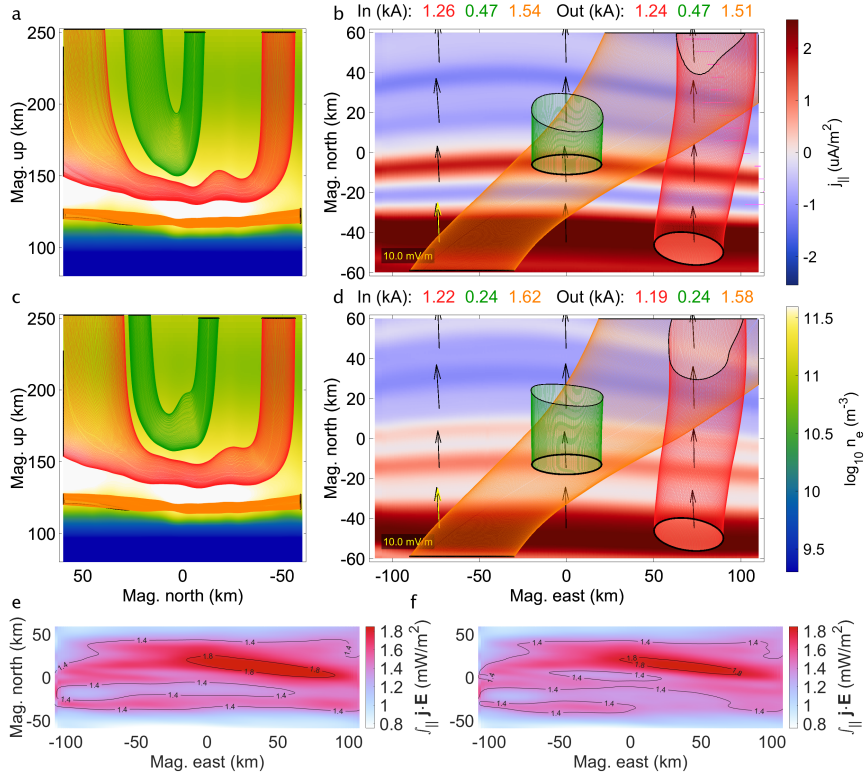


Figure 3.16: Comparison XI (March 14, 6:49 UT): Top and side views of Simulation XIa with a FAC replication using both Swarm A (east) and C (west) (a, b) versus Simulation XIb with a FAC replication using only Swarm A (c, d) along with height-integrated Joule heating for Simulation XIa (e) and XIb (f). For plot details, see Section 3.2.8. Data sources: Swarm (2025), SuperDARN (2025), and Simulations (2025).

carry a similar $1.5 - 1.6$ kA of Hall current at nearly the same location in both simulations. Overall, Comparison XI provides support for the extrapolation of FAC data over a distance of around 50 km, up to the differences in auroral arc simulations seen here.

Summary: Along-Arc FAC Structure

Two of our six conjunction events benefit from being able to use a second data track in their replications and subsequent simulations. Comparisons X and XI show to what extent the FAC map can change in just under 50 km, providing important insight into the confidence of all of our FAC replications, and consequently the resulting 3-D simulations of these auroral arc systems. Overall, contingent on the morphology indicated by the imagery and aside from minor FAC signatures, replicating the FAC data using arc boundaries defined by auroral imagery is a justifiable method for creating 2-D, continuous driver maps for 3-D simulations of auroral arc systems.

3.5 Discussions & Conclusions

Current closure morphology and Joule heating from resulting closure currents are two important aspects of ionospheric physics, particularly surrounding discrete auroral arc systems. By carefully incorporating observational data from multi-instrument conjunctions into input drivers of auroral arc simulations, we point out three aspects that the results are susceptible to: (1) the along-arc structure in FAC and the arc-boundary replication technique, (2) the constant background flow, and (3) the specifics of electron precipitation. Here, we conclude our findings and discuss possible future studies that can advance from this work.

Auroral arc systems should be studied in three dimensions to fully understand field-aligned current closure and, by extension, Magnetosphere-Ionosphere-Thermosphere coupling. We show, using several permutations of 3-D, electrostatic, data-driven, auroral arc simulations across six conjunction events, that flux tubes of electric current navigate around one another in their closure paths; something they cannot do in height-integrated (east, north), or cross-arc (north-up) two-dimensional descriptions. These current flux tubes tell the story of how FAC, ionospheric electric fields, and Pedersen and Hall conductivities interplay in a cohesive, self-consistent manner, and they do so with more detail than 2-D descriptions allow.

To produce top-boundary driver maps for our simulations, we demonstrate the use of auroral-imagery-guided FAC replication, similar to methods outlined by Clayton et al. (2019); van Irsel et al. (2024). We show that this method can produce FAC maps that are geophysically consistent with maps of precipitation energetics, and that hold reasonably well for major

arc-scale FAC structure. However, more minor FAC structure may appear or disappear when moving in the along-arc direction over distances on the order of 50 km. Even so, this methodology uses maximal information from imagery derived precipitation maps to provide geophysically meaningful extrapolations of FAC surrounding auroral arcs.

The 3-D auroral arc simulations covered in this paper have been shown to be very sensitive to both the magnitude and the direction of the constant, large-scale, background electric field, $\bar{\mathbf{E}}$. Equation 3.2 shows what the choice of $\bar{\mathbf{E}}$ implies about the 2-D top-boundary FAC driver map, and thus, how the simulations interpret these maps. We draw the following conclusions about how $\bar{\mathbf{E}}$, in the absence of neutral winds, affects discrete auroral arc systems:

- Strong background convection fields can render the use of Hall currents in FAC closure negligible, while weak background convection fields put emphasis on both local polarization fields and FAC closure through the electrojet.
- Across-arc electric fields provide shorter closure paths making FAC close through Pedersen current more often.
- FAC sheets close with adjacent ones only in the direction of the electric field.
- When part of the electric field is directed along the arc, it lengthens the closure paths and, as current flux tubes cannot intersect, it pushes additional tubes to Hall current altitudes.
- The manner in which the background electric field affects current connectivity, along with the electric field itself, significantly alters Joule heating, and thus the electrostatic load characteristics, of auroral arc systems.

These conclusions support the idea that large-scale convection flow conditions are a dominant driver of the specific morphology of auroral arc systems, with which the arc-scale ionosphere perturbs \mathbf{E} in accordance with a 3-D conductivity volume.

In addition to background convection fields, auroral arc systems are also sensitive to the specifics of precipitating electron energy distributions. We show that the use of unaccelerated Maxwellian spectra can erroneously enhance impact ionization at lower altitudes, resulting in an overestimation of E -region densities. We compare the use of such spectra against accelerated Maxwellian spectra, which decouple the peak energy from the energy spread. Even for simulations whose source region characteristic energy is

estimated to be relatively large, $T_s \sim 800$ eV, the unaccelerated assumption still greatly overestimates density enhancements at lower altitudes. We show the following:

- The availability of multi-spectral, rather than white-light, all-sky imagery allows the community to move away from the assumption of unaccelerated Maxwellian precipitation spectra, and toward energy distributions which decouple the energy spread from the peak energy, allowing for more flexibility in modeling electron precipitation.
- The choice of accelerated versus unaccelerated Maxwellian electron precipitation most affects FAC closure in auroral arc systems when the Hall currents play a considerable role in this closure.
- Keeping FAC and total precipitating electron energy drivers constant, the choice of unaccelerated over accelerated precipitation alone can increase the calculated height-integrated Joule heating by 30 – 50% in some auroral arc systems.
- Unaccelerated Maxwellian auroral precipitation assumptions are able to greatly enhance electrojet currents compared to accelerated precipitation assumptions.

This work looks at how to determine geophysical, self-consistent solutions to current continuity in auroral arc systems, and what these systems are sensitive to, thus uncovering how important various parameters can be. How then do we know which solution is correct? The existence of TII ion drift data (or other, independent flow data) from the Swarm spacecraft invites comparisons to the calculated GEMINI output flow maps covered in this paper. Figure 3.17 shows two such comparisons of the magnetic eastward TII flow (assuming no along-track component) across the model space for two of the simulations (Ib and IVb). While we have generated 17 simulations of the six events in Table 3.1, only the February 10 and March 14 conjunctions include Swarm A TII data; only the former has the crossing directly within the model space. The simulations using PFISR for the background flow for these two cases match better than the corresponding SuperDARN runs, which have smaller background flows.

It is notable among the examples chosen for this study (the six events in Table 3.1) that there is not a particularly strong correlation between the magnetic and electric field signatures in the raw Swarm data—for most of these events, the $\nabla \cdot \mathbf{E}$ term in Equation 3.1 is apparently not the major player for the events in Table 3.1. Thus this comparison with TII becomes mostly a question of matching the background flow to the TII value, perhaps why the nearer source (PFISR) provides the closest match. For the first example shown, there are some $\nabla \cdot \mathbf{E}$ signatures in both TII and the

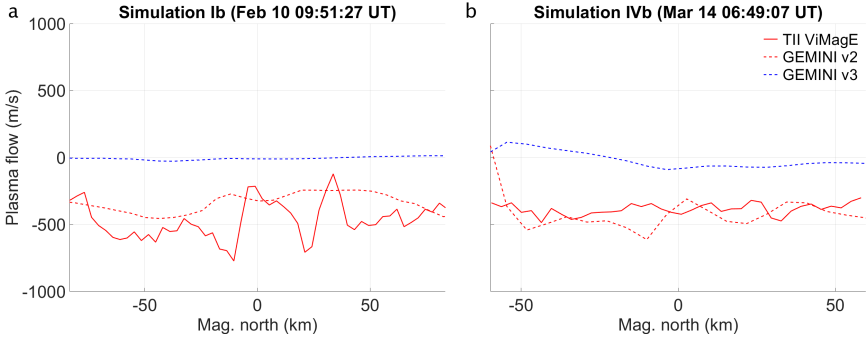


Figure 3.17: GEMINI versus TII flow comparisons for Simulations Ib (a) and IVb (b). The GEMINI magnetic eastward, “v2”, and northward, “v3”, plasma flows are interpolated through the simulation volume at the Swarm A tracks. TII magnetic eastward ion drift data, “ViMagE”, are converted to geomagnetic coordinates assuming no along-track component. Both simulations use PFISR derived background flow, accelerated Maxwellian precipitation, and double-spacecraft replications. Data sources: Swarm (2025), PFISR (2025), and Simulations (2025).

GEMINI results, but the GEMINI result is somewhat smoother and slightly offset. Both of these differences may well be artifacts of the image inversion process.

Finally we can consider whether the competition between the $\nabla \cdot \mathbf{E}$ and $\nabla \Sigma_{P,H}$ terms in Equation 3.1 provides a truly unique solution to the problem posed. There is a strong dependence on the chosen $\bar{\mathbf{E}}$: choosing the background electric field differently finds different situations. There may be choices, beyond what PFISR and SuperDARN provide, which more closely track the TII cross-track flow values. We do see that choosing different background flows, e.g. the no-background flow run versus the large-background flow simulations in Comparison III, generates in the GEMINI result a visible $\nabla \cdot \mathbf{E}$ signature which is masked when the imposed background electric field is strengthened. Future work exploring these comparisons with TII should include (a) events like the one covered by Clayton et al. (2021), with its strong $\nabla \cdot \mathbf{E}$ signature; and (b) further study of error sources stemming from matching the spacecraft data to inverted imagery, particularly for oblique camera angles which tend to blur and misplace discrete arc structures. We also note the scale of smoothing applied for these runs, as described in Subsections 3.2.1 and 3.2.2: this level of smoothing may yet be hiding relevant physics, particularly at sharp arc edge boundaries.

The tools developed herein provide a means for data-driven event case

study simulations to be routinely done, assuming sufficient data coverage. Upcoming iterations may consider different, incomplete combinations of input and/or adaptation of our methods into a formal physics-based assimilation scheme. A subject for further studies is the relevant physical gradient limit caused by recombination and collisions in the current closure altitude region: how sharp of gradients can be sustained and be relevant?

In the collective effort to try and understand the nature of aurorae, the instruments that provide our observational data are an ever-existing limitation. It would be optimal to deploy 1000s of spacecraft, radars, and imagers across the northern and southern auroral ovals (Nykyri et al., 2025), but this is impractical. Hence, measurements must be targeted and focused on parameters that are most influential to the physics at hand. This work provides three such aspects to contribute to this focus and aids in making decisions as to what is important and when.

Open Research

All 3-D simulation data, imagery inversions, and supporting metadata are available at <https://rcweb.dartmouth.edu/lynchk>. The data for the Poker Flat DASC are available at <http://optics.gi.alaska.edu/optics/archive>, for AMISR at <https://data.amisr.com/database>, for SuperDARN at <https://superdarn.ca/data-download>, and for Swarm at <https://swarm-diss.eo.esa.int>. The GEMINI source code and documentation is available at <https://github.com/gemini3d> and the replication/visualization tools at https://github.com/317Lab/aurora_gemini.

Acknowledgments

We thank NASA for funding Jules van Irsel from Grant 80NSSC23K1622 through the FINESST program and Dartmouth College for providing internal funding for Phase A of the Auroral Reconstruction CubeSwarm proposal from which a lot of this research stems, and we acknowledge NASA Grant 80GSFC21C0009 for the ARCS MIDEX CSR funding. AMISR facilities, including PFISR, are operated and maintained for the US National Science Foundation (NSF) by SRI International under a cooperative agreement #AGS-1840962. AMISR data are produced and made publicly available for scientific and academic research purposes under the same award. This work uses version 0302, level 1B data from the Thermal Ion Imagers and version 0401, level 2 FAC data made possible by the European Space Agency's Swarm Data, Innovation, and Science Cluster and Canadian Space Agency grant 15 SUSWARM. We thank NASA for providing funding for the GEMINI model development from Grant 80NSSC24K0126. 3-D simulations supporting this work were facilitated by the Discovery cluster at Dartmouth Research Computing and the NASA High-End Computing (HEC) Program through the NASA Advanced Supercomputing (NAS) Division at Ames Research Center. The authors acknowledge the use of SuperDARN data and thank Daniel Billett for collecting SuperDARN convection flow data for use in this paper. SuperDARN is a collection of radars funded by national scientific funding agencies of Australia, Canada, China, France, Italy, Japan, Norway, South Africa, United Kingdom and the United States of America. We thank Michael Hirsch, Terry Kovacs, and John Griffin for GEMINI and computational technical support.

Chapter 4

Conclusion Summary & Future Work

4.1 Conclusion Summary

The conclusions from Chapter 2 and 3 encompass the main takeaways from this thesis. To avoid redundancy, they are summarized here verbatim from Sections 2.5 and 3.5. Relevant figures and the Section 1.4 science question(s) they address, denoted with SQ #, are given for reference.

- Even for the most basic auroral arc systems, a 1-D or 2-D description can be insufficient and may hide the 3-D nature of current closure. (SQ 2)
- When extrapolating ionospheric topside plasma flow data surrounding auroral arcs, it is important to scale the data in a way that co-locates the associated shorted-out electric fields with the region of enhanced conductance. (SQ 1, Figures 2.4 & 2.10)
- Similarly, it is important to rotate the plasma flow data in a way that avoids introducing arbitrary angles between the ionospheric electric field and the conductance gradients. (SQ 1, Figures 2.4 & 2.10)
- Current flux tubes whose ends are near the FAC inflection line between an upward and downward current sheet can close through Pedersen current at altitudes well above where Pedersen conductivity maximizes. (SQ 2, Figure 2.9)
- Current flux tubes surrounding auroral arcs can split; a region of FAC inside one downward current sheet can close in two upward current sheets. (SQ 2 – 3, Figure 2.9)

- Strong background convection fields can render the use of Hall currents in FAC closure negligible, while weak background convection fields put emphasis on both local polarization fields and FAC closure through the electrojet. (SQ 1 – 3, Figures 3.8 & 3.9)
- Across-arc electric fields provide shorter closure paths making FAC close through Pedersen current more often. (SQ 1 – 3, Figure 3.8)
- FAC sheets close with adjacent ones only in the direction of the electric field. (SQ 2 – 3, Figure 3.11)
- When part of the electric field is directed along the arc, it lengthens the closure paths and, as current flux tubes cannot intersect, it pushes additional tubes to Hall current altitudes. (SQ 1 – 3, Figure 3.9)
- The manner in which the background electric field affects current connectivity, along with the electric field itself, significantly alters Joule heating, and thus the electrostatic load characteristics, of auroral arc systems. (SQ 1, Figures 3.8 – 3.11)
- The availability of multi-spectral, rather than white-light, all-sky imagery allows the community to move away from the assumption of unaccelerated Maxwellian precipitation spectra, and toward energy distributions which decouple the energy spread from the peak energy, allowing for more flexibility in modeling electron precipitation. (SQ 1 – 2, Figure Figures 3.12 – 3.13)
- The choice of accelerated versus unaccelerated Maxwellian electron precipitation most affects FAC closure in auroral arc systems when the Hall currents play a considerable role in this closure. (SQ 1 – 2, Figures 3.12 – 3.13)
- Keeping FAC and total precipitating electron energy drivers constant, the choice of unaccelerated over accelerated precipitation alone can increase the calculated height-integrated Joule heating by 30 – 50% in some auroral arc systems. (SQ 1, Figure 3.13)
- Unaccelerated Maxwellian auroral precipitation assumptions are able to greatly enhance electrojet currents compared to accelerated precipitation assumptions. (SQ 1 – 2, Figure 3.13)

These conclusions encapsulate the major findings of this work and aim to answer the science questions raised in Section 1.4. In addition to this, major scientific objectives are attained in (1) the development of a public catalog of data-driven auroral arc system simulations found at <https://rcweb.dartmouth.edu/LynchK/Gemini3D>, and (2) the formalization of the tools,

techniques, and methods used in this work found at https://github.com/317Lab/aurora_gemini. A high-level overview of this collection in this repository can be found in Appendix B.

4.2 Future Work

All the simulations presented in this work have fully static drivers. This provides an excellent basis for the understanding of discrete auroral arc systems, but the auroral forms studied in this thesis often pertain to the substorm growth phase, which can provide the system drivers with an equatorward drift of 70 – 170 m/s (Karlsson et al., 2020, and references therein). Such drifting motion can provide ionization hysteresis because of recombination and chemistry time scales. It is therefore an appropriate topic of a study that can build from this work with relative ease. Furthermore, adding time dependence to the electromagnetic fields allows for a study of Alfvénic signatures—studies for which the simulations used in this thesis can be a basis as well.

The ionospheric model used to simulate discrete aurorae in this work, GEMINI, is undergoing major improvements at the time of writing (Zettergren et al., 2024). One such improvement includes adaptive mesh refinement (AMR) which allows for simulations that focus their computational energy on regions of interest. It does so by refining the simulation cell sizes in accordance with local gradients which, as discussed throughout this thesis, is vitally important in the understanding of auroral current closures. This is a welcome change in that it directly reduces the limiting operational scale-sizes. Mesh refinement also drastically reduces computation times allowing for more efficient, and by extension a higher number of, iterations of simulations targeting sensitivity studies like those presented in this work.

A second major improvement is the introduction of inter-model communication between GEMINI, or rather the AMR version trees-GEMINI, and the Model for Acoustic and Gravity wave Interactions in a Compressible atmosphere (MAGIC, Snively and Pasko, 2008) Forest—a neutral atmosphere model—which will transfer information about neutral density, flow, and temperature perturbations. This allows for the study of neutral wind effects to auroral current closure and Joule heating and vice versa, and, importantly, provides a means for avenues where a passive ionospheric load becomes an active, current generating auroral ionosphere through neutral wind dynamos.

Prior to the actualization of these improvements, various implementations of neutral wind effects can be used to perform auroral arc system studies that are inside current generating ionospheres. For example, the empirical statistical neutral wind model called the Horizontal Wind Model (HWM, Drob et al., 2015, & references therein) is already integrated into

GEMINI and can show preliminary results of studying the importance of neutral winds to auroral current closure. For a data-driven approach, one can use Scanning Doppler Imagers (SDI, Dhadly and Conde, 2016) to input thermospheric wind measurements into GEMINI. The improved multi-spectral imagery inversion approach used in this thesis can be applied to the methodology in deriving neutral winds with SDIs for providing better altitudinal accuracy.

Aside from improvements to methodologies, this work sets the stage for more studies using campaigns of multi-platform, heterogeneous measurement conjunctions, like Swarm-over-Poker-2023. E.g. the recently launched Electrojet Zeeman Imaging Explorer (EZIE, Madelaire et al., 2023) mission provides an excellent opportunity for facilitating conjunctions with radars, all-sky imagers, sounding rockets, and perhaps more. Furthermore, measurements of the Hall current, such as by EZIE, can provide means of validation for the 3-D current closure morphologies. In addition to campaigns, the upcoming twin sounding rocket mission, the Geophysical Non-Equilibrium Ionospheric System Science (GNEISS, Lynch et al., 2024a) mission, directly aims to address an event study investigating further unanswered mysteries of auroral system science. It does so by using maximal relevant auroral measurements that are fully coincident to be input in GEMINI for interpretation.

The work is far from done. The aurorae are too beautiful to ignore, which makes studying them delightful. So it would be remiss to not take advantage of them fully in our journey to understand this Earth and other similarly illuminating planets. It is the goal of this thesis to help unravel the geophysical system surrounding quiet discrete auroral arcs, yet this only a part of a much larger goal: to understand the system—the currents, the electric fields, the charged particles raining down—to such an extent that one only has to look at the auroral emissions—the most abundant of all auroral measurements—and get the whole picture. In short, we want to be able to *read the aurorae*.

Appendix A

Derivations

A.1 Most General Two-Variable Polynomial Harmonic Function

This appendix is almost verbatim, with minor formatting and stylistic modifications, Appendix A in the manuscript covered by Chapter 2. The author contributions are that of this same manuscript.

To show Equation 2.21 is the most general case, we take the complex polynomial of degree m ,

$$p(z) = \sum_{n=0}^m F_n z^n, \text{ where } z^n = (x + iy)^n = \sum_{q'=0}^n \binom{n}{q'} x^{q'} (iy)^{n-q'}, \quad (\text{A.1})$$

and recognize that the homogeneous polynomial z^n is analytic which therefore has harmonic real and imaginary parts (Ahlfors, 1953). This gives two parameters, the real and imaginary parts of F_n , for each value of n . To show uniqueness, we recognize that the Laplacian maps homogeneous polynomials of degree n to those of degree $n-2$, the domain and image of which have dimensions n and $n-2$ respectively. By the rank-nullity theorem, this means the dimension of the kernel of the Laplacian is $n - (n-2) = 2$, so we have found all solutions.

A.2 Derivation of Accelerated Bi-Maxwellian Differential Number Flux

This appendix is almost verbatim, with minor formatting and stylistic modifications, Appendix A in the manuscript covered by Chapter 3. The author contributions are that

of this same manuscript.

In order to implement the impact ionization calculations by Fang et al. (2010), we need the differential (as a function of energy) hemispherical number flux, i.e. electrons/eV/s/cm², of precipitating energetic auroral electrons at the topside of the ionosphere for every latitude-longitude pair. To derive this flux for an accelerated population we start with a bi-Maxwellian source at the plasmashell as is done by Fridman and Lemaire (1980):

$$g_s(v_{\parallel,s}, v_{\perp,s}, \varphi) dv = n_{e,s} \left(\frac{m_e}{2\pi} \right)^{3/2} \frac{1}{E_{\parallel,s}^{1/2} E_{\perp,s}} \times \exp \left[-\frac{m_e v_{\parallel,s}^2}{2E_{\parallel,s}} - \frac{m_e v_{\perp,s}^2}{2E_{\perp,s}} \right] v_{\perp,s} dv_{\parallel} dv_{\perp} d\varphi, \quad (\text{A.2})$$

where $n_{e,s}$ is the source region electron density, m_e is the mass of an electron, $E_{\parallel,s}$ and $E_{\perp,s}$ are the parallel and perpendicular characteristic energies, $v_{\parallel,s}$ and $v_{\perp,s}$ are the source region parallel and perpendicular speeds, and φ is the azimuthal coordinate. As electrons precipitate down towards the ionosphere they undergo no collisions—their velocities change in two ways only (Knight, 1973; Fridman and Lemaire, 1980; Kaepller, 2013):

1. The conservation of the first adiabatic invariant, i.e. the mirror force, increases their perpendicular velocity:

$$v_{\perp,s} = \frac{1}{\sqrt{\beta}} v_{\perp,i}, \quad (\text{A.3})$$

where $\beta = B_i/B_s > 1$, and B_i and B_s are the ionospheric and source region magnetic field strengths.

2. The conservation of energy increases the square magnitude speed as they fall through the parallel potential difference, U_a :

$$v_{\parallel,i}^2 + v_{\perp,i}^2 = v_{\parallel,s}^2 + v_{\perp,s}^2 + \frac{2U_a}{m_e}. \quad (\text{A.4})$$

This provides the parallel source region speed as a function of the ionospheric coordinates:

$$v_{\parallel,s} = \pm \sqrt{v_{\parallel,i}^2 + v_{\perp,i}^2 \frac{\beta - 1}{\beta} - \frac{2U_a}{m_e}}. \quad (\text{A.5})$$

From here, we use Liouville's theorem which tells us that, along a well-defined path through phase space, e.g. $(\mathbf{x}, \mathbf{v})_s \rightarrow (\mathbf{x}, \mathbf{v})_i$, the phase space density is held constant such that

$$g_i(\mathbf{x}_i, \mathbf{v}_i) = g_s(\mathbf{x}_s, \mathbf{v}_s). \quad (\text{A.6})$$

A good assumption is to say that we may separate spatial and velocity coordinates, $g(\mathbf{x}, \mathbf{v}) = n(\mathbf{x})f(\mathbf{v})$, and that locally the densities are constants, i.e. $n_i(\mathbf{x}) = n_{e,i}$, $n_s(\mathbf{x}) = n_{e,s}$. This tells us

$$g_i(\mathbf{v}_i) = g_s(\mathbf{v}_s) = g_s(\mathbf{v}_s(\mathbf{v}_i)), \quad (\text{A.7})$$

such that

$$\begin{aligned} g_i(v_{\parallel,i}, v_{\perp,i})dv^2 &= n_{e,s} \frac{m_e^{3/2}/\sqrt{2\pi}}{E_{\parallel,s}^{1/2} E_{\perp,s}} \\ &\times \exp \left[-\frac{m_e \left(v_{\parallel,i}^2 + v_{\perp,i}^2 \frac{\beta-1}{\beta} - \frac{2U_a}{m_e} \right)}{2E_{\parallel,s}} - \frac{m_e v_{\perp,i}^2 / \beta}{2E_{\perp,s}} \right] \frac{v_{\perp,i}}{\sqrt{\beta}} dv_{\parallel} dv_{\perp} \end{aligned} \quad (\text{A.8})$$

where we've integrated over φ . The ionospheric density is thus

$$n_{e,i} = n_{e,s} \frac{E_{\parallel,s} \sqrt{\beta}}{E_{\parallel,s} + E_{\perp,s}(\beta-1)} \exp \left[\frac{U_a}{E_{\parallel,s}} \right]. \quad (\text{A.9})$$

Note that $U_a \rightarrow 0$ and $E_{\parallel,s} \rightarrow E_{\perp,s}$ gives a familiar density relation: $n_{e,i} = n_{e,s}/\sqrt{\beta}$. Now that we have the velocity distribution function at the ionosphere, we find the differential number flux using $J_{\parallel,i}(\mathbf{v}_i)d^3v = v_{\parallel,i}g_i(\mathbf{v}_i)d^3v$ and then we perform the following change of coordinates:

$$v_{\parallel,i} = v \cos \theta = \sqrt{2E/m_e} \cos \theta \text{ and } v_{\perp,i} = v \sin \theta = \sqrt{2E/m_e} \sin \theta, \quad (\text{A.10})$$

with θ being the pitch angle, and with Jacobian determinant $1/m_e$. The energy, E , has the condition

$$E = \frac{m_e}{2} \left(v_{\parallel,i}^2 + v_{\perp,i}^2 \right) \geq U_a, \quad (\text{A.11})$$

as per Equation A.4. This gives

$$\begin{aligned} J_{\parallel,i}(E, \theta)dEd\theta &= \frac{n_{e,s}}{\sqrt{m_e}} \frac{1}{E_{\parallel,s}^{1/2} E_{\perp,s}} \frac{\sin 2\theta}{\sqrt{2\pi\beta}} E \\ &\times \exp \left[-\frac{E - U_a}{E_{\parallel,s}} - \left(\frac{E}{E_{\perp,s}} - \frac{E}{E_{\parallel,s}} \right) \frac{\sin^2 \theta}{\beta} \right] dEd\theta. \end{aligned} \quad (\text{A.12})$$

With unit-less parameters $\varepsilon \equiv E/E_{\parallel,s}$, $u_a \equiv U_a/E_{\parallel,s}$, and $\delta \equiv E_{\perp,s}/E_{\parallel,s}$, we get

$$\begin{aligned} \frac{1}{n_{e,s}} \sqrt{\frac{m_e}{E_{\parallel,s}}} J_{\parallel,i}(E, \theta)dEd\theta &= \frac{\sin 2\theta}{\sqrt{2\pi\beta}} \frac{\varepsilon}{\delta} \\ &\times \exp \left[-(\varepsilon - u_a) - \left(\frac{\varepsilon}{\delta} - \varepsilon \right) \frac{\sin^2 \theta}{\beta} \right] d\varepsilon d\theta. \end{aligned} \quad (\text{A.13})$$

We now integrate over $v_{\parallel,i} > 0$, i.e. $0 \leq \theta \leq \pi/2$, and find the hemispherical differential number flux.

$$J_{\parallel,i}(\varepsilon) d\varepsilon = n_{e,s} \sqrt{\frac{E_{\parallel,s}}{m_e}} \frac{1}{\delta \sqrt{2\pi\beta}} G\left(\frac{\delta-1}{\delta\beta}\varepsilon\right) \varepsilon e^{-\varepsilon+u_a} d\varepsilon, \quad (\text{A.14})$$

where $G(x) \equiv (e^x - 1)/x$. For similar parallel and perpendicular source temperatures, we have $\delta \sim 1$, and we have $\beta \sim 10^3$ for a plasmashell source region (Fridman and Lemaire, 1980), where $G(x \ll 1) \rightarrow 1 + x/2 + \mathcal{O}(x^2)$ such that

$$J_{\parallel,i}(\varepsilon) d\varepsilon \approx n_{e,s} \sqrt{\frac{E_{\parallel,s}}{m_e}} \frac{1}{\delta \sqrt{2\pi\beta}} \left(1 + \frac{\delta-1}{2\delta\beta}\varepsilon\right) \varepsilon e^{-\varepsilon+u_a} d\varepsilon \quad (\text{A.15})$$

If we re-cast this in terms of normalized total precipitating energy flux, $q_p \equiv Q_p/E_{\parallel,s}$, where

$$q_p = \int_{u_a}^{\infty} \varepsilon J_{\parallel,i}(\varepsilon) d\varepsilon, \quad (\text{A.16})$$

we get

$$J_{\parallel,i}(\varepsilon) d\varepsilon = q_p \frac{1 + \chi\varepsilon}{2 + 6\chi + u_a(2 + u_a + (6 + u_a(3 + u_a))\chi)} \varepsilon e^{-\varepsilon+u_a} d\varepsilon, \quad (\text{A.17})$$

where $\chi \equiv (\delta-1)/(2\delta\beta)$. We note that in our regime of $\beta \sim 10^3$ we may ignore the temperature difference at the source, so if we take the limit of $\delta \rightarrow 1$ we get a familiar result

$$J_{\parallel,i}(E) dE = \frac{Q_p}{T_s^2 + (T_s + U_a)^2} \frac{E}{T_s} \exp\left[-\frac{E - U_a}{T_s}\right] dE, \quad E \geq U_a \quad (\text{A.18})$$

where, for clarity, we have defined $T_s \equiv E_{\parallel,s}$. These results have been congregated from knowledge and derivations obtained in publications by Medicus (1961); Evans (1974); Fridman and Lemaire (1980); Strickland et al. (1989); Kaepller (2013).

Appendix B

Simulation Instructions & Flowchart

This appendix gives a quick, high-level overview of the tools and methods used in this thesis, along with instructions to get started. To begin, clone and install the *Aurora GEMINI* repository:

```
git clone https://github.com/317Lab/aurora_gemini.git  
bash aurora_gemini/install.sh
```

This will clone and compile the various dependencies and provides a sample simulation to guide the user along. Figure B.1 outlines the major components of one such sample simulation. At the time of writing, the user is expected to download the appropriate Swarm, SuperDARN, and PFISR vvels data files, however, progress is being made to automate all data ingestion. Naturally, this flowchart is subject to change, but it sets the stage for fully automated curation and preparation of data for simulations, as well as the simulation setup and post-processing themselves. For further details, please see the appropriate documentation found at their respective repositories.

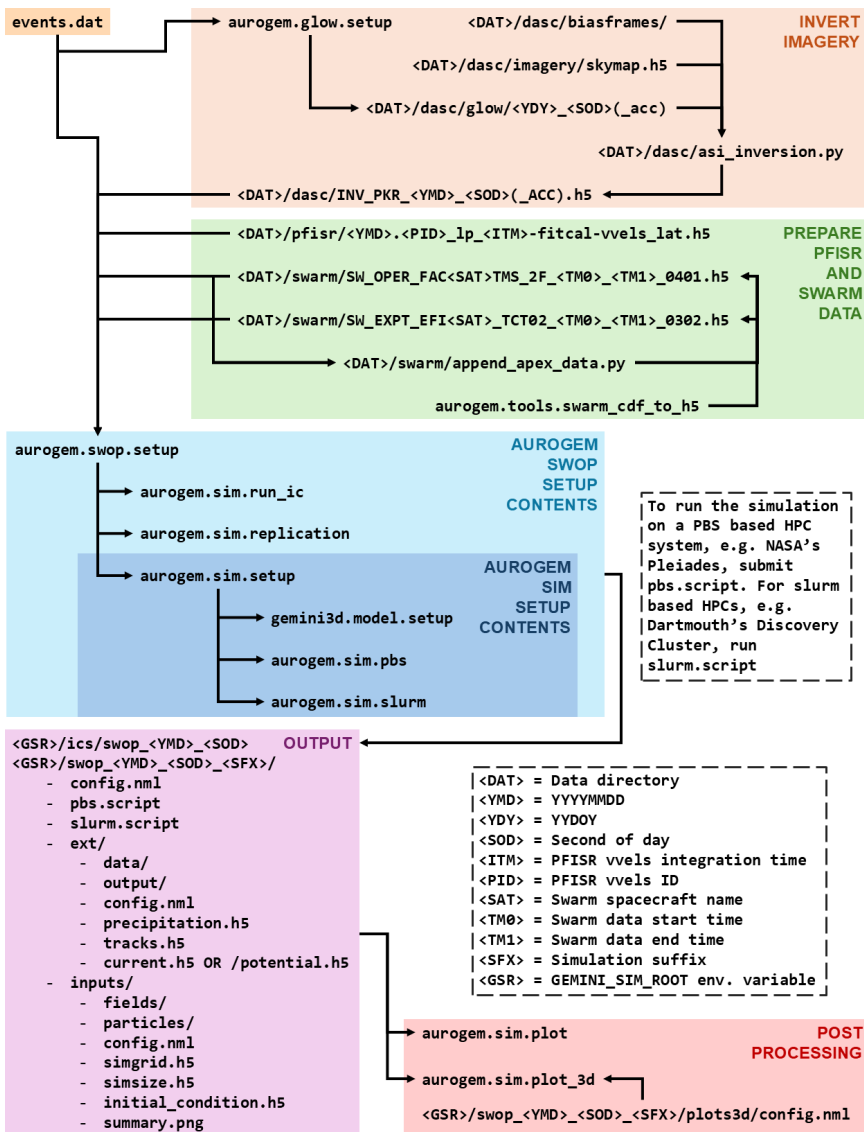


Figure B.1: High-level flowchart for running a data-driven GEMINI simulation.

Appendix C

Simulation Summary & Additional Comparisons

This appendix is almost verbatim, with minor formatting and stylistic modifications, the Supporting Information for the manuscript covered by Chapter 3. The author contributions are that of this same manuscript.

Figures C.1 – C.4, along with Sections C.1 – C.4, cover simulation comparisons that have been omitted from the main manuscript (Chapter 3). They include descriptions and interpretations of their respective simulations, as well as top and side views, along with height-integrated Joule heating, of the two simulations in each comparison.

Figures C.5 – C.22 provide an isometric view, in addition to the top and side views given in their respective comparison figures, of each simulation covered in this work. The captions outline the simulation ID(s) the figures belong to, the combination of parameters, and the tube set ID. The combinations are encoded using SD, PF, and NB for SuperDARN, PFISR, and No Background, AM and UM for Accelerated and Unaccelerated Maxwellians, and AC, xA, xB, or xC referring to the combination of Swarm spacecraft. E.g. SD-UM-xA has a combination of SuperDARN derived background flow, the unaccelerated Maxwellian electron precipitation, and a FAC map replicated with only Swarm A.

C.1 Comparison II: Background Flow

Comparison II, Figure C.1, panels a – b, show the simulation results for the February 12 event with a SuperDARN derived background electric field of 8.6 mV/m directed 10° west of north (Simulation IIa). This is compared

to the similarly strong, PFISR derived 11.9 mV/m in nearly the same direction (panels c – d, Simulation IIb). It is not surprising then, that there are few changes in current closure when comparing the two, as both have similar observations of $\bar{\mathbf{E}}$. One noteworthy difference is the amount of Hall current carried by the orange flux tubes. At 0.8 kA, the Simulation IIb flux tube carries around 33 – 35% more than its Simulation IIa counterpart. This is explained, in large part, by the roughly 38% increase in $\bar{\mathbf{E}}$. This same increase in electric field strength explains the 40 – 50% increase in height-integrated Joule heating, as shown in panels e and f, provided the $\mathbf{j} \cdot \mathbf{E} = \sigma_P |E|^2$ relationship.

The red and green flux tubes for both simulations IIa – b show that the southern downward FAC sheet is not able to fully connect back to the magnetosphere inside this simulation volume. Most of the central upward FAC sheet accounts for the closure of just the northern edge of the primary return current sheet. The green flux tube, probing the bulk of this sheet, shows that around half closes upwards while the remaining 0.5 kA exits through the northern wall.

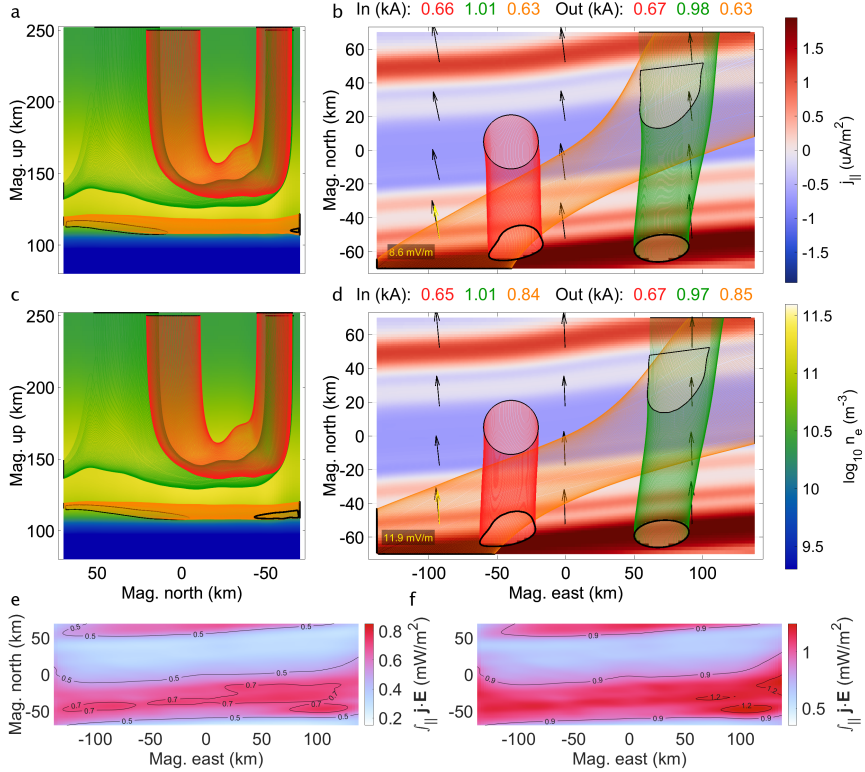


Figure C.1: Comparison II (February 12, 10:22 UT): Top and side views of Simulation IIa with SuperDARN derived background flow (a, b) versus Simulation IIb with PFISR derived background flow (c, d) along with height-integrated Joule heating for Simulation IIa (e) and IIb (f). For plot details, see Section 3.2.8. Data sources: <https://swarm-diss.eo.esa.int> (Swarm), <https://superdarn.ca/data-download> (SuperDARN), <https://data.amisr.com/database> (PFISR), and <https://rcweb.dartmouth.edu/LynchK> (Simulation).

C.2 Comparison IV: Background Flow

Comparison IV, Figure C.2, is similar to Comparison II. Simulations IVa – b both have nearly northward background electric fields with 10.0 mV/m from SuperDARN and 21.0 mV/m from PFISR. Doubling the electric field strength increases the Hall current by a factor of around 2.8, depicted by the orange flux tube carrying 1.5 and 4.2 kA in simulations IVa – b respectively. One small difference between Comparisons II and IV is seen in the red flux tubes of Comparison IV, here carrying 1.3 kA: in Simulation IVa, the red flux tube requires just enough Hall current to rotate slightly to the east at its apex, while its Simulation IVb counterpart closes directly northward. As in Comparison II, again this doubling of the electric field strength nearly quadruples the height-integrated Joule heating, as seen in panels e and f.

The fact that our March 14 conjunction event has its precipitation collocated with downward FAC sheets, we argue, is consistent with both Simulations IVa – b. Given the sufficiently strong electric field strengths, the FAC closure depicted by the green and red flux tubes barely grazes the enhanced density/conductivity caused by the main arc precipitation. This suggests that this auroral arc system has a configuration that uncouples the FAC closure from the accelerated electron precipitation.

Both Comparisons II and IV outline that, in auroral arc systems with Pedersen conductivity sufficient for their FAC demands, FAC closure is less sensitive to the magnitude of the background electric field beyond some point. The Hall currents change mostly in amperage, linearly with the electric field strength, but less so in morphology.

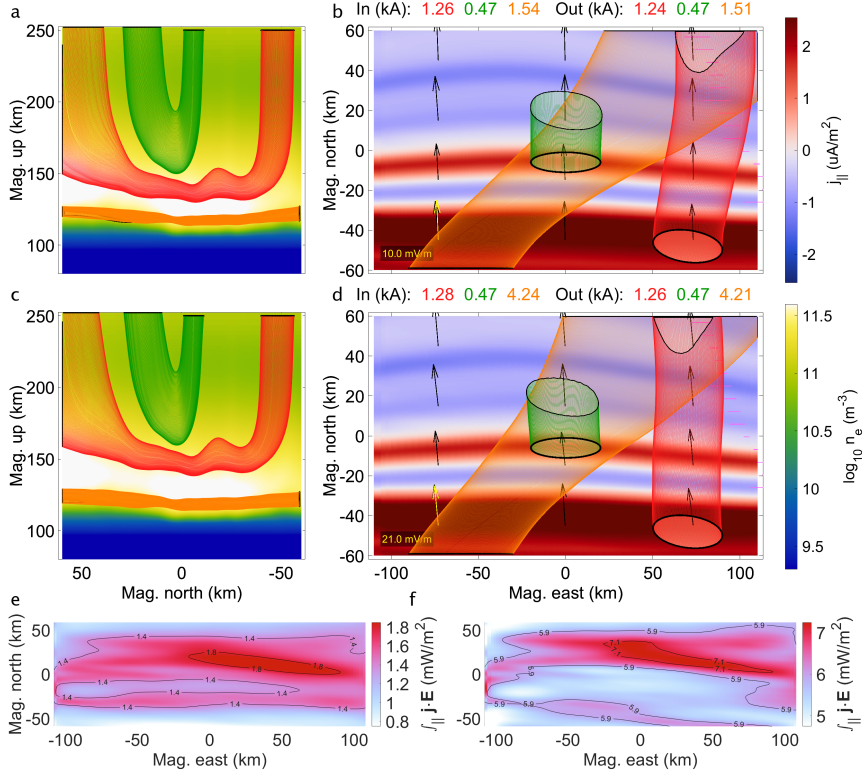


Figure C.2: Comparison IV (March 14, 6:49 UT): Top and side views of Simulation IVa with SuperDARN derived background flow (a, b) versus Simulation IVb with PFISR derived background flow (c, d) along with height-integrated Joule heating for Simulation IVa (e) and IVb (f). For plot details, see Section 3.2.8. Data sources: <https://swarm-diss.eo.esa.int> (Swarm), <https://superdarn.ca/data-download> (SuperDARN), <https://data.amisr.com/database> (PFISR), and <https://rcweb.dartmouth.edu/LynchK> (Simulation).

C.3 Comparison VII: Precipitation Spectra

Comparison VII shows a combination of a strong electric field and weak precipitation, in contrast to Comparison VI which shows a combination of a weak electric field and sufficiently energetic, low-reaching precipitation, and Comparison VIII with a very strong background electric field and the most energetic precipitation in our list of events.

Figure C.3 shows the simulations from Comparison VII which both assume the nearly northward background electric field of 8.6 mV/m, as estimated by SuperDARN, like in Comparison II. This, combined with the weakest precipitations of our conjunction events—an energy flux of $Q_p = 2.3 \text{ mW/m}^2$, acceleration potential of $U_a = 1.9 \text{ keV}$, and characteristic energy of $E_0 = 1.4 \text{ keV}$ (see Figure 3.5 and Table 3.1)—renders this comparison relatively unaffected by the assumption of $\phi_u(E)$ over $\phi_a(E)$. The electron density in Simulation VIIb does drop lower by around 5 km, which adds a slight eastward drift to the green flux tube and provides around 0.6 kA more to the orange tube.

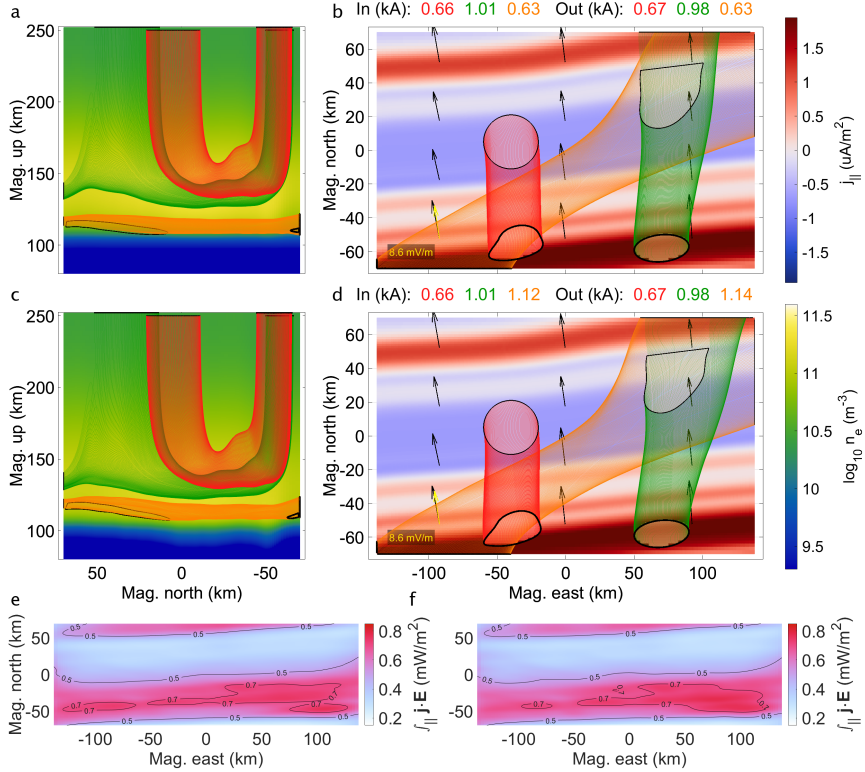


Figure C.3: Comparison VII (February 12, 10:22 UT): Top and side views of Simulation VIIa with accelerated Maxwellian electron precipitation (a, b) versus Simulation VIIb with unaccelerated Maxwellian electron precipitation (c, d) along with height-integrated Joule heating for Simulation VIIa (e) and VIIb (f). For plot details, see Section 3.2.8. Data sources: <https://swarm-diss.eo.esa.int> (Swarm), <https://superdarn.ca/data-download> (SuperDARN), and <https://rcweb.dartmouth.edu/LynchK> (Simulation).

C.4 Comparison IX: Precipitation Spectra

Figure C.4 depicts Comparison IX. The flux tubes in both Simulations IXa – b all have rather agitated shapes, including the out-flux curves, because of the relatively noisy imagery pertaining to this event, which shows through the inverted energy flux depicted by Figure 3.5j. Regardless, the FAC, electric field strength, and precipitation parameters are all low, other than the source region characteristic energy, $T_s = 860$ eV (see Table 3.1). In terms of electron density enhancements, panels a and c show how a ratio of acceleration potential to source region characteristic energy of $U_a/T_s \approx 3.5$, compared to the previous ~ 7.5 in Simulation VIIIa, still does not match the affects from an unaccelerated $U_s/T_s = 1$ assumption to E-region densities.

Furthermore, the low FAC requirements, together with the wider spread of the precipitation energies, work in the favor of Pedersen closure, while the remaining parameters suggest a need for Hall closure. Ultimately, we see here that the $\phi_u(E)$ versus $\phi_a(E)$ assumption has a less pronounced effect on current closure morphology or the height-integrated Joule heating. The green current flux tube in Simulation IXb, albeit less dramatic, does stretch in the along-arc directions, perpendicular to \mathbf{E} , compared to Simulation IXa, suggesting increased amounts of Hall closure, but the orange nor red flux tubes vary greatly.

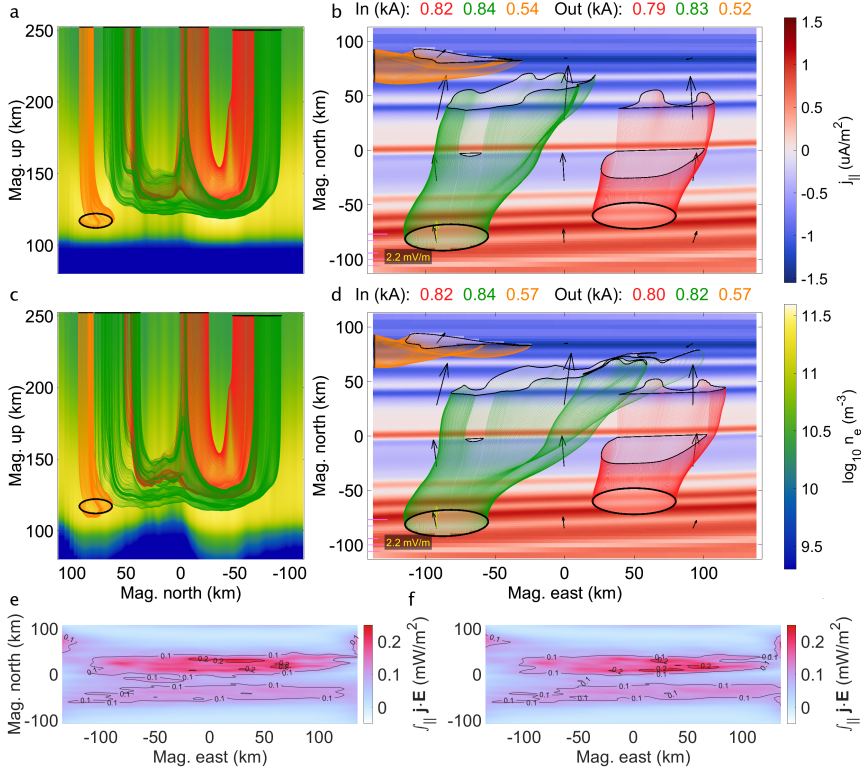


Figure C.4: Comparison IX (March 4, 10:14 UT): Top and side views of Simulation IXa with accelerated Maxwellian electron precipitation (a, b) versus Simulation IXb with unaccelerated Maxwellian electron precipitation (c, d) along with height-integrated Joule heating for Simulation IXa (e) and IXb (f). For plot details, see Section 3.2.8. Data sources: <https://swarm-diss.eo.esa.int> (Swarm), <https://superdarn.ca/data-download> (SuperDARN), and <https://rcweb.dartmouth.edu/LynchK> (Simulation).

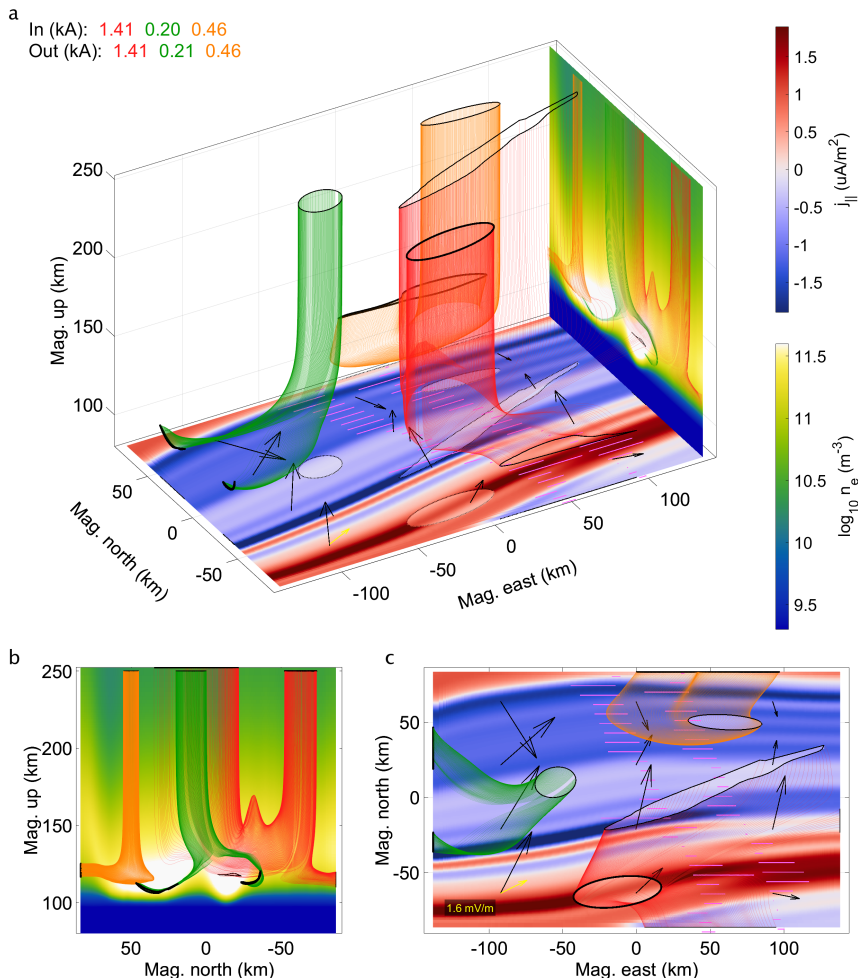


Figure C.5: Simulations Ia, VIIa, and Xa (February 10, 9:51 UT). Combination: SD-AM-AC. Tube set: 1. For plot details, see Section 3.2.8. Data sources found in respective comparison figures and the Open Research Section.

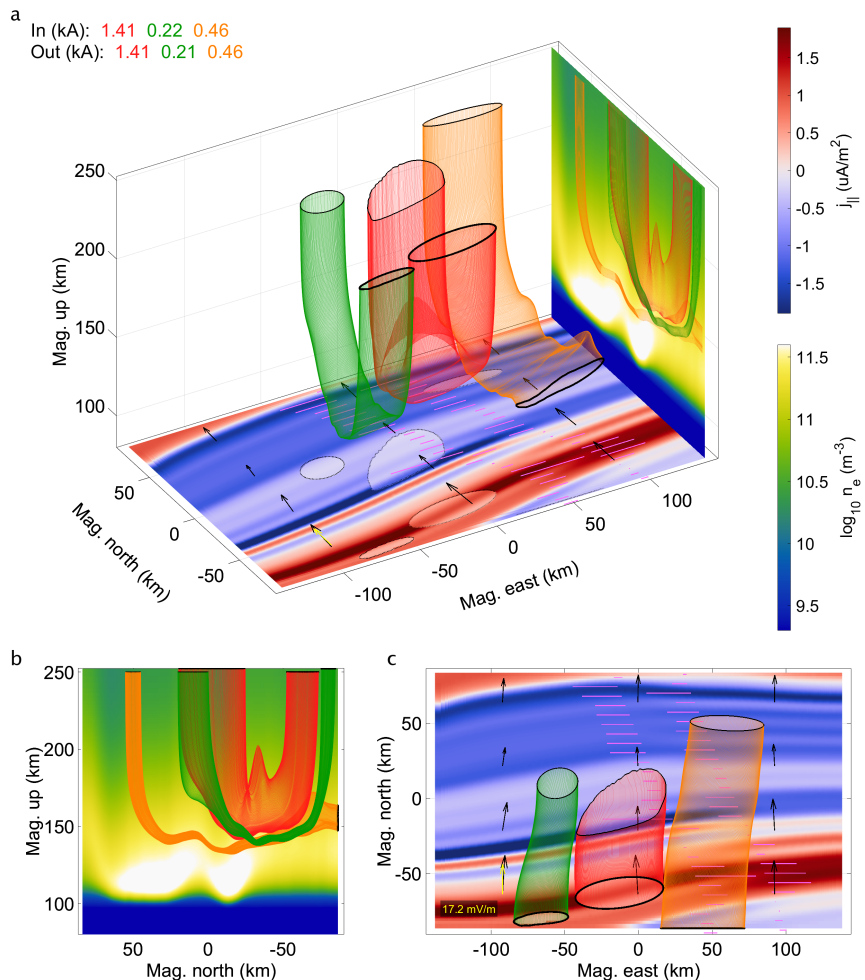


Figure C.6: Simulation Ib (February 10, 9:51 UT). Combination: PF-AM-AC. Tube set: 1. For plot details, see Section 3.2.8. Data sources found in respective comparison figures and the Open Research Section.

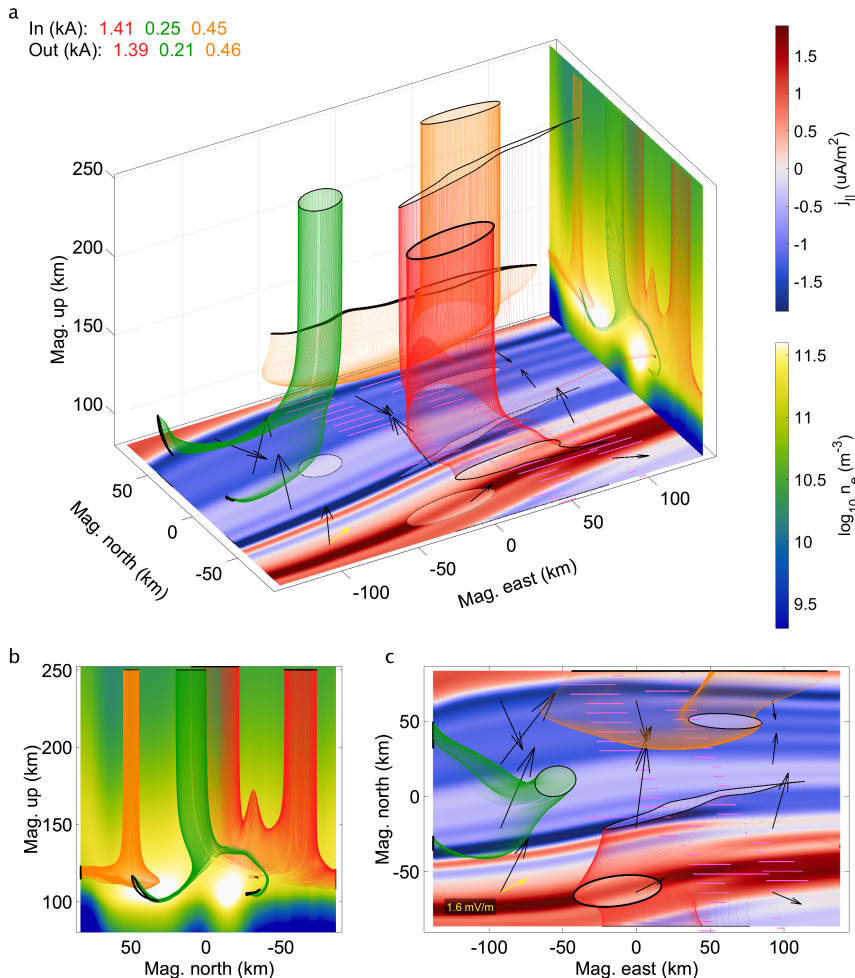


Figure C.7: Simulation VIb (February 10, 9:51 UT). Combination: SD-UM-AC. Tube set: 1. For plot details, see Section 3.2.8. Data sources found in respective comparison figures and the Open Research Section.

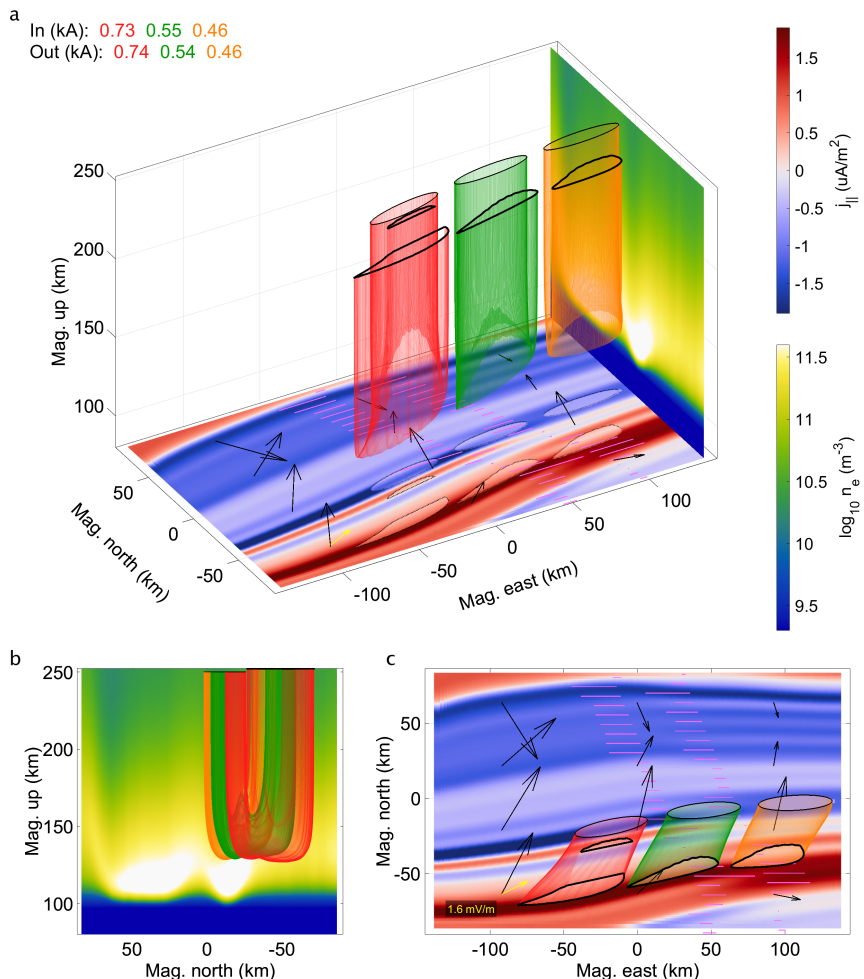


Figure C.8: Simulations Ia, VIa, and Xa (February 10, 9:51 UT). Combination: SD-AM-AC. Tube set: 2. For plot details, see Section 3.2.8. Data sources found in respective comparison figures and the Open Research Section.

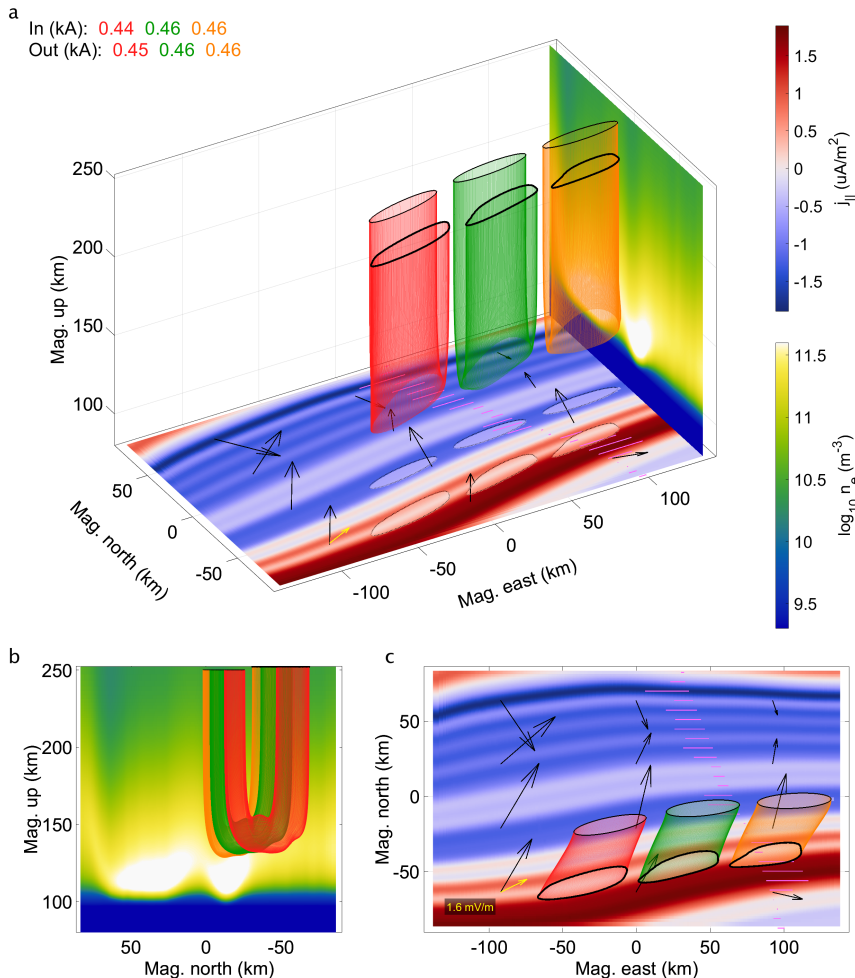


Figure C.9: Simulation Xb (February 10, 9:51 UT). Combination: SD-AM-xA. Tube set: 2. For plot details, see Section 3.2.8. Data sources found in respective comparison figures and the Open Research Section.

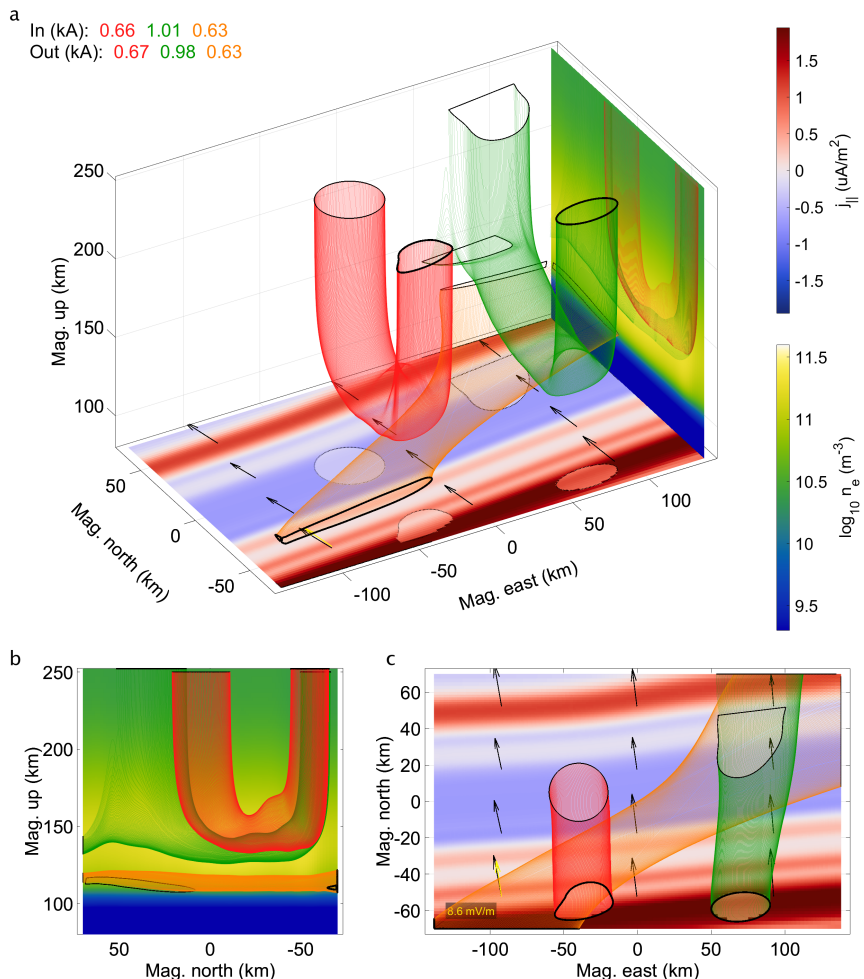


Figure C.10: Simulations IIa and VIIa (February 12, 10:22 UT). Combination: SD-AM-xC. Tube set: 1. For plot details, see Section 3.2.8. Data sources found in respective comparison figures and the Open Research Section.

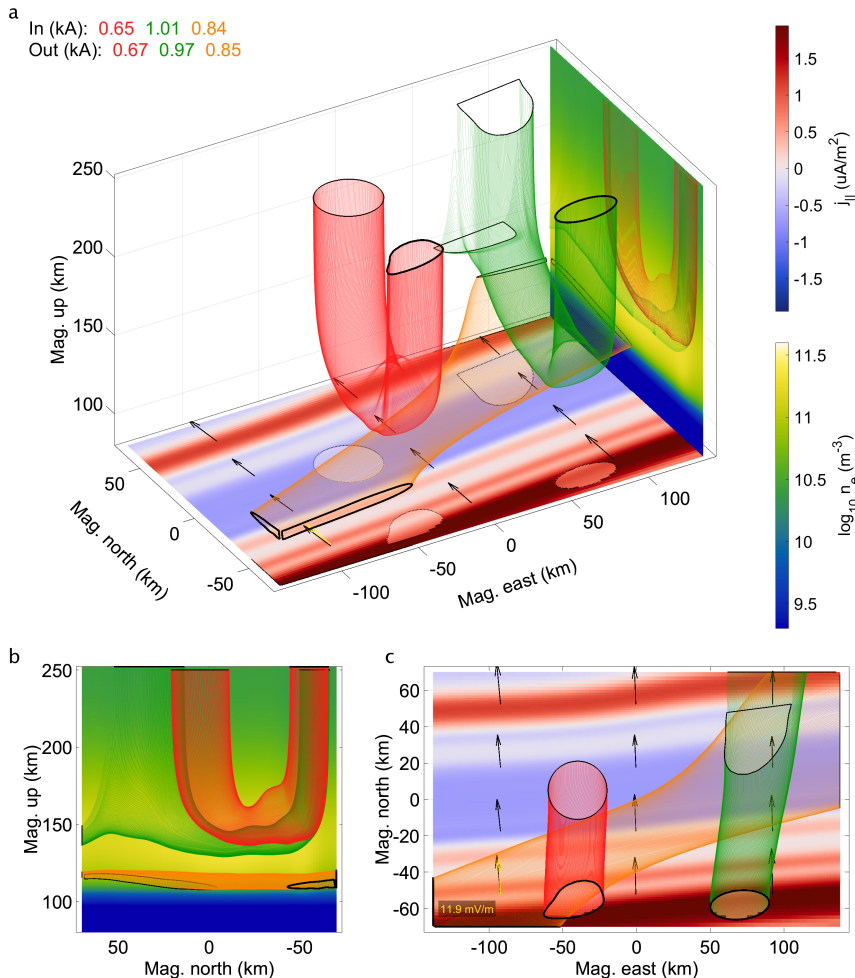


Figure C.11: Simulation IIb (February 12, 10:22 UT). Combination: PF-AM-xC. Tube set: 1. For plot details, see Section 3.2.8. Data sources found in respective comparison figures and the Open Research Section.

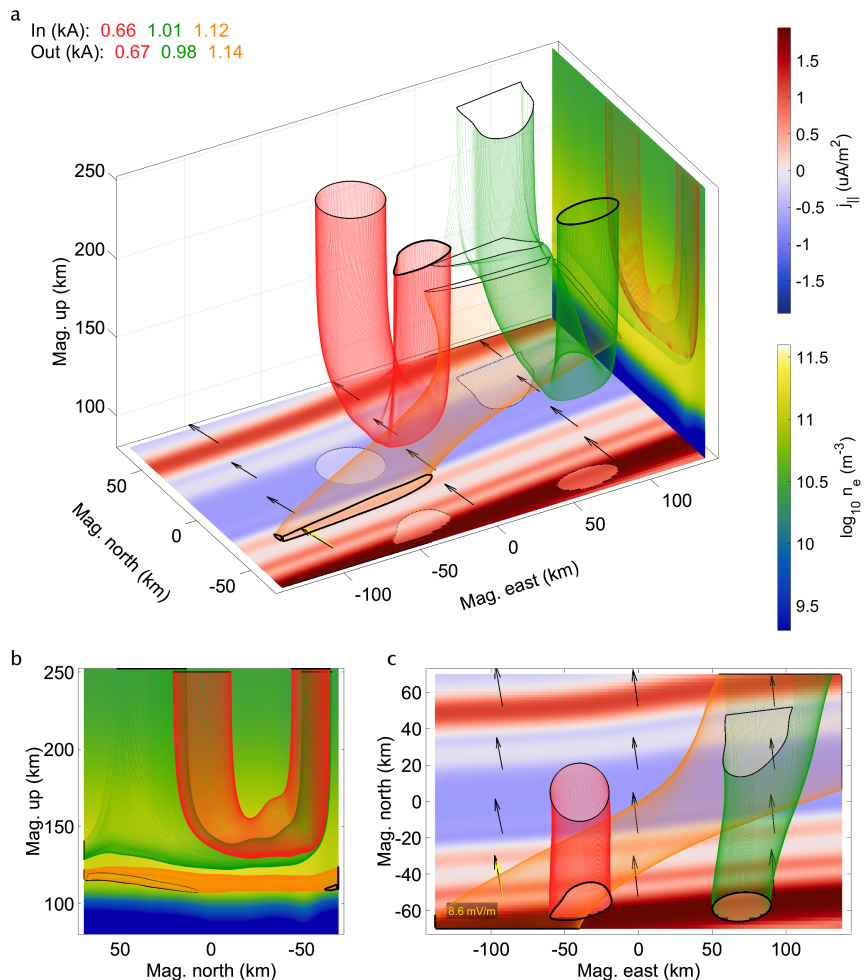


Figure C.12: Simulation VIIb (February 12, 10:22 UT). Combination: SD-UM-xC. Tube set: 1. For plot details, see Section 3.2.8. Data sources found in respective comparison figures and the Open Research Section.

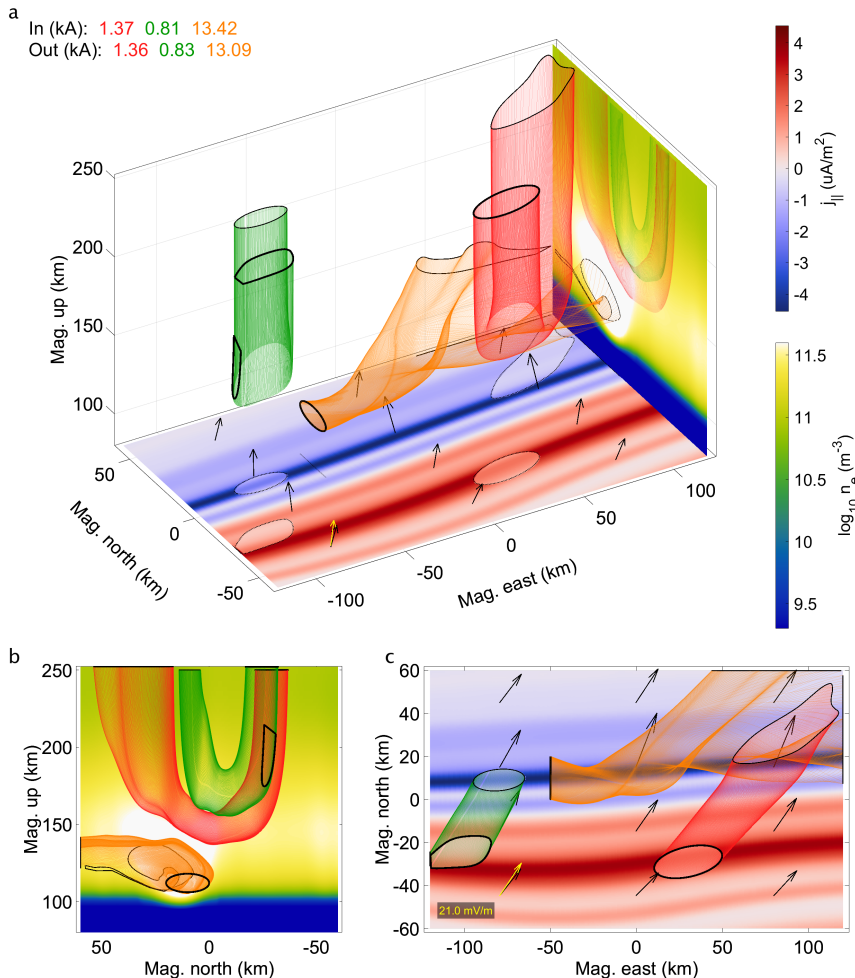


Figure C.13: Simulations IIIa and VIIa (March 4, 7:30 UT). Combination: SD-AM-xC. Tube set: 1. For plot details, see Section 3.2.8. Data sources found in respective comparison figures and the Open Research Section.

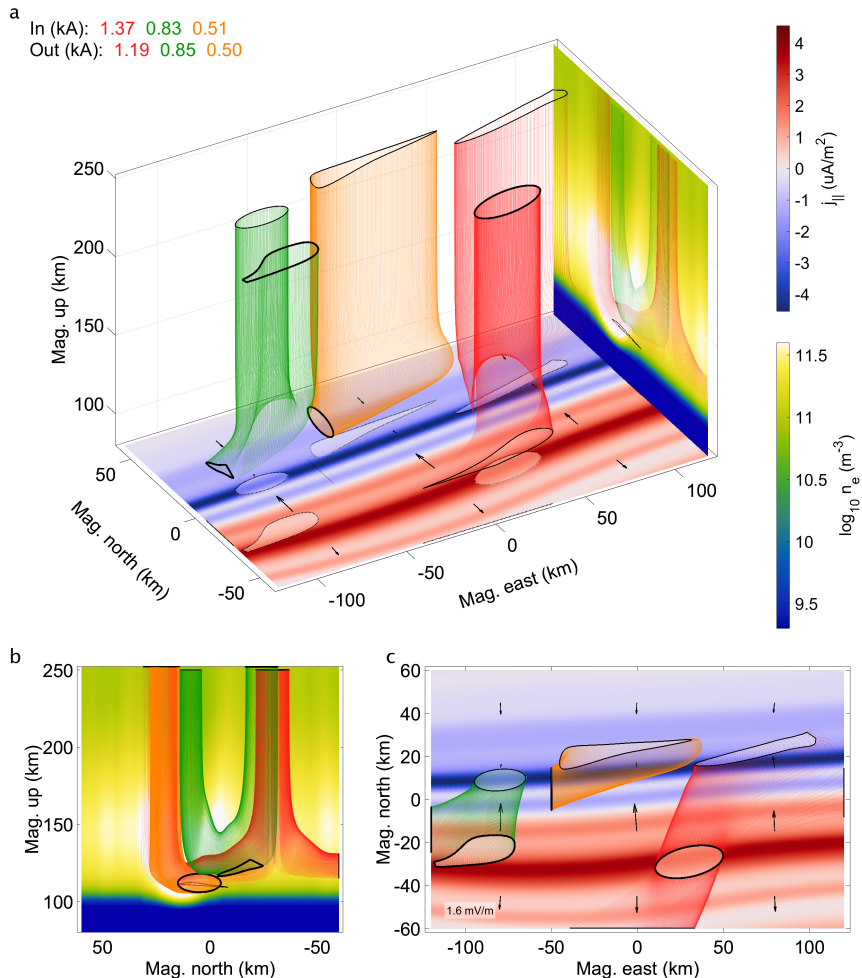


Figure C.14: Simulation IIIb (March 4, 7:30 UT). Combination: NB-AM-xC. Tube set: 1. For plot details, see Section 3.2.8. Data sources found in respective comparison figures and the Open Research Section.

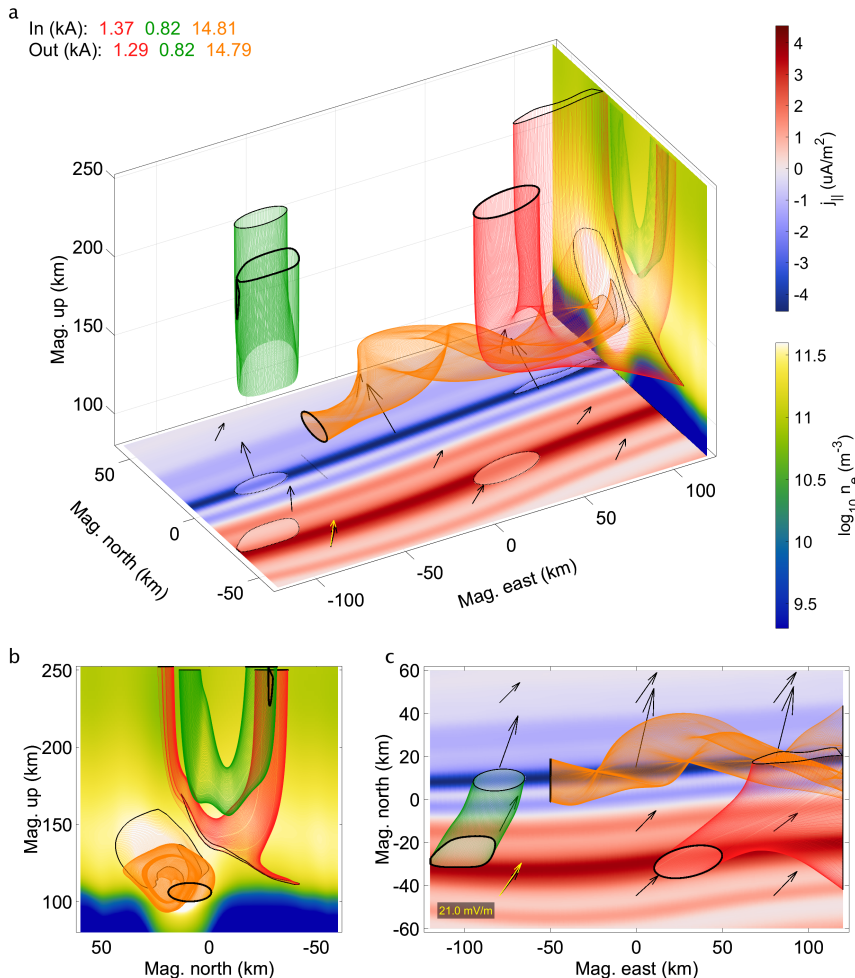


Figure C.15: Simulation VIIb (March 4, 7:30 UT). Combination: SD-UM-xC. Tube set: 1. For plot details, see Section 3.2.8. Data sources found in respective comparison figures and the Open Research Section.

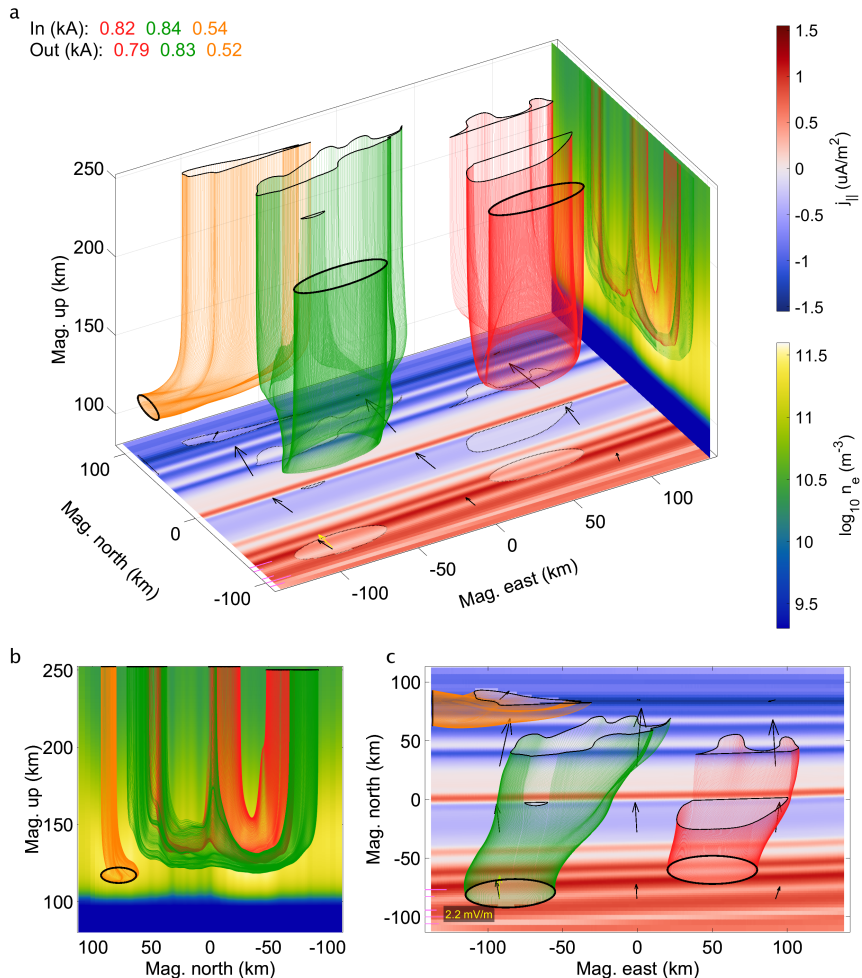


Figure C.16: Simulation IXa (March 4, 10:14 UT). Combination: SD-AM-xB. Tube set: 1. For plot details, see Section 3.2.8. Data sources found in respective comparison figures and the Open Research Section.

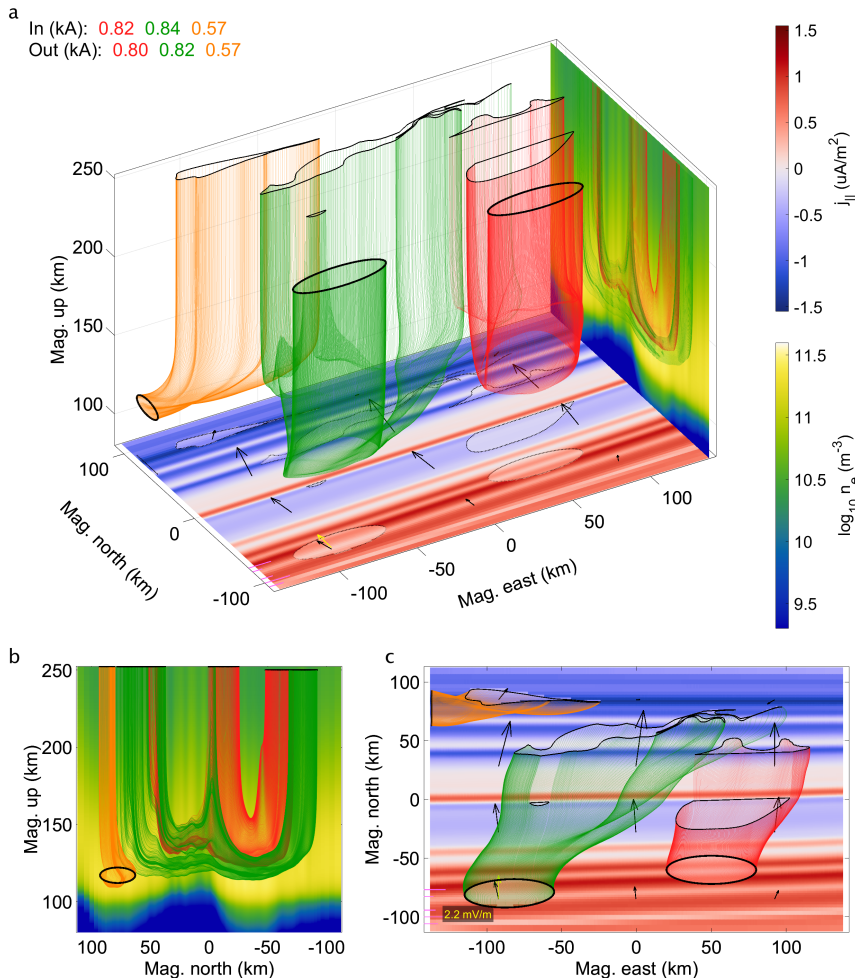


Figure C.17: Simulation IXb (March 4, 10:14 UT). Combination: SD-UM-xB. Tube set: 1. For plot details, see Section 3.2.8. Data sources found in respective comparison figures and the Open Research Section.

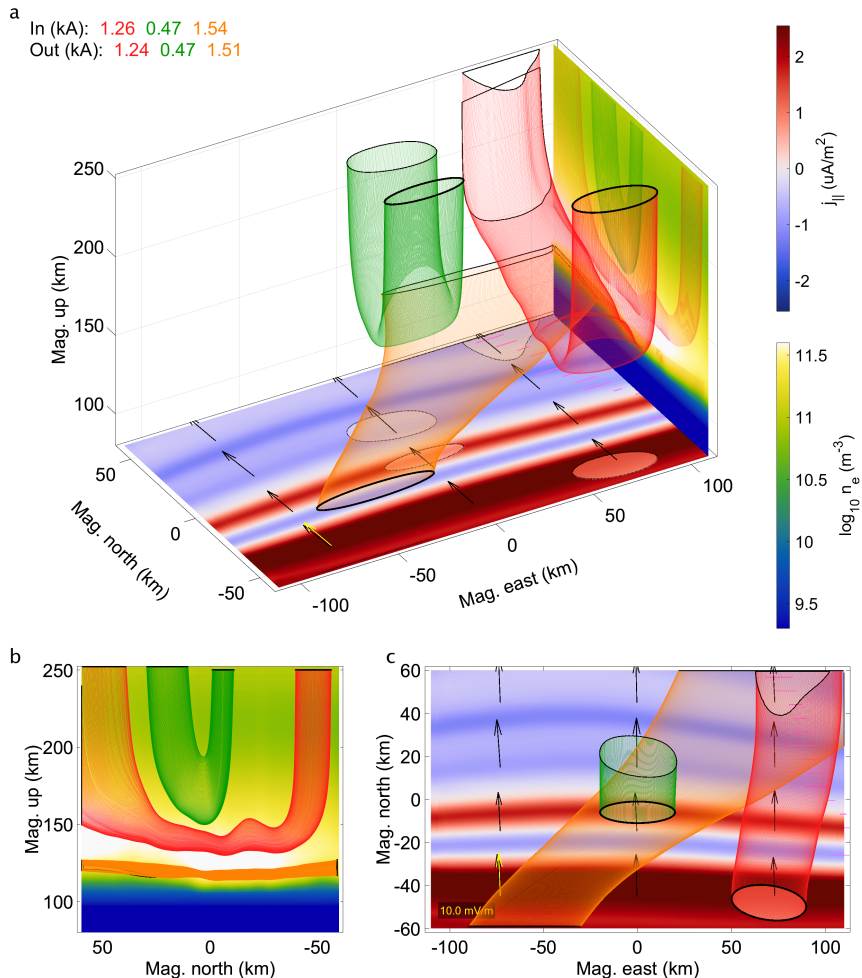


Figure C.18: Simulations IVa and XIa (March 14, 6:49 UT). Combination: SD-AM-AC. Tube set: 1. For plot details, see Section 3.2.8. Data sources found in respective comparison figures and the Open Research Section.

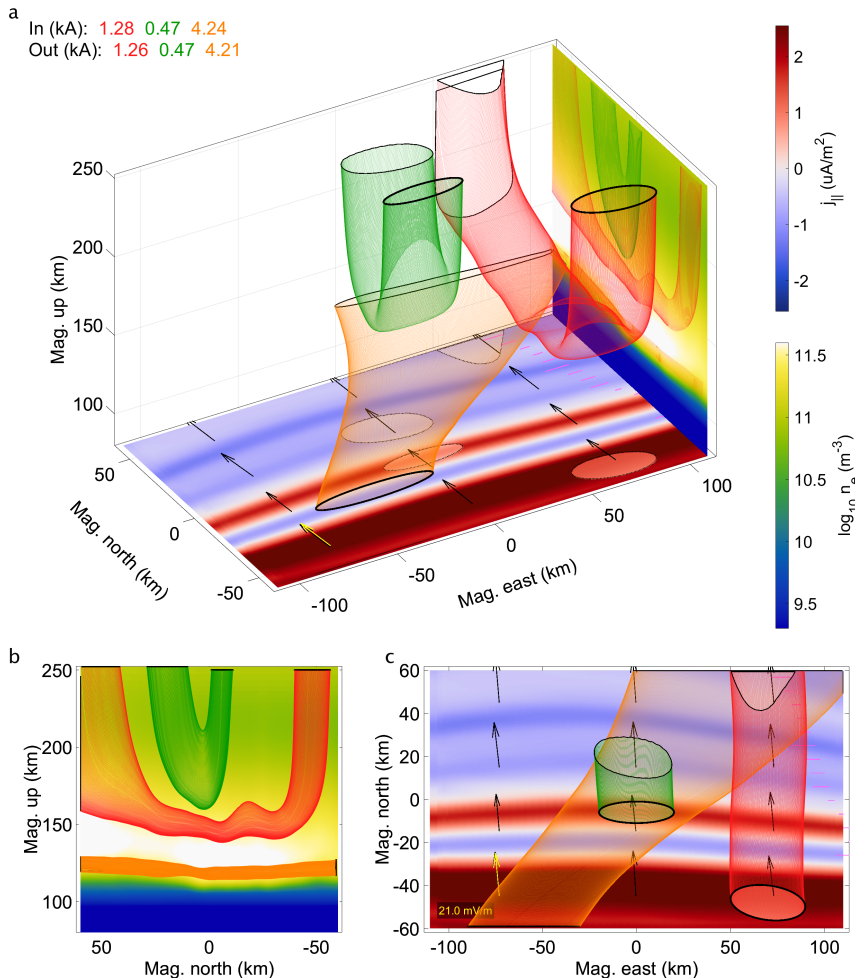


Figure C.19: Simulation IVb (March 14, 6:49 UT). Combination: PF-AM-AC. Tube set: 1. For plot details, see Section 3.2.8. Data sources found in respective comparison figures and the Open Research Section.

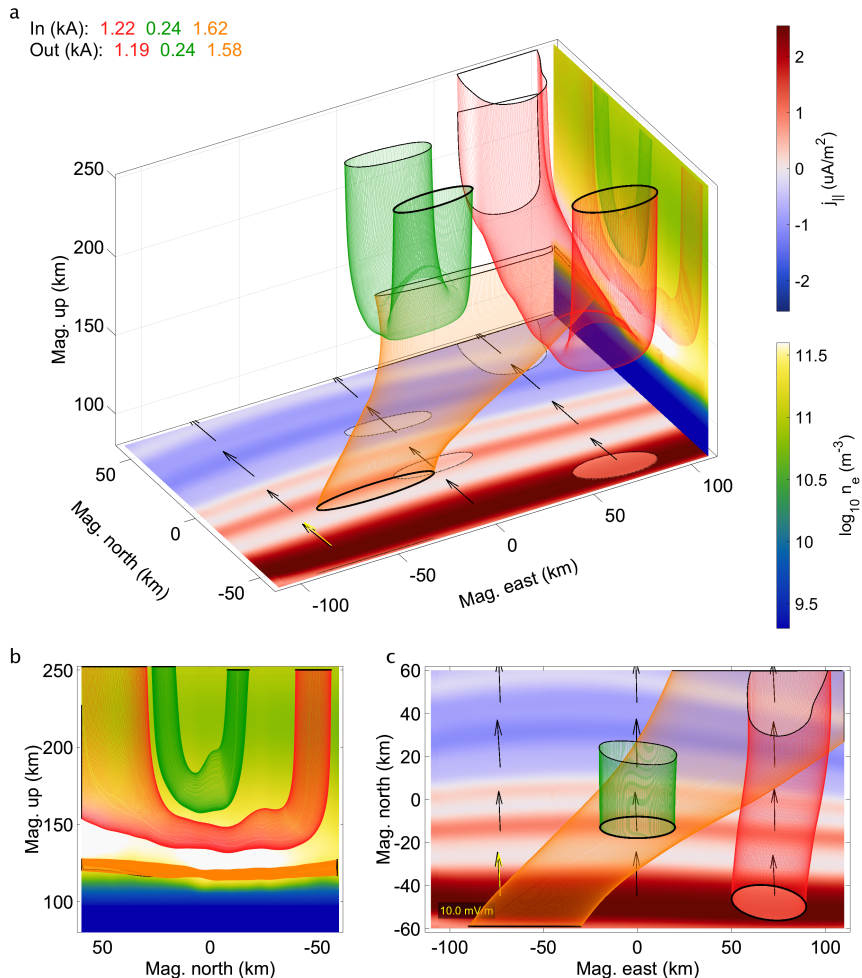


Figure C.20: Simulation XIb (March 14, 6:49 UT). Combination: SD-AM-xA. Tube set: 1. For plot details, see Section 3.2.8. Data sources found in respective comparison figures and the Open Research Section.

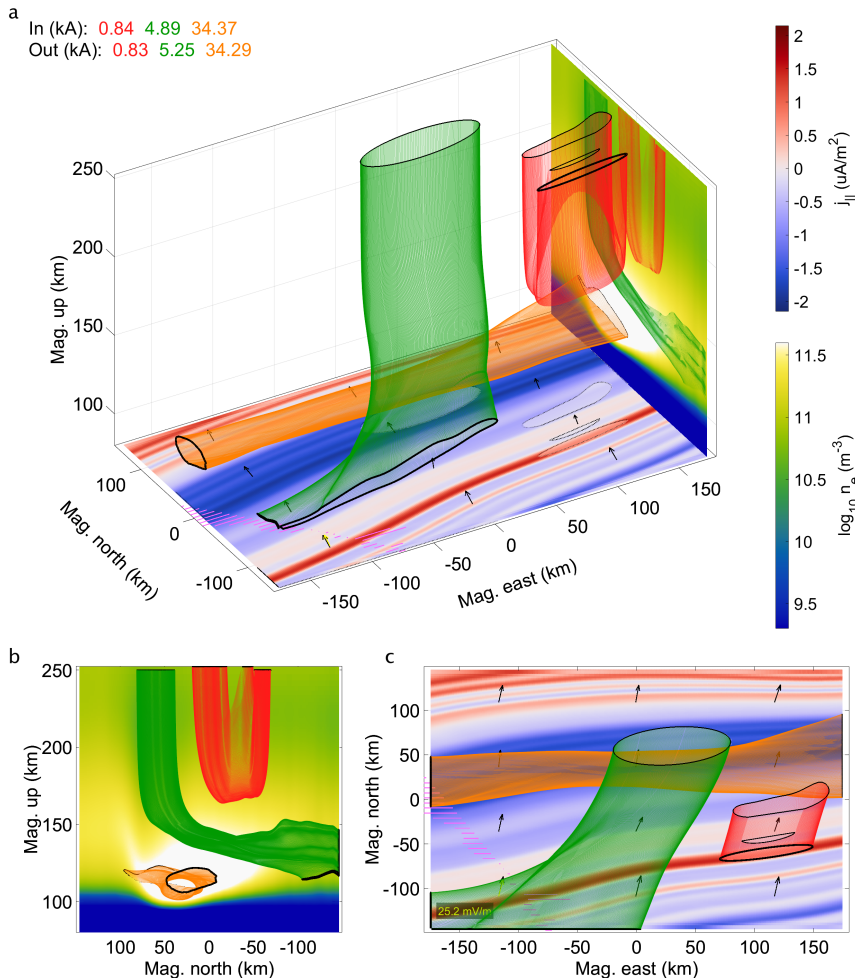


Figure C.21: Simulation Va (March 19, 8:23 UT). Combination: SD-AM-xB. Tube set: 1. For plot details, see Section 3.2.8. Data sources found in respective comparison figures and the Open Research Section.

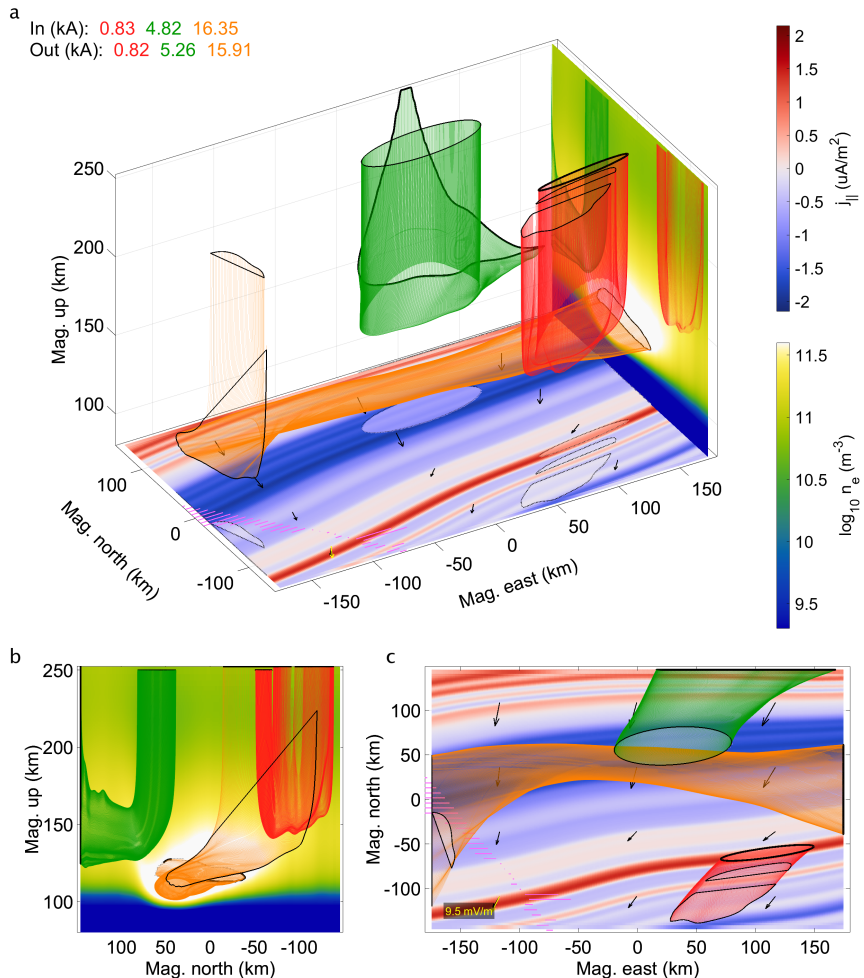


Figure C.22: Simulation Vb (March 19, 8:23 UT). Combination: PF-AM-xB. Tube set: 1. For plot details, see Section 3.2.8. Data sources found in respective comparison figures and the Open Research Section.

Bibliography

- Ahlfors, L. V. (1953). Complex analysis: An introduction to the theory of analytic functions of one complex variable. *New York, London*, 177.
- Alfvén, H. (1943). On the existence of electromagnetic-hydrodynamic waves. *Arkiv for matematik, astronomi och fysik*, 29:1 – 7.
- Amm, O. (1997). Ionospheric elementary current systems in spherical coordinates and their application. *Journal of Geomagnetism and Geoelectricity*, 49(7):947 – 955.
- Amm, O., Aruliah, A., Buchert, S. C., Fujii, R., Gjerloev, J. W., Ieda, A., Matsuo, T., Stolle, C., Vanhamäki, H., and Yoshikawa, A. (2008). Towards understanding the electrodynamics of the 3-dimensional high-latitude ionosphere: Present and future. *Annales Geophysicae*, 26(12):3913 – 3932.
- Amm, O., Fujii, R., Kauristie, K., Aikio, A., Yoshikawa, A., Ieda, A., and Vanhamäki, H. (2011). A statistical investigation of the Cowling channel efficiency in the auroral zone. *Journal of Geophysical Research: Space Physics*, 116(A2).
- Archer, W. E., Knudsen, D. J., Burchill, J. K., Jackel, B., Donovan, E., Connors, M., and Juusola, L. (2017). Birkeland current boundary flows. *Journal of Geophysical Research: Space Physics*, 122(4):4617 – 4627.
- Bristow, W. A., Hampton, D. L., and Otto, A. (2016). High-spatial-resolution velocity measurements derived using Local Divergence-Free Fitting of SuperDARN observations. *Journal of Geophysical Research: Space Physics*, 121(2):1349 – 1361.
- Burchill, J. K. and Knudsen, D. J. (2022). Swarm Thermal Ion Imager measurement performance. *Earth, Planets and Space*, 74(1):181.
- Clayton, R., Burleigh, M., Lynch, K. A., Zettergren, M., Evans, T., Grubbs, G., Hampton, D. L., Hysell, D., Kaepller, S., Lessard, M., Michell, R.,

Bibliography

- Reimer, A., Roberts, M., Samara, M., and Varney, R. (2021). Examining the auroral ionosphere in three dimensions using reconstructed 2D maps of auroral data to drive the 3D GEMINI model. *Journal of Geophysical Research: Space Physics*, 126(11).
- Clayton, R., Lynch, K., Zettergren, M., Burleigh, M., Conde, M., Grubbs, G., Hampton, D., Hysell, D., Lessard, M., Michell, R., Reimer, A., Roberts, T. M., Samara, M., and Varney, R. (2019). Two-dimensional maps of in situ ionospheric plasma flow data near auroral arcs using auroral imagery. *Journal of Geophysical Research: Space Physics*, 124(4):3036 – 3056.
- Conde, M., Craven, J. D., Immel, T., Hoch, E., Stenbaek-Nielsen, H., Hallinan, T., Smith, R. W., Olson, J., Sun, W., Frank, L. A., and Sigwarth, J. (2001). Assimilated observations of thermospheric winds, the aurora, and ionospheric currents over Alaska. *Journal of Geophysical Research: Space Physics*, 106(A6):10493 – 10508.
- Cowley, S. W. H. (2000). Magnetosphere-ionosphere interactions: A tutorial review. *Magnetospheric Current Systems, Geophysical Monograph Series*, 118:91 – 106.
- Cowling, T. G. (1932). The electrical conductivity of an ionised gas in the presence of a magnetic field. *Monthly Notices of the Royal Astronomical Society*, 93(1):90 – 97.
- Dahlgren, H., Gustavsson, B., Lanchester, B. S., Ivchenko, N., Brändström, U., Whiter, D. K., Sergienko, T., Sandahl, I., and Marklund, G. (2011). Energy and flux variations across thin auroral arcs. *Annales Geophysicae*, 29(10):1699 – 1712.
- DASC (2025). <ftp://optics.gi.alaska.edu/GAK/DASC>.
- Dhadly, M. S. and Conde, M. (2016). Distortion of thermospheric air masses by horizontal neutral winds over Poker Flat Alaska measured using an all-sky scanning Doppler imager. *Journal of Geophysical Research: Space Physics*, 121(1):854 – 866.
- Drob, D. P., Emmert, J. T., Meriwether, J. W., Makela, J. J., Doornbos, E., Conde, M., Hernandez, G., Noto, J., Zawdie, K. A., McDonald, S. E., Huba, J. D., and Klenzing, J. H. (2015). An update to the horizontal wind model (HWM): The quiet time thermosphere. *Earth and Space Science*, 2(7):301 – 319.
- Dungey, J. W. (1961). Interplanetary magnetic field and the auroral zones. *Physical Review Letters*, 6:47 – 48.

- Emmert, J. T., Drob, D. P., Picone, J. M., Siskind, D. E., Jones Jr., M., Mlynczak, M. G., Bernath, P. F., Chu, X., Doornbos, E., Funke, B., Goncharenko, L. P., Hervig, M. E., Schwartz, M. J., Sheese, P. E., Vargas, F., Williams, B. P., and Yuan, T. (2021). NRLMSIS 2.0: A whole-atmosphere empirical model of temperature and neutral species densities. *Earth and Space Science*, 8(3):e2020EA001321.
- Enengl, F., Kotova, D., Jin, Y., Clausen, L. B. N., and Miloch, W. J. (2023). Ionospheric plasma structuring in relation to auroral particle precipitation. *Journal of Space Weather and Space Climate*, 13.
- Ergun, R. E., Andersson, L., Main, D. S., Su, Y.-J., Carlson, C. W., McFadden, J. P., and Mozer, F. S. (2002). Parallel electric fields in the upward current region of the aurora: Indirect and direct observations. *Physics of Plasmas*, 9(9):3685 – 3694.
- Erlandson, R., Lynch, K. A., Samara, M., Anderson, B., Bortnik, J., Burleigh, M., Deshpande, K., Hampton, D., Kistler, L., Knudsen, D., LaBelle, J., Lyon, J., Magnes, W., Michell, R., Mouikis, C., Nakamura, R., Nikoukar, R., Torbert, R., van Irsel, J., Vines, S., Zettergren, M., and Zou, S. (2024). ARCS: Auroral Reconstruction CubeSwarm. A 2019 Heliophysics Medium-Class Explorer Phase A Concept Study. Section E: Science Implementation. NASA Technical Report.
- Evans, D. S. (1968). The observations of a near monoenergetic flux of auroral electrons. *Journal of Geophysical Research (1896 – 1977)*, 73(7):2315 – 2323.
- Evans, D. S. (1974). Precipitating electron fluxes formed by a magnetic field aligned potential difference. *Journal of Geophysical Research*, 79(19):2853 – 2858.
- Fang, X., Randall, C. E., Lummerzheim, D., Solomon, S. C., Mills, M. J., Marsh, D. R., Jackman, C. H., Wang, W., and Lu, G. (2008). Electron impact ionization: A new parameterization for 100 eV to 1 MeV electrons. *Journal of Geophysical Research: Space Physics*, 113(A9).
- Fang, X., Randall, C. E., Lummerzheim, D., Wang, W., Lu, G., Solomon, S. C., and Frahm, R. A. (2010). Parameterization of monoenergetic electron impact ionization. *Geophysical Research Letters*, 37(22).
- Farley Jr., D. T. (1959). A theory of electrostatic fields in a horizontally stratified ionosphere subject to a vertical magnetic field. *Journal of Geophysical Research (1896 – 1977)*, 64(9):1225 – 1233.

Bibliography

- Fridman, M. and Lemaire, J. (1980). Relationship between auroral electrons fluxes and field aligned electric potential difference. *Journal of Geophysical Research: Space Physics*, 85(A2):664 – 670.
- Fujii, R., Amm, O., Vanhamäki, H., Yoshikawa, A., and Ieda, A. (2012). An application of the finite length Cowling channel model to auroral arcs with longitudinal variations. *Journal of Geophysical Research: Space Physics*, 117.
- Fujii, R., Amm, O., Yoshikawa, A., Ieda, A., and Vanhamäki, H. (2011). Reformulation and energy flow of the Cowling channel. *Journal of Geophysical Research: Space Physics*, 116(A2).
- Greenwald, R. A., Baker, K. B., Dudeney, J. R., Pinnock, M., Jones, T. B., Thomas, E. C., Villain, J.-P., Cerisier, J.-C., Senior, C., Hanuse, C., Hunsucker, R. D., Sofko, G., Koehler, J., Nielsen, E., Pellinen, R., Walker, A. D. M., Sato, N., and Yamagishi, H. (1995). DARN/SuperDARN. *Space Science Reviews*, 71(1):761 – 796.
- Griffiths, D. (2017). *Introduction to Electrodynamics*. Cambridge University Press.
- Grubbs II, G., Michell, R., Samara, M., Hampton, D., Hecht, J., Solomon, S., and Jahn, J. (2018a). A comparative study of spectral auroral intensity predictions from multiple electron transport models. *Journal of Geophysical Research: Space Physics*, 123(1):993 – 1005.
- Grubbs II, G., Michell, R., Samara, M., Hampton, D., and Jahn, J. (2018b). Predicting electron population characteristics in 2-D using multispectral ground-based imaging. *Geophysical Research Letters*, 45(1):15 – 20.
- Gurnett, D. A. and Bhattacharjee, A. (2017). *Introduction to plasma physics: With space, laboratory and astrophysical applications*. Cambridge University Press.
- Haerendel, G. (1994). Acceleration from field-aligned potential drops. *International Astronomical Union Colloquium*, 142:765 – 774.
- Haerendel, G. (2021). Auroral arcs: The fracture theory revisited. *Journal of Geophysical Research: Space Physics*, 126(1).
- Hall, E. H. et al. (1879). On a new action of the magnet on electric currents. *American Journal of Mathematics*, 2(3):287 – 292.
- Hecht, J., Strickland, D., and Conde, M. (2006). The application of ground-based optical techniques for inferring electron energy deposition and composition change during auroral precipitation events. *Journal of Atmospheric and Solar-Terrestrial Physics*, 68(13):1502 – 1519.

- Hecht, J. H., Mulligan, T., Correira, J. T., Clemons, J. H., Strickland, D. J., Walterscheid, R. L., and Conde, M. G. (2012). A multiyear (2002 – 2006) climatology of O/N2 in the lower thermosphere from TIMED GUVI and ground-based photometer observations. *Journal of Geophysical Research: Space Physics*, 117(A3).
- Heinselman, C. J. and Nicolls, M. J. (2008). A Bayesian approach to electric field and E-region neutral wind estimation with the Poker Flat Advanced Modular Incoherent Scatter Radar. *Radio Science*, 43(5).
- Jago, L. (2001). *The Northern Lights*. A Borzoi book. Knopf.
- Janhunen, P. (2001). Reconstruction of electron precipitation characteristics from a set of multiwavelength digital all-sky auroral images. *Journal of Geophysical Research: Space Physics*, 106(A9):18505 – 18516.
- Kaepller, S., Markowski, D. G., Pepper, A. M., Troyer, R., Jaynes, A. N., Varney, R. H., and Hampton, D. (2023). Data-driven empirical conductance relations during auroral precipitation using incoherent scatter radar and all sky imagers. *Journal of Geophysical Research: Space Physics*.
- Kaepller, S. R. (2013). *A rocket-borne investigation of auroral electrodynamics within the auroral-ionosphere*. PhD thesis, University of Iowa.
- Kaepller, S. R., Kletzing, C. A., Rowland, D. E., Jones, S., Heinselman, C. J., Bounds, S. R., Gjerloev, J. W., Anderson, B. J., Korth, H., LaBelle, J. W., Dombrowski, M. P., Lessard, M., and Pfaff, R. F. (2012). Current closure in the auroral ionosphere: Results from the auroral current and electrodynamics structure rocket mission.
- Kamide, Y., Richmond, A. D., and Matsushita, S. (1981). Estimation of ionospheric electric fields, ionospheric currents, and field-aligned currents from ground magnetic records. *Journal of Geophysical Research: Space Physics*, 86(A2):801 – 813.
- Karlsson, T., Andersson, L., Gillies, D., Lynch, K., Marghitu, O., Partamies, N., Sivadas, N., and Wu, J. (2020). Quiet, discrete auroral arcs-observations. *Space Science Reviews*, 216(1):1 – 50.
- Kelley, M. C. (2009). *The Earth's ionosphere: Plasma physics and electrodynamics*. International Geophysics Series, v. 96. Academic Press, Amsterdam, Netherlands, 2nd edition.
- Kelly, J. and Heinselman, C. (2009). Initial results from Poker Flat Incoherent Scatter Radar (PFISR). *Journal of Atmospheric and Solar-Terrestrial Physics*, 71(6):635.

Bibliography

- Khazanov, G. V., Robinson, R. M., Zesta, E., Sibeck, D. G., Chu, M., and Grubbs, G. A. (2018). Impact of precipitating electrons and magnetosphere-ionosphere coupling processes on ionospheric conductance. *Space Weather*, 16(7):829 – 837.
- Kivelson, M. G. and Russell, C. T. (1995). *Introduction to space physics*. Cambridge university press.
- Knight, S. (1973). Parallel electric fields. *Planetary and Space Science*, 21(5):741 – 750.
- Knudsen, D. J. (2001). Structure, acceleration, and energy in auroral arcs and the role of alfvén waves. *Space Science Reviews*, 95(1):501 – 511.
- Knudsen, D. J., Borovsky, J. E., Karlsson, T., Kataoka, R., and Partamies, N. (2021). Editorial: Topical collection on auroral physics. *Space Science Reviews*, 217(1):19.
- Knudsen, D. J., Burchill, J. K., Buchert, S. C., Eriksson, A. I., Gill, R., Wahlund, J.-E., Åhlen, L., Smith, M., and Moffat, B. (2017). Thermal ion imagers and Langmuir probes in the Swarm electric field instruments. *Journal of Geophysical Research: Space Physics*, 122(2):2655 – 2673.
- Laundal, K. M., Reistad, J. P., Hatch, S. M., Madelaire, M., Walker, S., Hovland, A. Ø., Ohma, A., Merkin, V. G., and Sorathia, K. A. (2022). Local mapping of polar ionospheric electrodynamics. *Journal of Geophysical Research: Space Physics*, 127(5).
- Lotko, W. (2004). Inductive magnetosphere-ionosphere coupling. *Journal of Atmospheric and Solar-Terrestrial Physics*, 66(15):1443 – 1456.
- Lui, A. T. Y. (2018). *Review on the Characteristics of the Current Sheet in the Earth's Magnetotail*, chapter 10, pages 155 – 175. American Geophysical Union (AGU).
- Lynch, K., Bonnell, J. W., Burleigh, M., Clayton, R., Hampton, D. L., Lamarche, L. J., Lessard, M., Nikoukar, R., Samara, M., and Zettergren, M. D. (2024a). GNEISS: An auroral ionospheric sounding rocket campaign for a heterogeneous system science case study of auroral current closure. In *AGU Fall Meeting 2024*, Chicago, IL, USA. Presented at AGU24, SA43A-09, invited oral presentation.
- Lynch, K. A., Erlandson, R., Samara, M., Anderson, B., Bortnik, J., Burleigh, M., Deshpande, K., Hampton, D., Kistler, L., Knudsen, D., LaBelle, J., Lyon, J., Magnes, W., Michell, R., Mouikis, C., Nakamura, R., Nikoukar, R., Torbert, R., van Irsel, J., Vines, S., Zettergren, M., and Zou, S. (2024b). ARCS: Auroral Reconstruction CubeSwarm. A 2019

- Heliophysics Medium-Class Explorer Phase A Concept Study. Section D: Science. NASA Technical Report.
- Lynch, K. A., McManus, E., Gutow, J., Burleigh, M., and Zettergren, M. (2022). An ionospheric conductance gradient driver for subauroral picket fence visible signatures near STEVE events. *Journal of Geophysical Research: Space Physics*, 127(12).
- Madelaire, M., Laundal, K., Gjerloev, J., Hatch, S., Reistad, J., Vanhamäki, H., Waters, C., Ohma, A., Mesquita, R., and Merkin, V. (2023). Spatial resolution in inverse problems: The EZIE satellite mission. *Journal of Geophysical Research: Space Physics*, 128(5):e2023JA031394.
- Mallinckrodt, A. J. (1985). A numerical simulation of auroral ionospheric electrodynamics. *Journal of Geophysical Research: Space Physics*, 90(A1):409 – 417.
- Marghitu, O. (2012). *Auroral Arc Electrodynamics: Review and Outlook*, pages 143 – 158. American Geophysical Union (AGU).
- Maxwell, J. C. (1865). VIII. a dynamical theory of the electromagnetic field. *Philosophical Transactions of the Royal Society of London*, 155:459 – 512.
- Medicus, G. (1961). Theory of electron collection of spherical probes. *Journal of Applied Physics*, 32(12):2512 – 2520.
- Milan, S. E., Clausen, L. B. N., Coxon, J. C., Carter, J. A., Walach, M.-T., Laundal, K., Østgaard, N., Tenfjord, P., Reistad, J., Snekvik, K., Korth, H., and Anderson, B. J. (2017). Overview of solar wind-magnetosphere-ionosphere-atmosphere coupling and the generation of magnetospheric currents. *Space Science Reviews*, 206(1):547 – 573.
- Nicolls, M. J., Cosgrove, R., and Bahcivan, H. (2014). Estimating the vector electric field using monostatic, multibeam incoherent scatter radar measurements. *Radio Science*, 49(11):1124 – 1139.
- Nicolls, M. J. and Heinselman, C. J. (2007). Three-dimensional measurements of traveling ionospheric disturbances with the Poker Flat Incoherent Scatter Radar. *Geophysical Research Letters*, 34(21).
- Nykyri, K., Blanco-Cano, X., Knudsen, D., Sibeck, D. G., and Borovsky, J. E. (2025). Editorial: Past, present and future of multispacecraft measurements for space physics. *Frontiers in Astronomy and Space Sciences*, December 2025.
- Paschmann, G., Haaland, S., and Treumann, R. (2003). *Auroral Plasma Physics*. Springer Netherlands, Dordrecht, Netherlands.

Bibliography

- Pedersen, P. O. (1927). *The propagation of radio waves along the surface of the earth and in the atmosphere.* (No. 15). Copenhagen.
- PFISR (2025). <https://data.amisr.com/database>.
- Rees, M. H. and Luckey, D. (1974). Auroral electron energy derived from ratio of spectroscopic emissions 1. model computations. *Journal of Geophysical Research*, 79(34):5181 – 5186.
- Richmond, A. D. and Kamide, Y. (1988). Mapping electrodynamic features of the high-latitude ionosphere from localized observations: Technique. *Journal of Geophysical Research: Space Physics*, 93(A6):5741 – 5759.
- Ritter, P., Lühr, H., and Rauberg, J. (2013). Determining field-aligned currents with the swarm constellation mission. *Earth, Planets and Space*, 65(11):1285 – 1294.
- Robinson, R. M., Vondrak, R. R., Miller, K., Dabbs, T., and Hardy, D. (1987). On calculating ionospheric conductances from the flux and energy of precipitating electrons. *Journal of Geophysical Research: Space Physics*, 92(A3):2565 – 2569.
- Ruohoniemi, J. M., Greenwald, R. A., Baker, K. B., Villain, J. P., Hanuise, C., and Kelly, J. (1989). Mapping high-latitude plasma convection with coherent HF radars. *Journal of Geophysical Research: Space Physics*, 94(A10):13463 – 13477.
- Rönnmark, K. (2002). Auroral current-voltage relation. *Journal of Geophysical Research: Space Physics*, 107(A12).
- Seyler, C. E. (1990). A mathematical model of the structure and evolution of small-scale discrete auroral arcs. *Journal of Geophysical Research: Space Physics*, 95(A10):17199 – 17215.
- Simulations (2025). <https://rcweb.dartmouth.edu/LynchK/Gemini3D>.
- Snively, J. B. and Pasko, V. P. (2008). Excitation of ducted gravity waves in the lower thermosphere by tropospheric sources. *Journal of Geophysical Research: Space Physics*, 113(A6).
- Sobel, I. (2014). An isotropic 3×3 image gradient operator. *Presentation at Stanford A.I. Project 1968*.
- Solomon, S. C. (2017). Global modeling of thermospheric airglow in the far ultraviolet. *Journal of Geophysical Research: Space Physics*, 122(7):7834 – 7848.

- Stamm, J., Vierinen, J., Urco, J. M., Gustavsson, B., and Chau, J. L. (2021). Radar imaging with EISCAT 3D. *Annales Geophysicae*, 39(1):119 – 134.
- Strickland, D. J., Meier, R. R., Hecht, J. H., and Christensen, A. B. (1989). Deducing composition and incident electron spectra from ground-based auroral optical measurements: Theory and model results. *Journal of Geophysical Research: Space Physics*, 94(A10):13527 – 13539.
- SuperDARN (2025). <https://superdarn.ca/data-download>.
- Swarm (2025). <https://earth.esa.int/eogateway/missions/swarm/data>.
- Temerin, M. and Carlson, C. W. (1998). Current-voltage relationship in the downward auroral current region. *Geophysical Research Letters*, 25(13):2365 – 2368.
- Temerin, M. and Mozer, F. S. (1984). Observations of the electric fields that accelerate auroral particles. *Proceedings of the Indian Academy of Sciences-Earth and Planetary Sciences*, 93(3):227 – 245.
- van Irsel, J. (2024). Supporting datasets and computational notebooks [collection]. Repository: “Publication Data from the Lab of K. A. Lynch”. https://rcweb.dartmouth.edu/LynchK/pubdata/2024_vanirsel_jgr/data/.
- van Irsel, J., Lynch, K. A., Mule, A., and Zettergren, M. D. (2024). Generation of top-boundary conditions for 3D ionospheric models constrained by auroral imagery and plasma flow data. *Journal of Geophysical Research: Space Physics*, 129(8):e2024JA032722.
- van Irsel, J., Lynch, K. A., Mule, A., Zettergren, M. D., Burchill, J. K., Lamarche, L., and Hampton, D. L. (2025). Current closure and joule heating in data-driven 3-D auroral arc simulation. Manuscript in preparation.
- Vanhämäki, H. and Juusola, L. (2020). *Introduction to Spherical Elementary Current Systems*, pages 5 – 33. Springer International Publishing, Cham.
- Wang, X., Cai, L., Aikio, A., Vanhamäki, H., Virtanen, I., Zhang, Y., Luo, B., and Liu, S. (2024). Ionospheric conductances due to electron and ion precipitations: A comparison between EISCAT and DMSP estimates. *Journal of Geophysical Research: Space Physics*, 129(2).
- Wolf, R. A. (1975). Ionosphere-magnetosphere coupling. *Space Science Reviews*, 17(2):537 – 562.

Bibliography

- Wu, J., Knudsen, D. J., Gillies, D. M., Donovan, E. F., and Burchill, J. K. (2017). Swarm observation of field-aligned currents associated with multiple auroral arc systems. *Journal of Geophysical Research: Space Physics*, 122(10):10145 – 10156.
- Yano, Y. and Ebihara, Y. (2021). Three-dimensional closure of field-aligned currents in the polar ionosphere. *Journal of Geophysical Research: Space Physics*, 126(9).
- Zettergren, M., Clevenger, H., Lamarche, L., Calhoun, D., Mule, A., Lynch, K., Laundal, K., Snively, J., and Hampton, D. (2024). Multi-scale, data-driven modeling of high-latitude ionospheric responses. Presented at the American Geophysical Union Fall Meeting, Washington, DC, December 2024.
- Zettergren, M. and Snively, J. (2019). Latitude and longitude dependence of ionospheric TEC and magnetic perturbations from infrasonic-acoustic waves generated by strong seismic events. *Geophysical Research Letters*, 46(3):1132 – 1140.
- Zettergren, M. D. and Semeter, J. L. (2012). Ionospheric plasma transport and loss in auroral downward current regions. *Journal of Geophysical Research: Space Physics*, 117(A6).
- Zettergren, M. D. and Snively, J. B. (2015). Ionospheric response to infrasonic-acoustic waves generated by natural hazard events. *Journal of Geophysical Research: Space Physics*, 120(9):8002 – 8024.

The Earth relies on the Sun's energy, but at times this energy can be overwhelming; the Sun expels plasma which, were it not for our humble magnetic field, would erode our atmosphere (Mars, c. 4 Ga). The protective interaction Earth has with the solar wind results in spectacular auroral displays—one such auroral form is discussed in this thesis: quiet discrete auroral arcs.

Such arcs have long been studied; they are abundant, have usable symmetries, and they can predict magnetic substorms that wreak havoc in our magnetosphere. The auroral emissions, albeit beautiful, are however only the visible end of a self-consistent system of currents, electric fields, particle precipitation, and ionospheric conductivity. To study electric currents surrounding auroral arcs, it turns out, requires knowledge of all these aspects.

This thesis enhances our understanding of auroral arcs through the lens of ionospheric current closure. The ionosphere has its plasma transition to being collisional with the neutrals over about 100 km altitude, which allows for currents to flow perpendicular to the local magnetic field—something they cannot do outside our ionosphere. This couples the ionosphere and magnetosphere through magnetic-field-aligned current closure, where the ionosphere can present characteristics not unlike those in a circuit resistor.

The discrete auroral arcs come into play because they are the result of attempting to host field-aligned currents through magnetic flux tubes that can be too tenuous to fulfill their amperage without the creation of parallel electric fields. Such fields can cause electrons to accelerate to energies high enough to ionize the atmosphere. This enhances the ionospheric conductivity, affecting the pathways for current closure.

This thesis outlines methods involving the use of a plethora of heterogeneous, multi-platform auroral measurements curated for driving fully-three-dimensional ionospheric simulations of auroral arcs. This filters for solutions that are geophysical and self-consistent, and allows for the investigation of sensitivities to various input parameters. This work highlights, not just various considerations in performing such simulations, but the very fact that they require all three dimensions for a complete picture. After all, the equations that govern auroral arcs systems are inherently three-dimensional in nature.